Small-Scale Structure in Saturn's Rings

by

Morgan Rehnberg

B.S., Beloit College, 2012

M.S., University of Colorado, 2015

A thesis submitted to the

Faculty of the Graduate School of the

University of Colorado in partial fulfillment

of the requirements for the degree of

Doctor of Philosophy

Department of Astrophysics and Planetary Science

2017

This thesis entitled:
Small-Scale Structure in Saturn's Rings
written by Morgan Rehnberg
has been approved for the Department of Astrophysics and Planetary Science

_____

Prof. Larry Esposito

_____

Prof. Nick Schneider

_____

Prof. Dave Brain

_____

Prof. Ann-Marie Madigan

_____

Prof. Daniel Scheeres

Date _____

The final copy of this thesis has been examined by the signatories, and we find that both the content and the form meet acceptable presentation standards of scholarly work in the above mentioned discipline.

Rehnberg, Morgan (Ph.D., Astrophysics)

Small-Scale Structure in Saturn's Rings

Thesis directed by Prof. Larry Esposito

The rings of Saturn are the largest and most complex in the Solar System. Decades of observation from ground- and space-based observatories and spacecraft missions have revealed the broad structure of the rings and the intricate interactions between the planet's moons and its rings. Stellar occultations observed by the Ultraviolet Imaging Spectrograph's High Speed Photometer onboard the *Cassini* spacecraft now enable the direct study of the small-scale structure that results from these interactions. In this dissertation, I present three distinct phenomena resulting from the small-scale physics of the rings.

Many resonance locations with Saturn's external satellites lie within the main (A and B) rings. Two of these satellites, Janus and Epimetheus, have a unique co-orbital relationship and move radially to switch positions every 4.0 years. This motion also moves the resonance locations within the rings. As the spiral density waves created at these resonances interact, they launch an enormous solitary wave every eight years. I provide the first-ever observations of this never-predicted phenomenon and detail a possible formation mechanism.

Previous studies have reported a population of kilometer-scale aggregates in Saturn's F ring, which likely form as a result of self-gravitation between ring particles in Saturn's Roche zone. I expand the known catalog of features in UVIS occultations and provide the first estimates of their density derived from comparisons with the A ring. These features are orders of magnitude less dense than previously believed, a fact which reconciles them with detections made by other means.

Theory and indirect observations indicate that the smallest regular structures in the rings are wavelike aggregates called self-gravity wakes. Using the highest-resolution occultations, I provide the first-ever direct detection of these features by identifying the gaps that

represent the minima of the wakes. I demonstrate that the distribution of these gaps is consistent with the broad brightness asymmetries previously observed in the rings. Furthermore, the presence of spiral density waves affects the formation of self-gravity waves.

Dedication

To Mom, Dad, Bailey, and Zoe. You are my ever-present constellation.

Acknowledgements

No undertaking of this nature can succeed without substantial support and I've surely been on the receiving end of more than my fair share. A true enumeration of my thanks could itself fill an entire volume, but a few people rise above the many I've counted on these last five years. Foremost among those is my research advisor, Larry Esposito, who extended me an invitation to work on *Cassini* before I even arrived at CU. He offered me tremendous independence and flexibility; I hope I have used it well. Glen Stewart, Nicole Albers, Miodrag Sremčević, Michael Aye, and Zarah Brown each contributed to the development of this work.

My classmates have been an unending source of positivity during an often-trying period of my life. Alex Truebenbach taught me as much about quantum mechanics as I ever taught myself. Andrew Sturner and Justin Holmes were the roommates I never had to worry about and Matteo Crismani gave me a home when I needed it most. Jordan Wheeler was the most underrated of my poker opponents and Bryan Holler the most fun. Marek Slipski proved that scientists can indeed be cool. I'm sorry that after five years I still can't keep you and ~~Marek~~ Matteo straight. I owe Briana Ingermann too much to possibly list here.

Many others have left indelible marks on my CU experience. Evan Tilton joined me for many much-needed drinks. Good nights were often spent in the company of Becky Nevin and Adalyn Fyhrie. Sarah Black was forced to hear every rant about geology. Allie Hunter was my first and oldest friend in Boulder.

Nothing written here would have been possible without the unconditional support of Katherine Peters. You kept me aloft yet grounded and gave me the courage to pursue a career full of uncertainty. I'm excited to brave Texas with you. Let's eat a lot of barbecue.

Contents

Chapter

Tables

Table

Figures

Figure

Chapter 1

Introduction

1.1 Overview

Saturn was among the first objects examined by Galileo through the use of a telescope. In comparison to planets like Mars or Jupiter, Saturn appeared to him as not one, but several objects. Although his telescope was too poor to resolve them, he had discovered the first known planetary rings. Over the last four hundred years, we have discovered a number of additional ring systems in the Solar System and a plethora of ring-like structures elsewhere in the Universe. Saturn's substantial ring system remains the prototypical example.

In this chapter, we will examine the morphology of Saturn's rings, their relationship to the planet's moons, and the physics that underpins them. We will also introduce the other known ring systems and which Saturnian rings best represent them. Finally, we will examine the technique of stellar occultation used throughout this work.

Our knowledge of the rings comes from many sources, including theory and simulation, ground- and space-based telescopic observations, and interplanetary space missions. Most notable are the four spacecraft that have visited Saturn: *Pioneer 11* (1979), *Voyager 1* (1980), *Voyager 2* (1981), and *Cassini* (2004-2017).

Table 1.1 gives some basic physical parameters of Saturn which will be referred to throughout this work.

Parameter	Value	Reference
$r_{\text{equatorial}}$	60268±4 km	Seidelmann et al. (2007)
r_{polar}	54364±10 km	Seidelmann et al. (2007)
GM	37931207.7±1.1 km^3s^{-2}	Jacobson et al. (2006)
J_2	0.01629071±0.00000027	Jacobson et al. (2006)
J_4	−0.00093583±0.00000277	Jacobson et al. (2006)
J_6	0.000091±0.00000964	Jacobson et al. (2006)
ρ_{mean}	687.3 kg m^{-3}	Jacobson et al. (2006)

Table 1.1: Basic parameters for Saturn. Each r is the radius of Saturn at the specified location, GM measures the planet's mass and ρ_{mean} gives its bulk density. J_2, J_4, and J_6 are the first three gravitation moments of the planet and describe the spatial distribution of mass within Saturn.

1.2 Rings of Saturn

Even a passing visual inspection will reveal that the Saturnian rings are not a single, continuous structure. This was first noted by the Italian astronomer Giovanni Cassini in 1675 and today both the *Cassini* spacecraft and the region separating the A and B rings are named in his honor. The major rings are named in the approximate order of their discovery and extend outwards from Saturn (see figure 1.1) as follows: D, C, B, A, F, G, E, Phoebe (discovered most recently). Several additional narrow, tenuous rings have also been found, as well as arcs of material that do not stretch entirely around the planet. Changing physical and chemical composition, in addition to different origins and environments lead to large variety among these rings.

1.2.1 A ring

The A ring spans the region 122,340 - 136,780 km from the center of Saturn (Murray and Dermott, 1999). It is bounded on the inner edge by the Cassini Division and on the outer edge by a 7:6 mean motion resonance with Janus. Two embedded moons, Pan and Daphnis, open gaps in the ring known as the Encke and Keeler gaps, respectively. Mean motion resonances with Saturn's moons Atlas, Epimetheus, Janus, Mimas, Pandora, and Prometheus launch sizable density waves in this region of the rings.

Using images of spiral density waves observed with the *Cassini* Imaging Science Subsystem, Tiscareno et al. (2007) derive an approximate surface mass density for the A ring of 400 kg/m^2. This surface density appears to increase as one moves farther from the planet. They conclude the inner A ring has a vertical thickness (height) of 10-15 m for $r < 127,000$ km. The outer A ring is not substantially thicker.

Spectral observations of the main rings indicate they are 90-95% water ice (Filacchione et al., 2012). By examining diffraction spikes observed by the *Cassini* Ultraviolet Imaging Spectrograph at the outer edge of the A ring and at the edges of the Encke gap, Becker

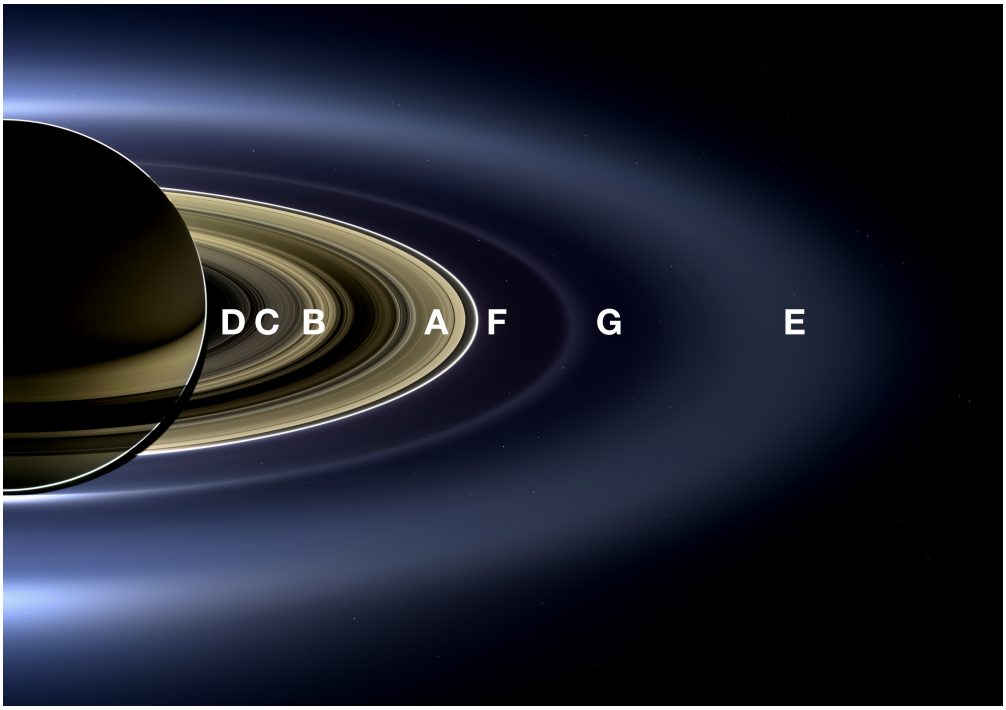

Figure 1.1: A back-lit *Cassini* image of Saturn and its rings. Enceladus (a = 237,948 km) is embedded in the E ring. The Phoebe ring lies far outside the field of view.

et al. (2016) deduce a minimum particle size on the order of 10 mm. They observe the minimum particle size to decrease and the size distribution to steepen with increasing radial distance from Saturn. Observations made with the *Cassini* Visual and Infrared Mapping Spectrometer indicate many particles with radii in the range of 10 μm (Nicholson et al., 2008). These small particles may exist as a regolith on the surfaces of larger ring particles.

The A ring is the most studied of Saturn's rings because of its combination of moderate features. Its optical depth is neither so small as to be difficult to observe nor so large as to be impervious to stellar occultations. The large sampling of spiral density waves provides a ready means for observing the *in situ* nature of the rings from afar.

1.2.2 B ring

The B ring extends from 91,975 - 117,507 km from Saturn, with its outer edge bounded by a 2:1 mean motion resonance with Mimas. Much of it is substantially less transparent than the A ring and the optical depth of the most-opaque central regions essentially extinguishes the light from even the brightest stars. No spiral density waves from this region are easily observable, which substantially limits our ability to accurately infer the ring's mass. This is troublesome, as it seems likely that the B ring dominates the total mass of the ring system.

Through a *Voyager* stellar occultation by the Janus 2:1 spiral density wave, Esposito et al. (1983) concluded a surface mass density for the inner B ring of 700$\pm$100 kg/m^2. Lissauer (1985) used the same occultation to examine the Mimas 4:2 bending wave in the outer B ring and determined a value of 540$\pm$100 kg/m^2 for that region. Recently, Hedman and Nicholson (2016) aligned and co-added a series of *Cassini* VIMS occultations to derive a surface mass density estimate for the central B ring by revealing embedded density waves. Their result of 420 - 1410 kg/m^2, which required substantial data filtering, suggests ring particles which are less dense than ice. A simulation-derived result of 2400 - 4800 kg/m^2 proves there remains substantial disagreement about the density (and thus the mass) of the B ring (Robbins et al., 2010). B-ring particles are similar in composition and size to those

of the A ring.

1.2.3 Cassini division and the C ring

Separating the A and B rings is the Cassini division. Originally interpreted as a region of empty space, we now know that a series of fine ringlets occupies this area. These ringlets share a common morphology with the C ring (74,658 - 91,975 km from Saturn). Both regions display a background optical depth in the neighborhood of 0.1 and are punctuated by a number of gaps. More tenuous than the A and B rings and much deeper in Saturn's gravity well than the F ring, the C ring and the Cassini division appear to be extraordinarily thin. In fact, the C ring may have a vertical thickness of less than 2 m in some locations (Baillié et al., 2011).

The C ring is home to a pair of phenomena not seen elsewhere in the rings. Its background is often interrupted by regions of rapidly-increased optical depth known as "plateaus." These regions appear to contain smaller particles than the rest of the ring. Although a number of density waves are visible in the C ring, relatively few have been linked to resonances with exterior satellites. Recent work has suggested that some of these waves may be raised by resonances with mass interior to the planet (Hedman and Nicholson, 2013, 2014).

1.2.4 F ring

Saturn's F ring is perhaps the most dynamically-interesting location in the Solar System. It lies within the planet's Roche zone for reasonable values of particle density (see section 1.4.1). The tug-of-war between Saturn's gravity and self-gravity leads to a nearly-continuous process of aggregations and dis-aggregation. One result of this interaction is a dramatically-thicker ring. Instead of a thickness (vertical height) on the order of the A ring's 10 m, the F ring measures 13±7 km (Scharringhausen and Nicholson, 2013). Thus, despite an optical depth that ranges from similar to the C ring to similar to the A ring, the mean free path is much larger.

Another notable feature of the F ring is its ephemeris. Unlike the inner rings, it has a measurable eccentricity (2.35×10^{-3}) and inclination (6.43×10^{-3} degrees), which cause aggregates contained within to move several hundred kilometers towards and away from the planet over the course of an orbit ($a = 140221.3 \pm 1.8$ km) (Albers et al., 2012)

1.2.5 D ring and the outer rings

The A, B, and C rings, as well as the Cassini division ringlets, can be considered dense, collisional rings. The F ring falls somewhat in between, but the remainder of the rings are tenuous. These include the D, G, E, and Phoebe rings. A number of faint ringlike structures exist elsewhere in the Saturn system.

The D ring begins about 5000 km from the planet's cloud tops and extends until it meets the C ring at about 74,500 km (Dougherty et al., 2009). The first extensive observations of the D ring were made by the *Voyager* spacecraft, which observed a series of distinct regions (or ringlets) within the ring. *Cassini* observations show that at least one of these structures has changed substantially in the intervening decades (Hedman et al., 2007a). Close proximity to massive Saturn may yield an environment which evolves rapidly.

Perhaps the most intriguing of the remaining is the E ring, which is centered on the semi-major axis of Enceladus ($a = 237{,}948$ km). One of the major achievements of *Cassini* is the discovery that water-vapor plumes emanating from the moon's south pole sustains the ring (Hansen et al., 2006; Porco et al., 2006). These plumes are associated with warm cracks on the surface (the "tiger stripes"), which recent work has shown lead to a global subsurface ocean (Spitale and Porco, 2007; Thomas et al., 2016). E ring particles coat the surfaces of nearby satellites like Tethys.

1.3 Moons of Saturn

Saturn's satellite system rivals Jupiter's as the Solar System's most diverse. Most notable of those not relevant to this work is Titan, the planet's largest moon. With a dense

atmosphere, surface liquid, and a weather system, it is perhaps the place in the Solar System most like the Earth.

Moons can affect planetary rings in multiple ways and the Saturnian system contains examples of each. They can affect the rings directly through physical or close gravitational interactions or indirectly through resonance perturbations. They can also serve as the source of a ring, again directly through (cryo)volcanism or indirectly as a target for micrometeoroid bombardment. Table 1.2 summarizes the important physical and orbital parameters for the satellites described here.

1.3.1 Pan and Daphnis

The A ring contains two permanently cleared gaps, the Encke gap (133,410 - 133,740 km) and the Keeler gap (136,487 - 136,522 km), both in the outer part of the ring (Murray and Dermott, 1999). The Encke gap is held open by Pan, which has a mass of $4.95 \pm 0.75 \times 10^{15}$ kg and a radius of 14.1±1.3 km, while the Keeler gap contains Daphnis, with a mass of $7.7 \pm 1.5 \times 10^{13}$ kg and a radius of 3.8 ± 0.8 km (Porco et al., 2007; Jacobson et al., 2008). These imply bulk densities of 420 ± 150 kg/m^3 and 340 ± 260 kg/m^3, respectively, which are both substantially lower than the density of ice, ~ 917 kg/m^3 (Thomas, 2010).

Pan in particular exerts substantial influence on the nearby ring material. These wave-like perturbations are commonly called wakes and are large enough to have been observed in *Voyager* stellar and radio occultations (Horn et al., 1996). Images by the *Cassini* Imaging Science Subsystem have also revealed the dramatic vertical perturbations and wavy radial structure excited by Daphnis at the Keeler gap edge (see figure 1.2).

1.3.2 Prometheus and Pandora

Prometheus and Pandora orbit just interior and just exterior to the F ring and act as "shepherd satellites " in confining the ring radially. As the more massive and nearer of the pair, Prometheus is the principal perturber of the F ring. *Cassini* images have revealed that

Name	r_{mean} (km) [1]	M (kg) [1]	a (km) [2]	i (°) [2]	e [2]
Daphnis	7.6	7.7×10^{13}	136,506	0.0036	0.000033
Enceladus	252.1	1.08×10^{20}	237,948	0.019	0.0047
Epimetheus	58.1	5.3×10^{17}		0.351	0.0098
2002-2006, 2010-2014			151,410 [4]		
2006-2010, 2014-2018			151,490 [4]		
Janus	89.5	1.9×10^{18}		0.163	0.0068
2002-2006, 2010-2014			151,460 [4]		
2006-2010, 2014-2018			151,440 [4]		
Mimas	198.2	3.7×10^{19} [3]	185,520	1.53	0.0202
Pan	14.1	5×10^{15}	133,584	0.0001	0.000014
Pandora	40.7	1.4×10^{17}	141,720	0.05	0.0042
Prometheus	43.1	1.6×10^{17}	139.380	0.008	0.0022

[1]Thomas (2010), [2]Spitale et al. (2006), [3]Jacobson et al. (2006), [4]Jacobson et al. (2008)

Table 1.2: Physical and orbital properties of moons relevant to this work. Two values for a are listed each for Janus and Epimetheus due to their orbital swap (which occurs on 21 January of the specified years).

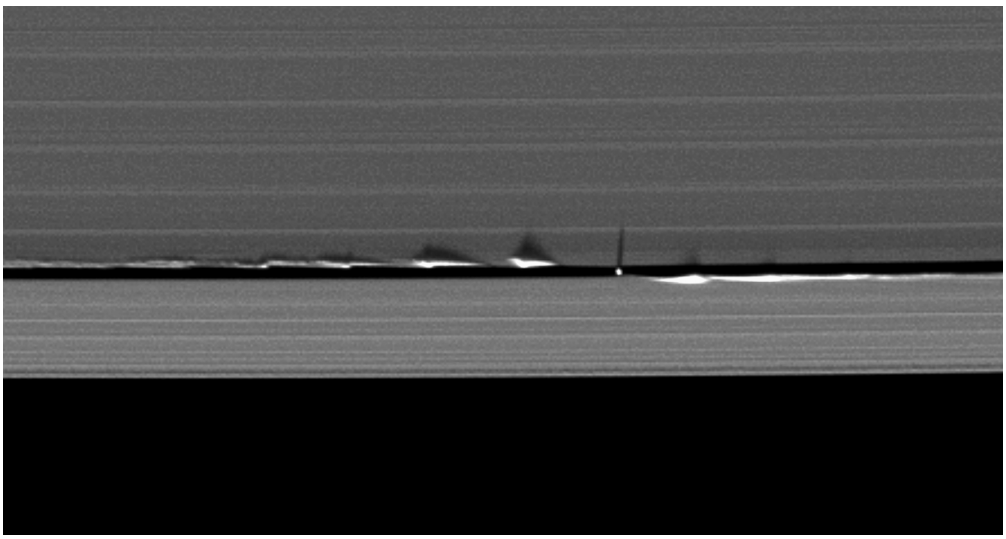

Figure 1.2: A *Cassini* image of Daphnis and the edge of the Keeler gap. Notice the shadows cast by vertical structure excited by the satellite.

each time the moon approaches the rings ($P = 14.7$ hr) it gravitationally carves "channels" through the F ring structure. These channels are the result of Prometheus pulling particles from their nominal locations, which leave gaps that are sheared out by Keplerian motion (Murray et al., 2005).

Both Prometheus and Pandora also have mean motion resonances that fall within the A ring and excite spiral density waves. Close proximity means that these moons have numerous such resonances that fall within the ring.

1.3.3 Janus and Epimetheus

Janus and Epimetheus are of particular interest because they represent the only pair of co-orbiting satellites in the solar system. While many planets have asteroids trapped in co-orbital resonances with them (i.e., the Trojans of Jupiter), Janus and Epimetheus are unique because of their comparable masses ($m_E/m_J = 0.278$). Dermott and Murray (1981) showed that this leads to each moon traversing a horseshoe orbit about the pair's shared mean orbital radius of 151,450 km. This gives a small relative velocity between the two. Every 4.0 years, the pair approach each other closely and exchange orbital angular momentum. This causes a rapid shift, in which the inner and outer bodies switch position. During *Cassini's* time at Saturn, this has occurred three times: 21 January 2006 (Janus moves inwards), 21 January 2010 (Janus moves outwards), and 21 January 2014 (Janus moves inwards).

When a moon moves radially, the location of its resonances also move. This begins the process of exciting a new density wave at that location, which will propagate outwards at the local group velocity. Thus, after the orbit swap, it can take substantial time for a density wave to reappear. Tiscareno et al. (2006b) demonstrate that for second-order, linear waves, it can take more than a year for an identifiable wave pattern to appear.

1.3.4 Enceladus

Like Pan and Daphnis, Enceladus is embedded in one of the planet's rings. Its location in the midst of the E ring led to early hypotheses that it was, in fact, the ring's source (Baum et al., 1981; Haff et al., 1983). This was confirmed by *Cassini*, which observed a plume of water emanating from the south pole region of the moon (Hansen et al., 2006; Porco et al., 2006). The so-called "tiger stripes", a series of cracks from which the plume was emitted, correspond with a substantial increase in subsurface heat and recent observations have revealed that this supports a global subsurface ocean (Spitale and Porco, 2007; Thomas et al., 2016).

Particles ejected from the moon travel widely throughout the Saturn system and are responsible for altering the albedos of other nearby moons. Enceladus is illustrative of a different relationship between a ring and a moon and reinforces the dynamic nature of ring-moon systems. The rings themselves may well be the source of a number of Saturn's small and intermediate moons and yet moons can also be the source of new rings. This interplay is likely vital to the history of the Saturn system.

1.3.5 Mimas and the outer moons

Saturn has seven large, regular satellites: Titan, Rhea, Iapetus, Dione, Tethys, Enceladus, and Mimas. Enceladus is discussed in section 1.3.4 and, of the rest, Mimas is by far the most important when studying the rings. It is the smallest of all seven, but also the closest to Saturn and thus to the main rings. This results in a number of Mimas resonances falling within the A and B rings. Most notable of these is the 2:1 inner Lindblad resonance, which sets the outer edge of the B ring. Mimas' non-negligible inclination also raises vertical perturbations in the rings, known as bending waves (see section 1.4.5).

Saturn also hosts two relatively large irregular satellites, Phoebe and Hyperion. Hyperion is of particular dynamical interest as it rotates chaotically. Its surface also has a striking

sponge-like appearance. Phoebe, however, is more interesting from the perspective of rings, as it is embedded in an enormous, tenuous ring likely generated by micrometeoroid impacts on the moon's surface (Verbiscer et al., 2009).

1.4 Physics of the rings

The rings of Saturn represent a remarkable natural laboratory for the observation of particle disk physics. The following will provide an overview of the processes relevant to the remainder of this work. One notable aspect is that the dynamics of the main rings occur largely in the absence of interaction with the planet's magnetosphere. The "spoke" phenomenon is the only large-scale main ring observation attributed to magnetic effects.

1.4.1 Particle self-gravity

The key process at work in the rings is the interplay between the gravity of Saturn and that of the individual ring particles. Far from the planet, inter-particle gravity is capable of holding together aggregates even against the effects of rotation (i.e., rubble pile asteroids). The closer this aggregate is to Saturn, however, the larger the effect of the planet's differential gravity (tidal force). The location where the magnitude of the tidal force exceeds that of self-gravity is commonly known as the Roche limit and can be written in a general form as

$$a_R = C \left(\frac{\rho_p}{\rho} \right)^{1/3} r_p, \tag{1.1}$$

where ρ_p and r_p are the density and equatorial radius of the planet, respectively, ρ is the density of the accreting particles, and C is a constant. C changes with the assumed model for the aggregate. For a fluid body in hydrostatic equilibrium, $C = 2.456$ (c.f. Esposito (2006)).

Given a distribution of particle densities, aggregates of different permanence can form at different distances from Saturn. Thus, it is typical to think less of a Roche limit and more of a Roche zone, where aggregation and disaggregation are in flux. Canup and Esposito

(1995) define a "critical density" ρ_p at which solid-body accretion becomes possible for a given location a in the rings:

$$\rho_{\rm crit} \approx 9.1 \left(\frac{R_p}{a}\right)^3 \rho_p. \tag{1.2}$$

At the outer edge of the A ring, $\rho_{\rm crit} = 535$ kg m^{-3} and in the F ring it is 497 kg m^{-3}. Of course, solid bodies are held together by more than simply self-gravity and thus moons like Pan and Daphnis can withstand the tidal stresses at locations well within the classical Roche limit. Instead of being a vast collection of gravitationally-bound ice particles, their solid structure is held together by chemical forces which are stronger than Saturn's tides.

Within the rings, the gravitational attraction between ring particles is balanced by their random motions, given by their dispersion velocity c. If that velocity becomes too low, the effects of self-gravity can begin to dominate. Toomre (1964) showed that a differentially-rotating particle disk can become locally-unstable if the dispersion velocity falls below a critical value $c_{\rm cr}$ given by

$$c_{\rm cr} = \frac{3.36 G\sigma}{\kappa}. \tag{1.3}$$

In this case, small-scale axisymmetric disturbances form with approximate wavelengths of

$$\lambda_{\rm cr} = \frac{4\pi^2 G\sigma}{\kappa^2}, \tag{1.4}$$

where κ is the epicyclic frequency (see the next section). At a location in the mid-A ring ($a =$ 127,000 km) and assuming a surface mass density of 400 kg m^{-3}, these so-called "self-gravity wakes" would have a wavelength of 57 m. Such tenuous structures must be transitory, but, averaged over a large region, they achieve an equilibrium state.

1.4.2 Ring-moon resonances

Saturn's more than sixty moons provide for a large variety of orbital resonance locations. Several types of resonances are possible, including corotation, vertical, and Lindblad.

Owing to the minimal inclinations and exterior nature of most of Saturn's regular satellites, Lindblad resonances are most common within the A ring.

Esposito (2006) gives the condition for an inner Lindblad resonance as:

$$m(\Omega_p - n) = -\kappa, \tag{1.5}$$

where $m\Omega_p = mn_s + k\kappa_s$ is an integer multiple of the angular speed with which the gravitational potential of an orbiting, exterior satellite with no inclination rotates. It is given in terms of n_s, the satellite's mean orbital angular velocity and κ_s, the radial, or epicyclic, frequency of its orbit. The numbers n and κ represent the same quantities for a test particle within the rings. The coefficients m and k are integers, with $m > 0$ specifying the number of spiral arms the resonance will create. Because Saturn's oblateness is relatively low, to first order $n \approx \kappa,\ n_s \approx \kappa_s$ and we can rewrite equation 2.1 as

$$(m + k)n_s = (m - 1)n. \tag{1.6}$$

This leads to the common practice of labeling resonances as $(m + k) : (m - 1)$.

In order to precisely compute locations of resonances within the rings, however, we must not make approximations like $n_s \approx \kappa_s$ and instead compute them separately based on a more complete model of Saturn. This is necessary because of Saturn's oblateness; if the planet were a perfect sphere, then $n_s = \kappa_s$. Lissauer and Cuzzi (1982) give more precise expressions:

$$n_s = \frac{GM_p}{r^3}\left[1 + \frac{3}{2}J_2\left(\frac{R_p}{r}\right)^2 - \frac{15}{8}J_4\left(\frac{R_p}{r}\right)^4 + \frac{35}{16}J_6\left(\frac{R_p}{r}\right)^6\right] \tag{1.7}$$

and

$$\kappa_s = \frac{GM_p}{r^3}\left[1 + \frac{3}{2}J_2\left(\frac{R_p}{r}\right)^2 + \frac{45}{8}J_4\left(\frac{R_p}{r}\right)^4 - \frac{175}{16}J_6\left(\frac{R_p}{r}\right)^6\right], \tag{1.8}$$

where M_p is the mass of the planet and J_i are the planet's gravitational coefficients. Equation 1.5 can then be solved numerically to compute the precise resonance location.

1.4.3 Ring-planet resonances

In section 1.4.2, we explicitly considered the perturbing effects of exterior satellites on the rings. Although such resonances comprise the entirety of this work, it is worth considering for a moment that there is nothing unique about this configuration. Satellites interior to a ring would also induce gravitational perturbations that could align with a ring particle's frequency of radial oscillation. In fact, *any* interior mass would have this effect, including mass embedded within the planet itself.

If this mass were distributed with azimuthal isotropy, the perturbation would be uniform and thus have no effect. All planets, however, have interior inhomogeneities, which trace out a repeating path for each rotation of the planet. In a gas giant like Saturn, there may even be interior masses which move at least partially independent of planetary rotation. We call resonances excited by any interior mass, whether inside a planet or not, an outer Lindblad resonance. They follow the same conditions previously described, only with $m < 0$.

Waves launched at these resonances have been observed in the C ring and are beginning to enable inferences about the interior structure of Saturn (Hedman and Nicholson, 2013, 2014).

1.4.4 Spiral density waves

The kilometer-scale structure visible in nearly all observations of Saturn's A and B rings can be attributed primarily to the presence of spiral density waves. Lin and Shu (1964) were the first to develop a theory of density waves to explain the spiral structure of many galaxies. Thus originates the name for the feature seen in the rings of Saturn. Spiral density waves as postulated by Lin and Shu (1964) are the result of natural modes in the otherwise-uniform surface mass density of a galaxy. Saturn's rings are a different situation. As discussed previously, the planet's many moons provide a myriad of regular, periodic forcing frequencies within the rings. Collisions between particles are also common

in the rings; the stars in a galaxy form an essentially collisionless system.

Goldreich and Tremaine (1982) and Shu (1984) were among the first to apply the theory of spiral density waves to explain the structure of Saturn's rings. The flybys of *Voyager 1* and *Voyager 2*, as well as the ongoing *Cassini* mission have prompted continued interest in this phenomenon. Tiscareno et al. (2007) provide an overview of these developments. The following discussion stems from that work and the work of Shu (1984).

On scales much larger than the particle size ($\sim$ cm), Saturn's relatively dense main rings (A and B) can be conveniently considered as a fluid. Define ϕ_p, ϕ_s, and ϕ_d as the gravitational potentials due to the planet, satellite, and disk self-gravity, respectively. Then, in cylindrical coordinates, a disk of with surface mass density σ must obey Poisson's Law,

$$\nabla^2 \phi_d = 4\pi G \sigma \delta(z), \tag{1.9}$$

for $\delta(z)$, the Dirac delta function and G, the gravitational constant. Calling $\mathbf{u} = u\hat{r} + v\hat{\theta}$ the disk also satisfies the mass and momentum conservation equations:

$$\frac{\partial \sigma}{\partial t} + \nabla \cdot (\sigma \mathbf{u}) = 0 \tag{1.10}$$

$$\frac{\partial u}{\partial t} + u\frac{\partial u}{\partial r} + \frac{v}{r}\frac{\partial u}{\partial \theta} - \frac{v^2}{r} = -\frac{\partial}{\partial r}\left(\phi_p + \phi_s + \phi_d\right) \tag{1.11}$$

$$\frac{\partial v}{\partial t} + \frac{u}{r}\frac{\partial (rv)}{\partial t} + \frac{v}{r}\frac{\partial v}{\partial \theta} = \frac{1}{r}\frac{\partial}{\partial r}\left(\phi_s + \phi_d\right) \tag{1.12}$$

Assuming the perturbations in the surface density are small compared to the overall surface density σ_0 of the ring (we will see later that this is often a poor assumption), we can linearize the equations and solve for the solutions to the equations as exponential functions of radius and time. We can further assume that a smoothly varying radial profile can be separated from the rapid azimuthal variation. Then the time- and position-varying surface density σ is given by:

$$\sigma(r, \theta, t) = \sigma_0(r) + \mathrm{Re}\left(S(r) e^{i(\Omega_p t - m\theta)}\right), \tag{1.13}$$

where $S(r)$ is the amplitude of the radial variation, defined by Shu (1984) as his equation 24c.

Equation 1.13 is sufficient for our purposes, however, to analyze the qualitative behavior of a spiral density wave. The perturbation on the background surface density has an amplitude governed by the overall surface density of the ring (through ϕ_d as constrained by equation 1.9) and the mass of the perturbing moon (through ϕ_s). The wave oscillates with a wavelength governed by the frequency of the forcing (through the pattern speed Ω_p), given by the dispersion relation

$$(\Omega_p - m\Omega)^2 = \kappa^2 + k^2c^2 - 2\pi G\sigma_0|k|, \tag{1.14}$$

for the wavenumber k, epicyclic (radial) frequency κ, and sound speed c (Shu, 2016). The second (pressure) term is usually neglected.

Even neglecting the fact that the surface density perturbation $\Delta\sigma$ is often comparable in magnitude to σ_0, an important piece of physics is missing from equation 1.13: damping. Indeed, spiral density waves within the rings are rarely observed to extend for more than 200 km, a relatively short distance when compared with the 12,440 km radial width of the A ring. Correcting for viscous damping involves adding the viscous terms $\nu\nabla^2\mathbf{u} + (\xi + \frac{1}{3}\nu)\nabla(\nabla \cdot \mathbf{u})$ to equations 1.11 and 1.12, where ν is the shear viscosity and ξ is the bulk viscosity. Shu (1984) demonstrates (omitted here) that damping occurs exponentially at radii greater than the resonance location r_L:

$$\text{amplitude} \propto \exp\left[-\left(\frac{r - r_L}{X_d}\right)^3\right], \tag{1.15}$$

for X_d the damping length.

Finally, we must address the non-linearity of many spiral density waves in Saturn's rings. All the waves examined in this work show strong non-linear features. These features generally manifest themselves as wave crests (regions of increased surface density) that are much steeper than wave troughs (regions of decreased surface density). Figure 1.3 illustrates

a typical wave. Tiscareno et al. (2007) (their equations 1-4) give the equation specifying the surface density perturbation in this case, but we will not derive it here.

Waves launched propagate from the resonance towards the location where $n = \Omega_p$. For inner Lindblad resonances, this results in outward propagation, while waves excited by outer Lindblad resonances go inward (Hedman and Nicholson, 2013).

1.4.5 Bending waves

Of the moons with a substantial number of resonances that fall within the main rings, only Mimas ($i = 1.574°$) has the inclination necessary to raise bending waves. These waves, which are the vertical displacement of ring particles, arise at locations analogous to Lindblad resonances. Just as orbiting objects oscillate radially with frequency κ (see section 1.4.2), they also oscillate vertically with frequency μ. Bending waves propagate from locations that satisfy

$$m(\Omega_p - n) = -\mu, \tag{1.16}$$

where here $m\Omega_p = nm_s + p\mu_s$ (in general, $m\Omega_p = nm_s + k\kappa_s + p\mu_s$, where for Lindbald resonances $p = 0$ and here $k = 0$).

As bending waves do not play a significant role in this work, we will not derive their structure here. A good discussion can be found in Shu et al. (1983). One interesting observational property of bending waves is that their structure disappears with high observation angles, since particles are only vertically displaced. Figure 1.4 illustrates this effect. Four Mimas bending waves, the 4:2, 7:4, 5:3, and 8:5 are easily visible in the main rings (Lissauer, 1985).

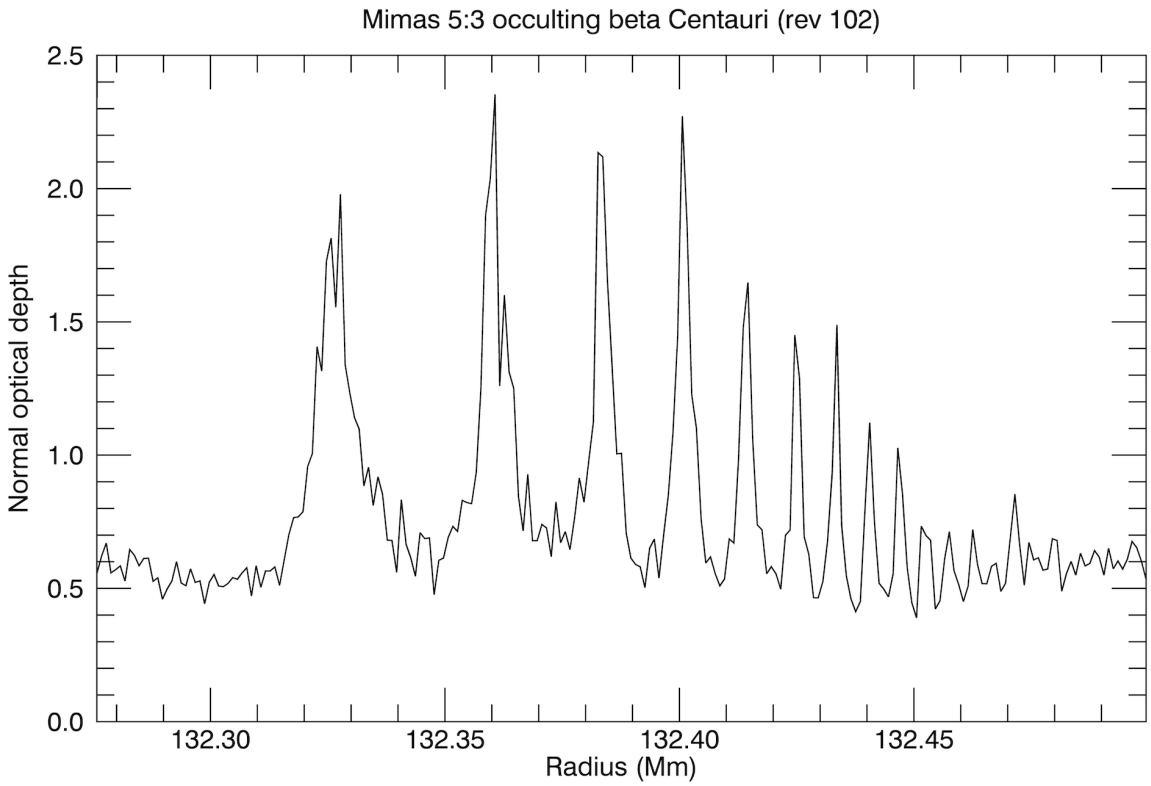

Figure 1.3: A typical Mimas 5:3 spiral density wave smoothed to 1 km. Note the steepened crests.

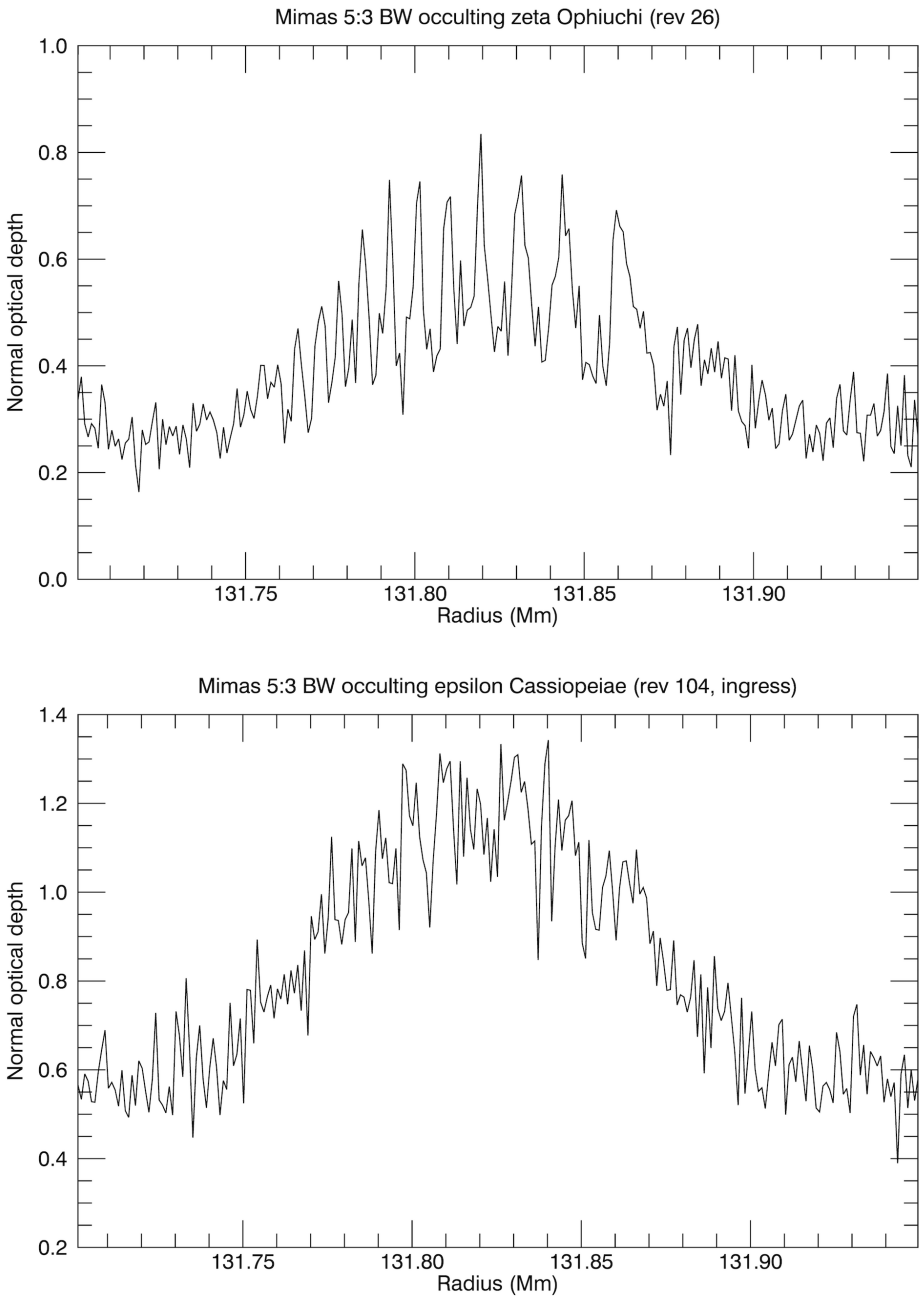

Figure 1.4: The Mimas 5:3 bending wave as seen from a low observation angle ($b = 16.2°$, top) and a high angle ($b = 70.0°$, bottom). Notice how the structure of the wave begins to disappear at the higher angle.

1.5 Age and origin of the rings

The most enduring mystery of Saturn's rings is their age and thus their origin. The case for a young (non-primordial) ring system hinges on two arguments: their observed purity and their expected dynamical evolution.

The apparent cleanliness of the rings (90-95% water ice) is the most direct indicator that the rings should be relatively recent. The rings are exposed to a continuous flux of meteoritic dust from interplanetary space, which Doyle et al. (1989) compute would pollute the rings to their current water ice purity within 100-200 million years. Even a substantially-reduced impactor flux would pollute the rings in less than the age of the Solar System.

The size and shape of the rings have also likely changed since their formation. Two factors that shape this evolution are the transfer of angular momentum from the rings to resonant moons and the viscous spreading of a collisional ring system. If angular momentum transfer is rapid relative to the age of the Solar System, it implies the current arrangement is likely transitory. Goldreich and Tremaine (1982) derived the approximate timescale for a satellite near the A ring edge to double its separation from the ring:

$$t_s \approx 8 \times 10^5 \text{ yr} \left(\frac{a_s - r}{r}\right) \left(\frac{1000 \text{ kg m}^{-3}}{\sigma}\right) \left(\frac{10^{18} \text{ kg}}{M_s}\right) \left|\frac{a_s - r}{1000 \text{ km}}\right|^3, \tag{1.17}$$

for a_s the semi-major axis of a satellite with mass M_s and r the location of a ring edge with surface mass density σ. Using *Cassini*-derived values for the moon Pandora yields $t_s \approx 6.2 \times 10^7$ yr, about two orders of magnitude shorter than the age of the Solar System.

The low bulk density of Saturn's small, icy satellites has been interpreted as evidence that they accreted, at least in part, out of ring material (e.g. Porco et al. (2007)). Such accretion could only occur beyond the Roche limit, while the present-day rings are presumed to contain the vast bulk of their mass in the interior A and B rings. This suggests that the rings must have been more massive and extended farther out in the past. More massive rings, however, evolve more rapidly and Salmon et al. (2010) perform variable-viscosity simulations

to determine that the rings as visible now have a dynamical age most resembling 100 million years and very likely less than 1 billion years.

Both the purity and the dynamic evolution of the main rings hinge on their overall mass, which appears to be within in order of magnitude of the mass of Mimas. The exact figure remains a matter of substantial dispute, but should be determined accurately by the final *Cassini* maneuvers in the vicinity of the rings. During these orbits, Doppler shifts in the spacecraft's transmissions to Earth will allow for an estimate with an accuracy on the order of several percent. If the rings prove to be more massive than anticipated, perhaps they can absorb and distribute polluting material in such a way as to retain their youthful appearance over the age of the Solar System (Esposito et al., 2012). If the rings are less massive, as suggested by at least one recent study, then they are almost surely young (Hedman and Nicholson, 2016).

The primary obstacle to a young ring system is its mechanism of formation. Two general categories of formation mechanism are plausible: the disruption of a satellite or the disruption of a comet. A third scenario, that the rings are a remnant of the circumplanetary disk, seems unlikely in the face of their composition.

If a comet were to pass close to the planet, it is plausible that tidal forces could tear it apart, spreading at least some of its material in the region that would eventually become the rings. Although this could occur at any time (Dones, 1991), it is more likely to happen in the early Solar System when the density of comets and other icy planetesimals is greater. Charnoz et al. (2009), however, find the number of these objects during the Late Heavy Bombardment is so large that we should expect Saturn-like rings around all the gas giants.

Another possibility is that one of these passing comets stuck a moon with an orbit similar to the present-day location of the rings. If the impact were sufficiently large enough, it could break apart the satellite and form a ring in its place. Such a collision would be even more unlikely than the previous scenario, again benefiting from the increased flux early in the Solar System's history. A further complication is that any satellite that co-accreted with

Saturn would contain a substantial fraction of metals and silicates, which we do not observe in the rings today.

Canup (2010) combines the heretofore described scenarios into one that neatly accounts for many of the properties of the current rings. One unusual feature of Saturn is that it hosts only one large satellite, Titan, in comparison to the four found at Jupiter. If multiple such moons formed in the early Solar System, then perhaps one migrated through the circumplanetary disk and spiraled into the planet. Such an object would be too large to fully disrupt with tidal forces; instead, the outer layers would be preferentially removed before the remainder collided with Saturn and was absorbed. Objects as large as Titan are nearly always differentiated (the lone exception being Jupiter's Callisto) and thus those outer layers would be composed primarily of ice, the primary constituent of the rings today. A massive initial ring could have then formed Saturn's present icy satellites.

1.6 Rings in other contexts

Although the rings of Saturn are the most massive and varied yet observed, ring systems have been found around all other gas giants in the Solar System, around smaller objects, and encircling planets around other stars. Here I give an overview of these systems and contrast them with the Saturnian rings.

1.6.1 Jovian rings

The rings of Jupiter were first discovered by *Voyager 1*, although our current understanding of them is primarily derived from observations made in the 1990s by the *Galileo* spacecraft. They can be divided into three broad regions: an inner, nebulous halo, a flatter main ring, and outer, tenuous "gossamer" rings. Unlike Saturn's icy rings, the particles which comprise the Jovian rings are smaller and composed of dust. All the rings of Jupiter are likely generated and sustained from the ejecta of micrometeoroid collisions with known embedded satellites. Figure 1.5 shows configuration of this system.

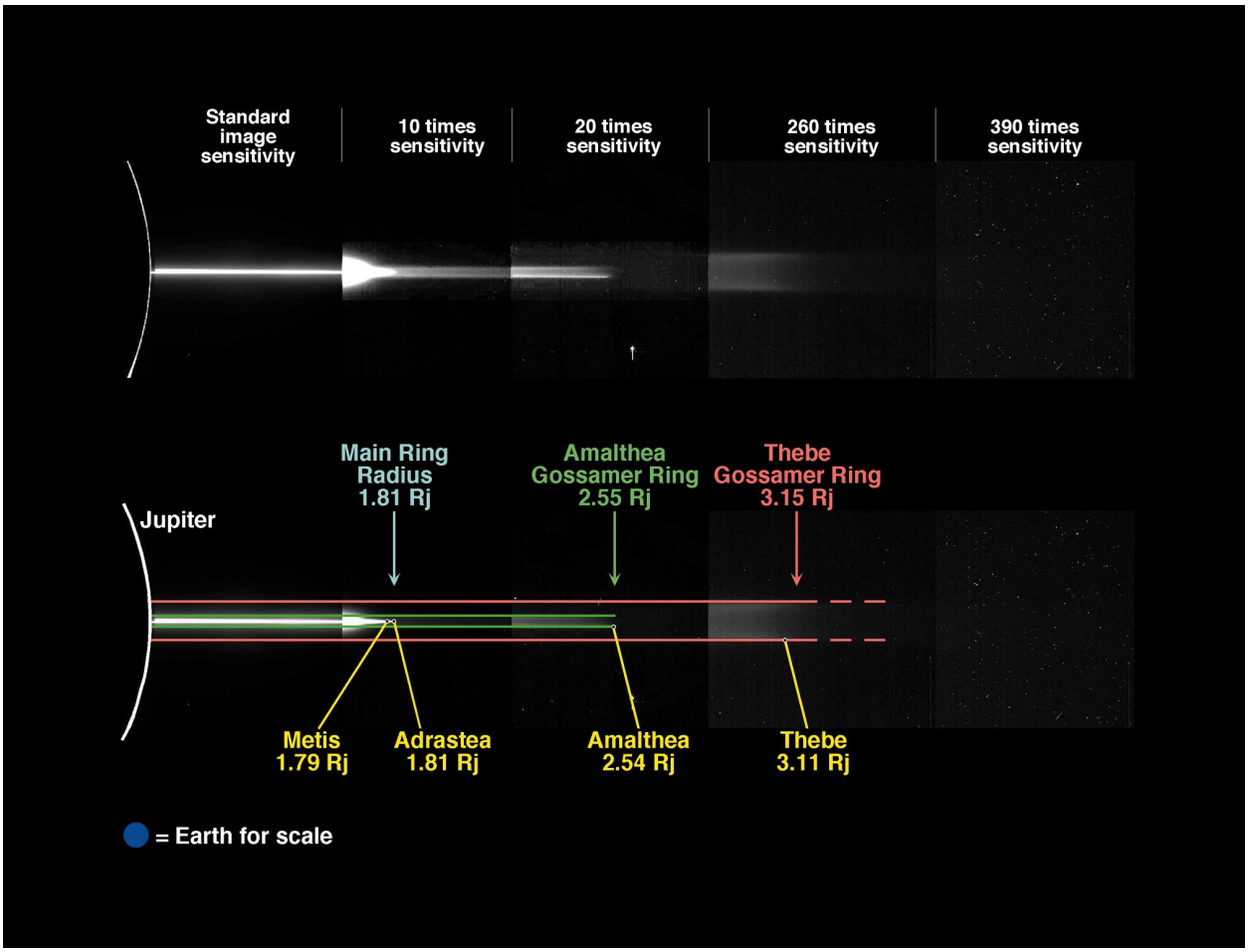

Figure 1.5: The ring system of Jupiter as seen by the *Galileo* orbiter. The halo, which lies interior to the main ring, is not labeled here. Image PIA01623 (NASA/JPL/Cornell University).

The inner halo is unique among Solar System rings for its tremendous vertical extent. It extends radially from approximately 90,000 km to 122,000 km from Jupiter ($r_J = 71,492$ km) with a vertical height on the order of 10^4 km (Burns et al., 1999). Its optical depth of 10^{-6} is orders of magnitude lower than the main rings of Saturn. Drag forces likely drive particles from the main ring into this region, where a resonance with Jupiter's powerful magnetic field lifts them vertically (Throop et al., 2004).

The main ring is likely the densest of Jupiter's rings. Although its normal optical depth of about 10^{-6} is commensurate with that of the halo, main ring particles are confined to a region no more than several hundred kilometers in height (Ockert-Bell et al., 1999). At its interior is a smooth transition to the halo, while its outer boundary lies in the vicinity of the orbits of Metis and Adrastea at around 129,000 km. Micrometeoroid bombardment of these two moons is the most plausible source for the ring material, although embedded Metis (a =127,980) also serves as a sink for particles.

The diffuse ($\tau \approx 10^{-7}$) gossamer rings like exterior to the main ring. Originally identified as one ring in *Voyager* observations, later data revealed the presence of two distinct rings corresponding to the orbits of the moons Amalthea and Thebe. These rings are intermediate in thickness likely due to the slight inclination of their source satellites (Burns et al., 1999). All regions of the Jovian rings have loss timescales on the order of 10^6 years or shorter, with particles 1 μm in size disappearing in as few as 100 years. This indicates that the dust production process must be ongoing.

The best Saturnian analogue to the Jovian rings is probably the enormous Phoebe ring. Like the gossamer rings, the Phoebe ring has substantial vertical extent caused by the inclination of its source. Like the Jovian main ring, particles from the Phoebe ring likely migrate inwards due to drag (Verbiscer et al., 2009). And, like all the Jovian rings, it is caused by micrometeoroid impact on a moon. Saturn's G ring is also sustained through micrometeoroid impact, although there is likely far more than one impacted body (Hedman et al., 2007b).

1.6.2 Uranian rings

The rings of Uranus are the second most extensive of the Solar System, but their character is quite different than those of Saturn. Unlike Saturn's bright, broad rings, Uranus possesses a series of narrow, dark ones. The planet's 13 known rings, from interior to exterior, are ζ, 6, 5, 4, α, β, η, γ, δ, λ, ϵ, ν, μ. Most of the rings are eccentric and inclined with an albedo in the vicinity of 0.05 (Smith et al., 1986).

The narrow nature of the Uranian rings seems contrary to the expectation that they should viscously spread (see section 1.5 for further discussion on ring spreading). This lead to the development of theory surrounding the confinement of narrow rings, most notably through shepherding of nearby satellites. However, only one set of shepherding moons (Cordelia and Ophelia bracket the ϵ ring) has yet been discovered. Unlike Jupiter and Saturn, Uranus has not had an orbiting mission capable of exhaustively discovering small moons. Recent reanalysis of *Voyager* occultations by Chancia and Hedman (2016) gives indirect evidence for satellites on the order of 2-4 km in the vicinity of the α and β rings. These sizes are at the detection limit of *Voyager* images.

Evidence suggests that the Uranian rings are not primordial. Colwell and Esposito (1992) estimate the collisional lifetimes for Uranus' small satellites to be on the order of 10^8 years, which suggests the rings could have formed from the scattered debris of such a collision.

The F ring is the only ring of Saturn confined by shepherd satellites (Pandora and Prometheus). Much of its dynamic structure has been attributed to the close proximity of Prometheus, which strongly perturbs the nearby ring (Murray et al., 2005, 2008; Beurle et al., 2010). Perhaps the ϵ ring experiences similar disruption.

1.6.3 Neptunian rings

The rings of Neptune may be the most perplexing in the Solar System. Like those of Uranus, they are a series of narrow, confined bands. Embedded within the most prominent of these (the Adams ring) is a series of denser regions known as "arcs" (Smith et al., 1989). These arcs were the only portion of the rings initially discovered via ground-based observations, leading to substantial puzzlement as to the nature of the Neptunian rings. A *Voyager* image of the arcs can be seen in figure 1.6.

Two moons nearby the rings (Galatea and Despina) may serve as at least partial shepherds to confine the narrow rings. The confinement mechanism for the arcs, which have an optical depth about three times that of the background Adams ring ($\tau \approx 0.011$) (Horn et al., 1990). One plausible possibility is that a high-order resonance with neighboring Galatea could provide numerous stable points within the ring, about which pockets of material could collect and orbit, causing the enhanced optical depth of these regions (Goldreich et al., 1986; Porco, 1991; Namouni and Porco, 2002). Earth-based observations carried out since the *Voyager* flyby in 1989, however, have revealed that the arcs move in ways inconsistent with resonant confinement (Dumas et al., 1999; Sicardy et al., 1999; de Pater et al., 2005).

The low albedo of the rings is similar to that of the nearby moons (Smith et al., 1989) and thus the rings of Neptune seem consistent with an origin similar to that of the Uranian rings. If two moons collided in the past, they would have spread both small particles and larger fragments throughout the system. If several of these fragments became trapped in resonance with Galatea, they could sustain the arcs through micrometeoroid bombardment (Esposito, 2006).

Saturn's G ring also contains an arc and, like those of Neptune, it is likely constrained by a resonance with a satellite (in this case, with the moon Mimas). *Cassini* observations indicate that in this region lie a population of meter-sized objects that, in total, amount to the mass of a 100-m moonlet (Hedman et al., 2007b). Particle collisions with these objects

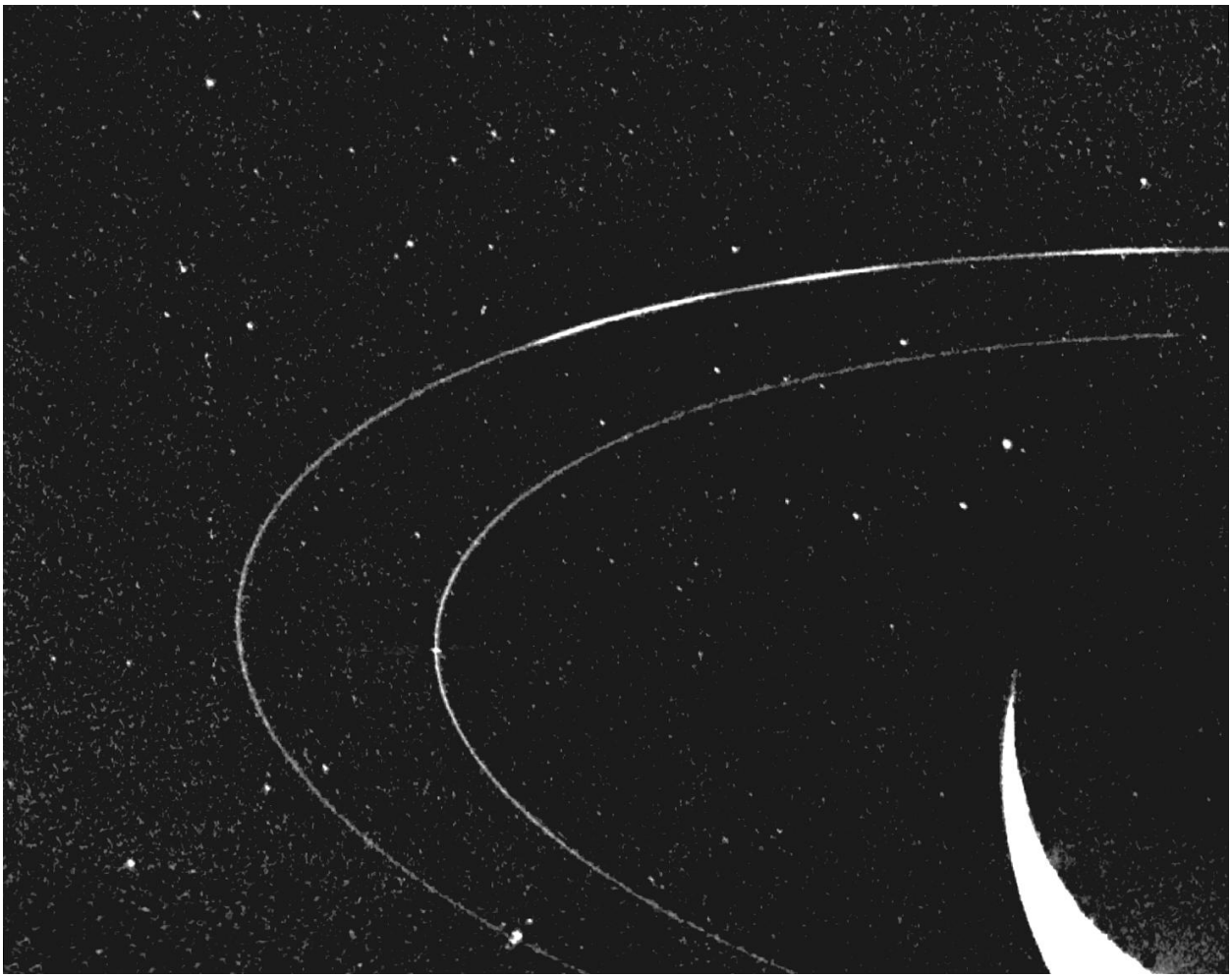

Figure 1.6: A *Voyager* image of the arcs embedded in Neptune's Adams ring. Image PIA01493 (NASA/JPL)

generate debris which brightens the arc and may sustain the entirety of the G ring.

1.6.4 Centaur rings

An exciting recent development is the discovery of rings around objects other than planets. Two such objects, both centaurs orbiting between Saturn and Uranus, are currently known. Of the two, the first discovered and best characterized system is that around 10199 Chariklo. It was found as a result of a 2013 stellar occultation observed from several locations on the Earth (Braga-Ribas et al., 2014). Intriguingly, this 124-km object has not one, but two distinct rings.

The inner ring ($a = 391$ km) has a width of 7 km, while the outer one ($a = 405$ km) is 3 km across. With optical depths of 0.4 and 0.06, respectively, these rings bear a greater resemblance to those of Saturn and Uranus than those of Jupiter or Neptune. With an estimated surface mass density of 300-1000 kgm^{-3}, the physics of these rings might resemble those of Saturn's A ring. Their narrow shape may also point to unseen shepherd moons.

Hedman (2015) has noted that all known dense rings in the Solar System seem to fall between 8 and 20 AU from the Sun. He points out that the rings of Saturn, Uranus, and Chariklo all have temperatures around 70 K and suggests that perhaps the physical nature of water ice at the temperature is particularly suited to forming rings that are dense without accreting into solid objects. If we continue to discover additional ringed objects in the Solar System, we may soon begin to understand which features are common to many environments and which are the result of individual circumstances.

1.6.5 Extrasolar planetary rings

The most important 21st century development in astronomy is the tremendous acceleration in the detection of planets around other stars. The nature of the known extrasolar systems is so varied that it has required a substantial rethinking of the way planetary systems form and evolve. One aspect of stellar systems which has yet to prove particularly fruitful,

unfortunately, is planetary rings. That rings around extrasolar planets are extremely difficult to detect should not be altogether surprising, given the difficulty of finding them even in our own Solar System. The rings of Jupiter, for example, where not discovered until the arrival of space probes and they are as few as 4 AU away!

At least one exoplanet with a ring system has been discovered. The pre-main sequence star 1SWASP J140747.93?-94542.6 hosts a large planet or brown dwarf with large and complex rings (Mamajek et al., 2012).These rings lead to three orders of magnitude of extinction during a transit and appear to extend out to at least 15% of the planet's Hill sphere, meaning they extend far beyond the Roche limit (Kenworthy et al., 2015). This young system may offer a glimpse of what rings look like prior to accreting beyond the Roche zone into solid satellites.

An understanding of ring-moon systems derived from studies of the Solar System's rings may prove vital to understanding the nature of exoplanetary systems. The existence of a large gap in a ring (*a la* the Cassini division) may reveal the presence of an unseen outer moon. A narrow ringlet may indicate small shepherd satellites too tiny to measurably affect a transit.

1.6.6 Astrophysical disks

Not only are the increasing number of known exoplanets interesting for the rings they may possess, but also for the protoplanetary disks out of which they formed. It's important at this juncture to point out that protoplanetary disks differ substantially from all known ring systems and especially the one at Saturn. For one, the dominant constituent of disks surrounding young stars is gas, a feature not present in meaningful quantities in rings. Thus, although we commonly model dense rings as fluids, their microscopic nature is fundamentally different. Another feature common to at least the vast majority of protoplanetary disks is the presence of a strong magnetic field. A coupling between magnetic field and gas often drives the large-scale dynamics of these disks. In comparison, the rings of Saturn behave

largely as if not in the presence of such a field.

Still, a better understanding of one kind of disk will surely benefit the study of other kinds. As mentioned before, the theory used to model density waves in Saturn's rings was first developed to account for the spiral arms of galaxies. Recent observations, for example by Pérez et al. (2016), show that ALMA is capable of detecting spiral density waves in disks around young stars. Like in the case of exoplanetary rings above, these waves may reveal the presence of unseen massive bodies.

1.7 Stellar occultations

Stellar occultations, in which a star is observed passing behind the object of interest, have long been a staple of planetary science. They offer unparalleled spatial resolution at distance at the relative penalty of not being able to pick and choose your observational parameters. This work derives its data nearly entirely from occultations and in this section we will discuss the method in detail.

Traditionally, occultations are observed from one or more locations on the surface of the Earth. The straight line from a point on the Earth to the star defines whether a not an occultation can be observed. If this line is obscured by the intervening phenomenon, the occultation can be observed; if not, another location must be found. Since most of the Earth is covered in water, this limits which occultations can be observed and for how long. Airborne telescopes like SOFIA and orbiting telescopes like *Hubble* can help ameliorate these issues, but Earth and its orbit are still very limited in their perspective. One must often wait a considerable amount of time before a star happens to pass behind the object of interest in our line of sight. A spacecraft in orbit about the phenomenon offers substantially increased flexibility in finding an appropriate star. This is especially true for a spacecraft like *Cassini*, which has undergone many orbital maneuvers during its nearly 13-year mission (see figure 1.7).

No star is observed more than once per *Cassini* orbit and so it is common practice

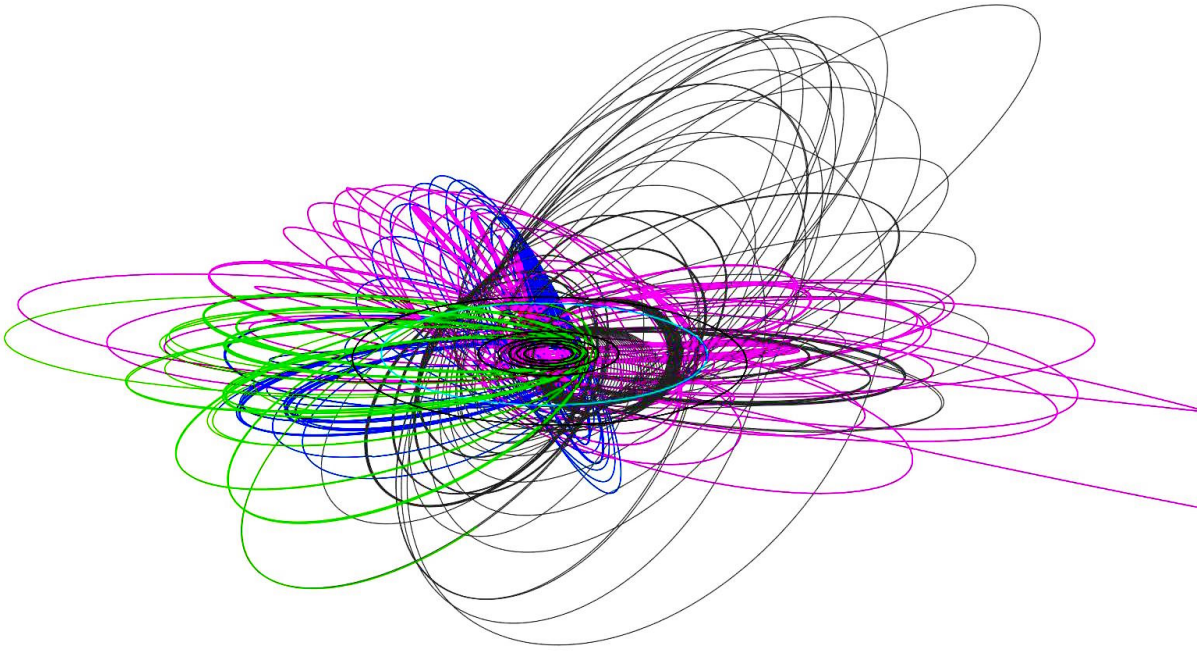

Figure 1.7: A NASA visualization of the orbit of *Cassini* between Saturn orbit insertion (30 June 2004) through the end of the mission (15 Sept 2017). Saturn is located at the center. Note the changing inclination and eccentricity of the orbit, which enable the observation of occultations of many stars.

to name an observation by the star occulted and the orbit ("rev") in which the observation occurred. Occultations that begin at a larger radial distance from Saturn than they end are called "ingress" observations. The reverse are called "egress" observations. Some occultations first go in one direction before turning around and going in the other. In these instances, we append "in" or "out" to distinguish between the two. Thus, every named observation represents exactly one cut through a portion of the rings traveling in one direction. For example, Bet_Cen_R105_in is the ingress portion of an occultation of the star β Centauri during *Cassini* orbit 105.

1.7.1 High Speed Photometer

The data for this investigation consist primarily of stellar occultations observed by the *Cassini* Ultraviolet Imaging Spectrograph (UVIS) High Speed Photometer (HSP). The instrument is described in detail by Esposito et al. (2004).

The HSP is a discrete optical train within UVIS designed to make rapid photometric observations of target stars whilst they are being occulted by the phenomenon in question. With a bandpass of approximately 110-190 nm, HSP is designed to observe bright O and B stars (see table 1.3 for a list of observed stars). A field of view of 6 mrad ensures that the photometer remains evenly illuminated even with non-ideal errors in spacecraft pointing. The photometer can sample at a variable rate from 1 to 8 ms and this rate is fixed for the duration of an observation. The sampling rate, in addition to occultation geometry and the relative motions of *Cassini* and the rings, gives the spatial resolution of the observation and can be set as rapid as the anticipated data volume permits. For the observations used in this work, an integration period Δt of 1 or 2 ms is typical.

Over the course of the mission, the sensitivity of the HSP has decreased. This manifests itself as both an absolute decrease in sensitivity and a slower response time when first engaged. The latter is described in the following section and the former is illustrated in figure 1.8. Over a three-year period, the sensitivity fell by a factor of four. Since then, the

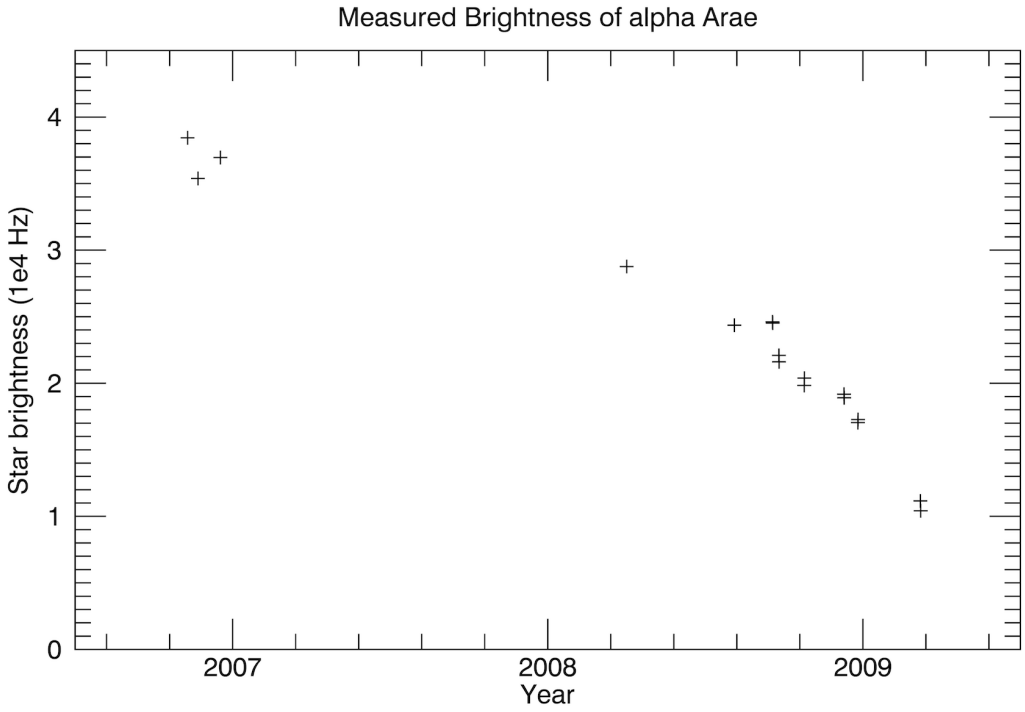

Figure 1.8: The brightness of α Arae from 2006 through 2009, illustrating the decreasing sensitivity of HSP. The rate of sensitivity loss has slowed over time.

rate of decreasing sensitivity has slowed. Since UVIS observes primarily bright stars, this loss in sensitivity has not seriously impacted the usefulness of the HSP.

Table 1.3: A summary of stars observed by HSP. Ingress and egress parts of double occultations are counted separately.

Star	Abbreviation	# of observations
3 Centauri	3_Cen	1
126 Tauri	126_Tau	2
α Arae	Alp_Ara	22
α Canis Majoris	Alp_CMa	2
α Crucis	Alp_Cru	4
α Leonis	Alp_Leo	2
α Lupi	Alp_Lup	2
α Lyrae	Alp_Lyr	4
α Pavonis	Alp_Pav	1
α Scorpii	Alp_Sco	9
α Sexantis	Alp_Sex	2
α Virginis	Alp_Vir	15
β Centauri	Bet_Centauri	15
β Canis Majoris	Bet_CMa	1
β Crucis	Bet_Cru	3
β Hydrae	Bet_Hya	1
β Librae	Bet_Lib	3
β Lupi	Bet_Lup	2
β Orionis	Bet_Ori	3

Star	Abbreviation	# of observations
β Persei	Bet_Per	3
β Picis Austrini	Bet_PsA	1
β Sagittarii	Bet_Sgr	2
χ Centauri	Chi_Cen	1
δ Aquarii	Del_Aqr	1
δ Centauri	Del_Cen	11
δ Ceti	Del_Cet	2
δ Lupi	Del_Lup	1
δ Persei	Del_Per	5
δ Scorpii	Del_Sco	2
ϵ Cassiopeiae	Eps_Cas	3
ϵ Centauri	Eps_Cen	1
ϵ Canis Majoris	Eps_CMa	4
ϵ Lupi	Eps_Lup	3
ϵ Microscopium	Eps_Mic	1
ϵ Picis Austini	Eps_PsA	4
ϵ Sagittarii	Eps_Sgr	2
η Lupi	Eta_Lup	2
γ Arae	Gam_Ara	3
γ Cassiopeiae	Gam_Cas	2
γ Cancri	Gam_Cnc	2
γ Columbae	Gam_Col	3
γ Gruis	Gam_Gru	5
γ Lupi	Gam_Lup	4
γ Orionis	Gam_Ori	2
γ Pegasi	Gam_Peg	6

Star	Abbreviation	# of observations
ι Centauri	Iot_Cen	2
ι Orionis	Iot_Ori	1
κ Centauri	Kap_Cen	5
κ Canis Majoris	Kap_CMa	2
κ Orionis	Kap_Ori	1
κ Scorpii	Kap_Sco	1
κ Velorum	Kap_Vel	1
λ Aquilae	Lam_Aql	2
λ Ceti	Lam_Cet	1
λ Scorpii	Lam_Sco	4
λ Tauri	Lam_Tau	2
μ Centauri	Mu_Cen	1
μ Picis Austini	Mu_PsA	4
μ Scorpii	Mu_Sco	2
μ Sagittarii	Mu_Sgr	2
ν Centauri	Nu_Cen	2
π^4 Orionis	Pi4_Ori	1
ψ Centauri	Psi_Cen	2
b Centauri	SAO_205839	1
σ Sagittarii	Sig_Sgr	4
θ Arae	The_Ara	3
θ Carinae	The_Car	2
θ Hydrae	The_Hya	8
ξ^2 Ceti	Xi2_Cet	1
ζ Centauri	Zet_Cen	4
ζ Canis Majoris	Zet_CMa	2

Star	Abbreviation	# of observations
ζ Ophirchi	Zet_Oph	1
ζ Orionis	Zet_Ori	3
ζ Persei	Zet_Per	2
ζ Puppis	Zet_Pup	4

1.7.2 Geometry of a stellar occultation

There are three basic components to an HSP observation: the measured stellar photon count during the occultation $I\Delta t$, the observed unocculted stellar photon count $I_0\Delta t$, and the contribution of background sources $b\Delta t$. For one sampling period, $I = I_0 e^{-\tau} + b$, for ring's optical depth τ. The photon count $I\Delta t$ is the quantity measured as a time series by the photometer. Ideally, I_0 is a constant (ignoring stellar variability), but, in reality, the instrument becomes more sensitive during the course of an observation (Colwell et al., 2007). This effect is known as "ramping up." Fortunately, this work is not attempting to make absolute photometric measurements and, over short distances (hundreds of kilometers), the effects of ramping up are not large. Since b should not contain any contribution from the target star's flux, we measure it when the target star is occulted by an opaque region of the rings.

Raw HSP data files contain two vectors: the observed counts $I\Delta t$ and the times at which each data entry was recorded. The time vector can be converted to vectors of ring radii and ring longitude through knowledge of the position and orientation of the spacecraft, planet, and star. The plane of the rings is defined as the planet's equatorial plane, with longitude measured prograde from the ascending node of Saturn's equatorial plane on Earth's J2000 equator. This information can be obtained from the reconstructed SPICE kernels and

geometric calculations are performed[1] with the method described by Albers et al. (2012).

There are three important angles when evaluating a *Cassini* stellar occultation: the elevation angle B, the viewing angle ϕ_{view}, and the track angle ϕ_{track}. All stem from the line of sight from the spacecraft to the occulted star. The occultation "footprint" is the term used for the projection of the star on the rings at the point where the line of sight pierces the ring plane. Figure 1.9 diagrams an occultation.

The elevation angle B describes how steep or shallow the observation is, where $B = 0°$ indicates an (unrealistic) edge-on view and $B = 90°$ indicates a top-down view in which the spacecraft and star are on exactly opposite sides of the ring. This angle is taken to be approximately constant during a single observation. The lower the elevation angle, the more ring material starlight must pass through and the dimmer the star will appear. Small uncertainties in the geometry of the observation also propagates to larger uncertainty in the radial position of the footprint for observations with a small B. As it doesn't generally matter whether the spacecraft is facing the lit or unlit side of the rings during an occultation, B is expressed as a positive number.

The viewing angle ϕ_{view} describes where the spacecraft is looking relative to the local radial direction. This is useful for understanding how the observed starlight is interacting with structures in the rings. For example, if there was a radial gap in the rings, an observation with $\phi_{\text{view}} = 0°$ would be looking directly along it and starlight would not be occulted (assuming $B > 0$). This angle is symmetrical about 180°, so observations with $\phi_{\text{view}} = 90°$ and $\phi_{\text{view}} = 270°$ would both be looking perpendicular to the aforementioned gap. This viewing angle typically changes moderately during an observation and is computed for every integration period.

The track angle ϕ_{track} describes the path the occultation footprint traces relative to the local radial direction. If $\phi_{\text{track}} = 0°$, the occultation is cutting radially outwards from Saturn, while $\phi_{\text{track}} = 90°$ implies it is moving tangentially (in the direction in orbital motion). This

[1] Geometry code provided by M. Sremčević

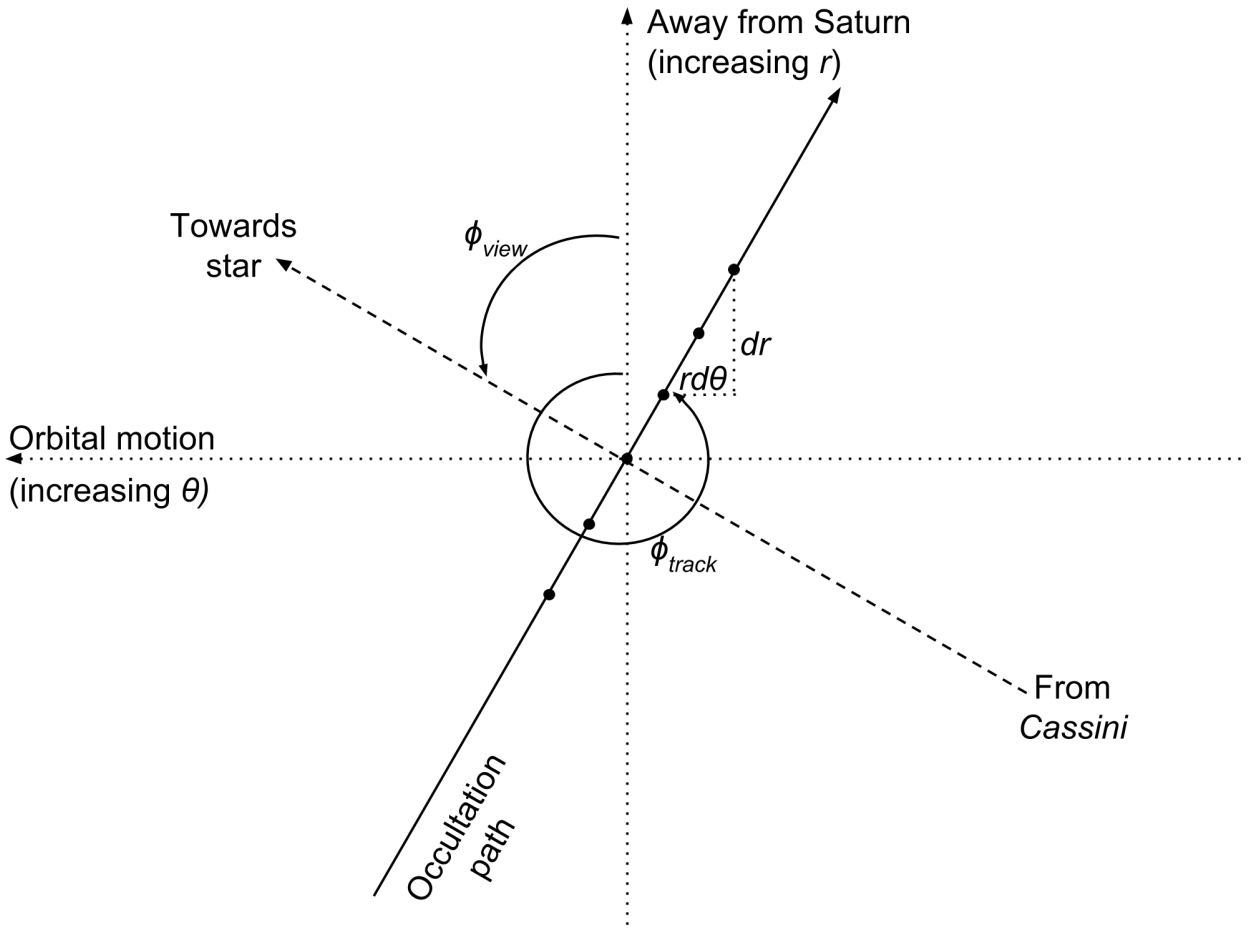

Figure 1.9: A top-down view of the rings illustrating $\phi_{\rm view}$ and $\phi_{\rm track}$. Each dot represents the location of the occultation footprint at one integration period and the dashed line representing the line of sight is projected into the ring plane. Both angles are measured in the positive direction from the positive radial axis.

is useful for determining whether an occultation is traveling along a ring feature with a given orientation. The track angle can change substantially during an observation and it computed for every integration period.

1.7.3 Optical depth

By rearranging the above formula for optical depth τ and correcting for the elevation angle B, we find the formula used to convert data counts to normal optical depth:

$$\tau_{\perp} = \tau \sin B = \ln \left[\frac{I_0}{I - b} \right] \sin B. \tag{1.18}$$

This formula is valid for $I_0 > 0$ (always true) and $I - b > 0$ (not always true). Because of photon counting statistics, sometimes $b \geq I$ for a given data point. The natural logarithm is undefined for negative values and unbounded as its argument tends to infinity. We account for this by placing a floor on $I - b$, namely $\max((I - b)\Delta t, 1)$. This has the effect of creating a maximum optical depth for observations with low photon counts.

1.8 The remainder of this work

The following chapters will examine structural elements of Saturn's rings on increasingly-small scales. In chapter 2, I will describe a traveling, wave-like structure resulting from the cyclical orbital motion of Janus and Epimetheus. This phenomenon, not previously theorized, demonstrates the dramatic effect the motion of massive bodies can have on the rings. In chapter 3, I will extend previous work to characterize the population of temporary aggregates ("kittens") found in the F ring and demonstrate that prior conceptions as to their physical parameters are not consistent with other observations of the rings. In chapter 4, I will give the results of the first comprehensive search for the tenuous gap regions at the minima of self-gravity wakes. I will show that these detected structures account for the long-observed brightness asymmetry of the main rings. Finally, in chapter 5, I will draw overall conclusions about the small-scale nature of Saturn's rings.

Chapter 2

A Solitary Wave Launched at Janus Resonances

2.1 Introduction

Cassini investigations of the rings of Saturn have revealed a rich collection of phenomena both secular and transient. One of the most important drivers of processes in the rings is the gravitational influence of a subset of Saturn's more than 60 moons. Two of these moons are particularly dynamic: co-orbitals Janus and Epimetheus. Every 4.0 years, they migrate radially and switch their positions relative to the planet. When this migration occurs, so too move the resonance locations between the rings and the two moons. Tiscareno et al. (2006b) have described the effects of this swap on overlapping linear spiral density waves, but stellar occultations observed by *Cassini* at various times during this process have revealed that the nonlinear density waves do not respond in the same way. We investigate that phenomenon here. The work presented in this chapter has been published in Rehnberg et al. (2016).

2.1.1 Resonances and spiral density waves

Saturn's numerous moons provide for a large number of inner Lindblad resonances within the A and B rings. Lissauer and Cuzzi (1982) give the condition for such a resonance as:

$$m(\Omega_p - n) = -\kappa, \tag{2.1}$$

Parameter	Value
GM_{Saturn}	37931207.7 km^3s^{-1}
r_{Saturn}	60,330 km
J_2	1.629071×10^{-2}
J_4	-9.3583×10^{-4}
J_6	8.614×10^{-5}
J_8	-1×10^{-5}
$n_{\text{Jan, in}}$	1.04708751×10^{-4} s^{-1}
$n_{\text{Jan, out}}$	1.04687109×10^{-4} s^{-1}
$n_{\text{Epi, in}}$	1.04736844×10^{-4} s^{-1}
$n_{\text{Epi, out}}$	1.04658870×10^{-4} s^{-1}

Table 2.1: The parameters used to compute the resonance locations specified in this work. All except the mean motions of Janus and Epimetheus are taken from Jacobson et al. (2006).

where $m\Omega_p = mn_s + k\kappa_s$ is an integer multiple of the angular speed Ω_p with which the gravitational potential of an orbiting, exterior satellite with no inclination rotates. It is given in terms of n_s, the satellite's mean orbital angular velocity and κ_s, the radial, or epicyclic, frequency of its orbit. The numbers n and κ represent the same quantities for a test particle within the rings. The coefficients m and k are integers, with m specifying the number of spiral arms the resonance will create. To first order, $n \approx \kappa,\ n_s \approx \kappa_s$ and we can rewrite equation 2.1 as

$$(m + k)n_s = (m - 1)n. \tag{2.2}$$

This leads to the common practice of labeling resonances as $(m + k) : (m - 1)$.

In order to precisely compute locations of resonances within the rings, however, we must not make approximations like $n_s \approx \kappa_s$ and instead compute them separately based on a more complete model of Saturn. This is necessary because of Saturn's oblateness; if the planet were a perfect sphere, then $n_s = \kappa_s$. We use the method of Lissauer and Cuzzi (1982) to compute precise locations for the resonances. Table 2.1 lists the parameters used in these computations.

At many of these resonance locations, features are excited within the rings. Lin and Shu (1964) were the first to develop a theory of density waves to explain the spiral structure of many galaxies, thus giving the phenomenon its name. Later, Goldreich and Tremaine (1982) and Shu (1984) were among the first to apply the theory to explain the structure of Saturn's rings. Linear density waves are raised by weaker resonances as small perturbations on the background surface mass density of the rings. Stronger resonances generate larger perturbations, which can be of the same order as the background density. When this occurs, a nonlinear density wave forms, with sharp peaks (regions of highest density) and shallow troughs (regions of lowest density). The predator-prey model of Esposito et al. (2012) identified strongly-perturbed regions such as nonlinear density waves as a likely site of increased aggregation within the rings.

2.1.2 Surface mass density in the A and B rings

Using images of spiral density waves observed with the *Cassini* Imaging Science Subsystem (ISS), Tiscareno et al. (2007) derive an approximate surface mass density for the A ring of 40 g/cm^2. This surface density appears to increase as one moves farther from the planet.

Esposito et al. (1983) used a *Voyager* occultation of the Janus 2:1 spiral density wave to estimate a surface mass density for the inner B ring of 70$\pm$10 g/cm^2. This is somewhat larger than the results of Reffet et al. (2015), who use *Cassini* CIRS observations to estimate a value on the order of 40 g/cm^2 for the inner B ring, 100 g/cm^2 for the middle of the ring and 50 g/cm^2 towards the outer boundary. The results of Hedman and Nicholson (2016) bridge this gap by finding that the surface mass density varies within the Janus 2:1 resonance from 69 g/cm^2 near resonance to 47 g/cm^2 several hundred kilometers exterior. These values are all substantially lower than an estimate that considers the dynamics and aggregation of ring particles by Robbins et al. (2010) of 240-480 g/cm^2.

The background surface mass density σ_0 strongly governs the group velocity v_g of spiral

density waves excited at resonance locations, given by $v_g = \frac{\pi G \sigma_0}{\kappa}$, for epicyclic frequency κ and gravitational constant G (Toomre, 1969). For this study, we assume a surface mass density of 40 g/cm^2 for the A ring and as a lower limit for the B ring. We take 70 g/cm^2 as an upper limit for the B ring in the vicinity of the Janus 2:1 resonance.

2.1.3 Janus and Epimetheus

Among Saturn's many moons, Janus and Epimetheus are of particular interest because they represent the only pair of co-orbiting satellites in the solar system. Dermott and Murray (1981) showed that this co-orbital configuration leads to each moon traversing a horseshoe orbit about the pair's shared mean orbital radius of 151,450 km in a frame of reference rotating with their mean angular velocity. This gives a small relative velocity between the two. Every 4.0 years, the pair approach each other within 15,000 km (Nicholson et al., 1992) and exchange orbital angular momentum. This causes a rapid shift, in which the inner and outer bodies switch position in the course of approximately 100 days. Each moon is radially shifted in proportion to its relative mass ($m_E/m_J = 0.278$): 20 km for Janus and 80 km for Epimetheus. During *Cassini's* time at Saturn, this has occurred three times: 21 January 2006 (Janus moves inwards), 21 January 2010 (Janus moves outwards), and 21 January 2014 (Janus moves inwards).

Because of this change in the radius of their orbits, special care must be taken when computing the mean motions (and thus the pattern speeds and resonance locations) of these bodies. The semi-major axes given in table 2.2 are valid only for times distant from the orbital swap; during the swap, the values evolve continuously. Table 2.3 lists the computed resonance locations for the first-order Janus and Epimetheus resonances used in this study.

Although the focus of this work is the effect that the Janus/Epimetheus orbital swap has on spiral density waves raised within the rings, El Moutamid et al. (2016) have also observed that changes in the Janus 7:6 resonance affect the shape of the outer edge of the A ring.

Name	M (kg) [1]	a (km) [2]	i (°) [3]	e [3]
Epimetheus	5.3×10^{17}		0.351	0.0098
2002-2006, 2010-2014		151,410		
2006-2010, 2014-2018		151,490		
Janus	1.9×10^{18}		0.163	0.0068
2002-2006, 2010-2014		151,460		
2006-2010, 2014-2018		151,440		

[1]Thomas (2010), [2]Jacobson et al. (2008), [3]Spitale et al. (2006)

Table 2.2: Basic properties of Janus and Epimetheus. Values with specified dates refer to 21 Jan of that year and are not accurate in the immediate vicinity (approximately 100 days) of those end points.

2.2 Data

The data for this investigation consist primarily of stellar occultations observed by the *Cassini* Ultraviolet Imaging Spectrograph (UVIS) High Speed Photometer (HSP). The instrument is described in detail by Esposito et al. (2004).

The HSP is a discrete optical train within UVIS designed to make rapid photometric observations of target stars whilst they are being occulted by the phenomenon in question. With a bandpass of approximately 110-190 nm, HSP is designed to observe bright O and B stars. A field of view of 6 mrad ensures that the photometer remains evenly illuminated even with non-ideal errors in spacecraft pointing. The photometer can sample at a variable rate from 1 to 8 ms and this rate is fixed for the duration of an observation. The sampling rate, in addition to occultation geometry and the relative motions of *Cassini* and the rings, gives the spatial resolution of the observation and can be set as rapid as the anticipated data volume permits. For the observations used in this work, an integration period Δt of 1 or 2 ms is typical.

There are three basic components to an HSP observation: the measured stellar photon count during the occultation $I\Delta t$, the observed unocculted stellar photon count $I_0\Delta t$, and the contribution of background sources $b\Delta t$. For one sampling period, $I = I_0 e^{-\tau} + b$, for

Resonance	Time period	r_{res} (km)	n_{occ}	n_{features}	n_{empty}
Epimetheus 6:5			152	-	-
	2002-2006, 2010-2014	134,223			
	2006-2010, 2014-2018	134,289			
Epimetheus 5:4			151	-	-
	2002-2006, 2010-2014	130,660			
	2006-2010, 2014-2018	130,724			
Epimetheus 4:3			142	-	-
	2002-2006, 2010-2014	125,228			
	2006-2010, 2014-2018	125,290			
Epimetheus 3:2			132	-	-
	2002-2006, 2010-2014	115,922			
	2006-2010, 2014-2018	115,979			
Epimetheus 2:1			103	-	-
	2002-2006, 2010-2014	96,216			
	2006-2010, 2014-2018	96,263			
Janus 6:5			152	92	50
	2002-2006, 2010-2014	134,265			
	2006-2010, 2014-2018	134,247			
Janus 5:4			151	110	33
	2002-2006, 2010-2014	130,701			
	2006-2010, 2014-2018	130,683			
Janus 4:3			142	127	19
	2002-2006, 2010-2014	125,267			
	2006-2010, 2014-2018	125,250			
Janus 3:2			132	1	104
	2002-2006, 2010-2014	115,959			
	2006-2010, 2014-2018	115,943			
Janus 2:1			103	177	5
	2002-2006, 2010-2014	96,246			
	2006-2010, 2014-2018	96,233			
Mimas 5:3		132,298	151	7	139
Prometheus 31:30		136,389	146	0	130
Prometheus 14:13		132,716	153	0	141

Table 2.3: Inner Lindblad resonance locations used for this work. The orbit swap of Janus and Epimetheus means that the resonance location shifts on 21 January of the specified years. The number of examined occultations n_{occ} does not equal the sum of observed features n_{features} and occultations with no observed features n_{empty} because some occultations contain multiple features and some have a signal-to-noise ratio too low to resolve the density wave. Because the Epimetheus resonance regions overlap the (much stronger) Janus ones, they were not independently searched for anomalous features.

ring's optical depth τ. The photon count $I\Delta t$ is the quantity measured as a time series by the photometer. Ideally, I_0 is a constant (ignoring stellar variability), but, in reality, the instrument becomes more sensitive during the course of an observation (Colwell et al., 2007). This effect is known as "ramping up." Fortunately, this work is not attempting to make absolute photometric measurements and, over short distances (hundreds of kilometers), the effects of ramping up are not large. Since b should not contain any contribution from the target star's flux, we measure it when the target star is occulted by an opaque region of the rings.

Raw HSP data files contain two vectors: the observed counts $I\Delta t$ and the times at which each data entry was recorded. The time vector can be converted to vectors of ring radii and ring longitude through knowledge of the position and orientation of the spacecraft, planet, and star. The plane of the rings is defined as the planet's equatorial plane, with longitude measured prograde from the ascending node of Saturn's equatorial plane on Earth's J2000 equator. This information can be obtained from the reconstructed SPICE kernels and geometric calculations are performed with the method described by Albers et al. (2012).

We exclude occultations of the stars α Sextantis and θ Hydrae because the extremely low elevation angle of these observations yields high uncertainty in the geometric solution and a poor signal-to-noise ratio. We estimate the uncertainty of the geometric solution by comparing the location of the inner Encke Gap edge computed by French et al. (1993) with the same feature in each occultation. This yields a 1-σ radial uncertainty of 1.17 km, which is smaller than the size of the plotting symbols used in the figures.

By rearranging the above formula for optical depth τ and correcting for the elevation angle B, we find the formula used to convert data counts to normal optical depth:

$$\tau_\perp = \tau \sin B = \ln\left[\frac{I_0}{I-b}\right] \sin B. \tag{2.3}$$

This formula is valid for $I_0 > 0$ (always true) and $I - b > 0$ (not always true). Because of photon counting statistics, sometimes $b \geq I$ for a given data point. The natural logarithm is

undefined for negative values and unbounded as its argument tends to infinity. We account for this by placing a floor on $I - b$, namely $\max((I - b)\Delta t,1)$. This has the effect of creating a maximum optical depth for observations with low photon counts. Although the presence of self-gravity wakes in the A and B rings may alter $\tau_\perp$ (Colwell et al., 2006, 2007; Hedman et al., 2007c; Ferrari et al., 2009), the search method described in section 2.3 relies only on relative optical depths $\Delta\tau_\perp$.

2.3 Methods

2.3.1 Search regions

Each occultation was examined manually over a region spanning 10 km interior to a calculated resonance to 200 km exterior. In the A ring, larger search regions are inhibited by the presence of other resonance locations. In the B ring, the Janus 2:1 density wave becomes very closely spaced. Janus resonances were selected as the primary region of search because they are substantially stronger than the corresponding Epimetheus resonance. In addition, the same region around the Mimas 5:3 (a very strong second-order resonance), the Prometheus 31:30, and the Prometheus 14:13 resonances were searched as a control. The relative strengths of these resonances are given in table 2.4; all are substantially stronger than those examined by Tiscareno et al. (2006b).

Some occultations are performed such that the star's track on the rings crosses a given radial location twice. While the radial location may be the same, with few exceptions the azimuthal location in a co-rotating frame is (often substantially) different. Thus we treat the ingress and egress observations as two separate, independent occultations.

2.3.2 Selection criteria

The computed optical depth data for each observation were binned to a 500-m resolution to improve the signal-to-noise ratio. Each spiral density wave was then visually

Resonance	$\lvert T^L_{l,m}\rvert$ (cm^4/s^2)
Janus 6:5	7.90×10^{18}
Prometheus 31:30	6.62×10^{18}
Janus 5:4	5.09×10^{18}
Janus 4:3	2.90×10^{18}
Janus 3:2	1.32×10^{18}
Prometheus 14:13	1.24×10^{18}
Mimas 5:3	6.12×10^{17}
Janus 2:1	3.54×10^{17}
Janus 11:9	4.56×10^{16}
Janus 9:7	1.78×10^{16}

Table 2.4: The torque densities computed by Lissauer and Cuzzi (1982) for resonances examined in this study (above dashed line) in comparison to two sample resonances examined by Tiscareno et al. (2006b) (below dashed line).

searched for anomalous features. A feature was deemed anomalous if it met either of two criteria: (type 1) an optical depth greater than that of the crests of the wave or (type 2) a radial position such that the regularity of the wave was disrupted. To eliminate outliers due to photon counting statistics, a detected feature needed to be at least two data elements wide (approximately 1 km in radial width) and (in the case of type-2 detections) have an optical depth at least half that of the adjacent crests of the wave. A feature is said to have disrupted the regularity of the wave if it broke the monotonic decrease in radial distance between subsequent wave crests when included.

2.3.3 Feature characterization

When an anomalous feature is identified, its position (radius and longitude), peak optical depth, width, and time of observation are recorded. With the exception of the width (measured as FWHM), these quantities are measured from the peak of the feature. In the case of features that break the expected periodicity of the wave (type 2), sometimes, especially later in the wave train, it is difficult to distinguish which of two peaks is anomalous. In these instances, the mean radial location of the two is recorded.

2.4 Results

The control regions (Mimas 5:3, Prometheus 31:30, Prometheus 14:13) showed few anomalous features matching the criteria outlined in section 2.3.2 and no correlation between those was observed. The Janus 3:2 region was too optically thick to distinguish the spiral density wave and thus the selection criteria couldn't be applied. Every other searched region (Janus 6:5, Janus 5:4, Janus 4:3, Janus 2:1) resulted in a substantial number of anomalous features. Figure 2.1 illustrates a typical observation without an anomalous feature, while figure 2.2 depicts an occultation containing such a feature.

For each resonance location, we plot the time a feature was observed against its radial position within the rings. Figure 2.3 depicts the results. A clear trend is visible in each

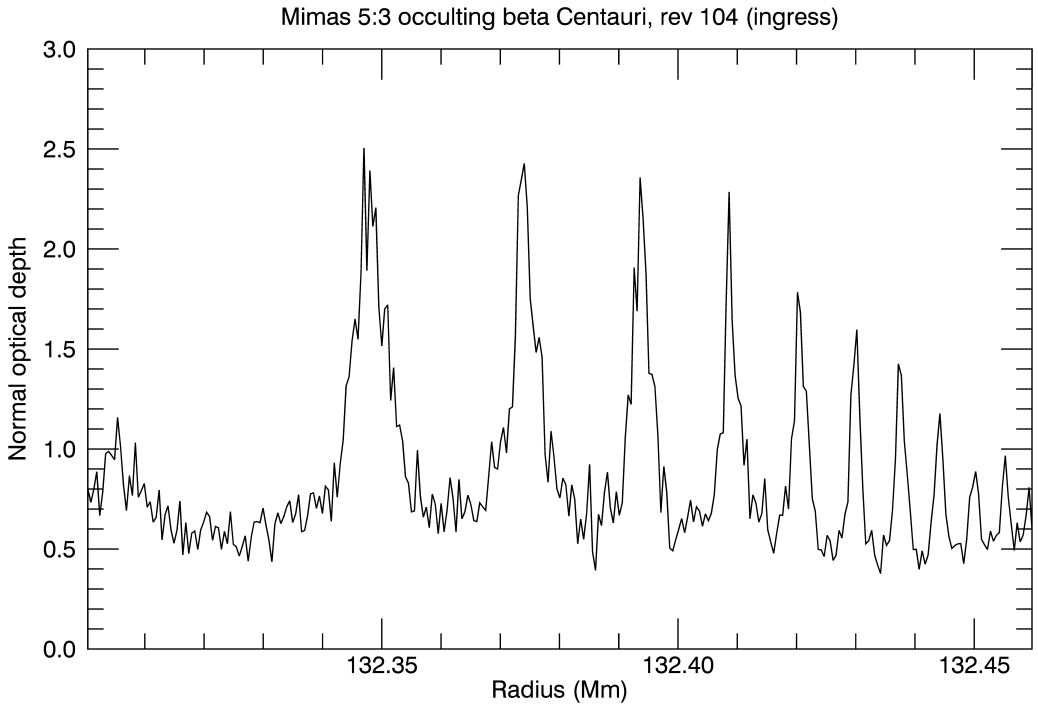

Figure 2.1: A typical nonlinear spiral density wave as seen in an HSP stellar occultation. The data are binned to a radial resolution of approximately 500 meters.

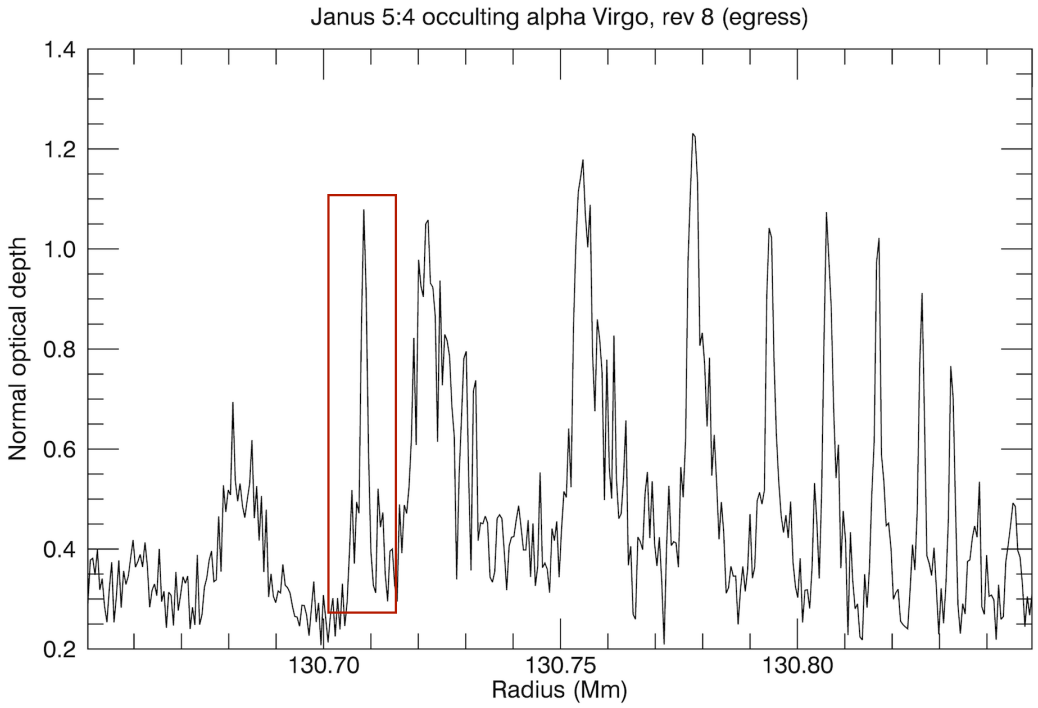

Figure 2.2: An anomalous feature in an HSP stellar occultation of the Janus 5:4 spiral density wave, binned to a radial resolution of approximately 500 meters. The type-2 feature, identified by the red box, clearly breaks the expected regularity of the density wave. The small peak atop the leftmost crest is too narrow to be selected (It would have been a type-1 feature, see section 2.3.2).

Resonance	Feature velocity (km/yr)	DW group velocity (km/yr)
Janus 6:5	39.8±1.6	21[1]
Janus 5:4	39.6±0.85	20[1]
Janus 4:3	45.8±0.60	19[1]
Janus 2:1	19.8±0.55	13[1], 23[2]

[1]assumes $\sigma_0 = 40$ g/cm^2, [2] assumes $\sigma_0 = 70$ g/cm^2

Table 2.5: Velocities derived by assuming each anomalous feature is a detection of the same phenomenon and fitting a line as indicated in figure 2.3. Uncertainty is 1 σ with equal weighting of points. Group velocities are computed for the Janus-in configuration.

region: as time progresses, the radial locations in which anomalous features are detected move outwards. By fitting a line to a coherent collection of detections in each region (indicated in each figure by a solid line), we can compute the velocity with which a single phenomenon would need to move in order to account for the observed detections. Table 2.5 lists these fitted values as well as computed group velocities for the local spiral density wave.

Two trends are readily apparent. First, in the A ring, the "feature velocity" is approximately twice that of the group velocity in the local spiral density wave, while in the B ring these velocities are roughly commensurate. Second, the number of occultations in which no anomalous features are detected (indicated by the circles near the bottom of each panel in figure 2.3 and tabulated in table 2.3) increases as we move to resonances which are farther from Saturn and also stronger.

No correlation was observed between the detection of an anomalous feature and that occultation's longitude relative to Janus. Figure 2.4 depicts the longitudinal coverage of our occultations.

2.5 Discussion

We consider two hypotheses with which to explain the observed results: a population of discrete objects and one or more continuous structures.

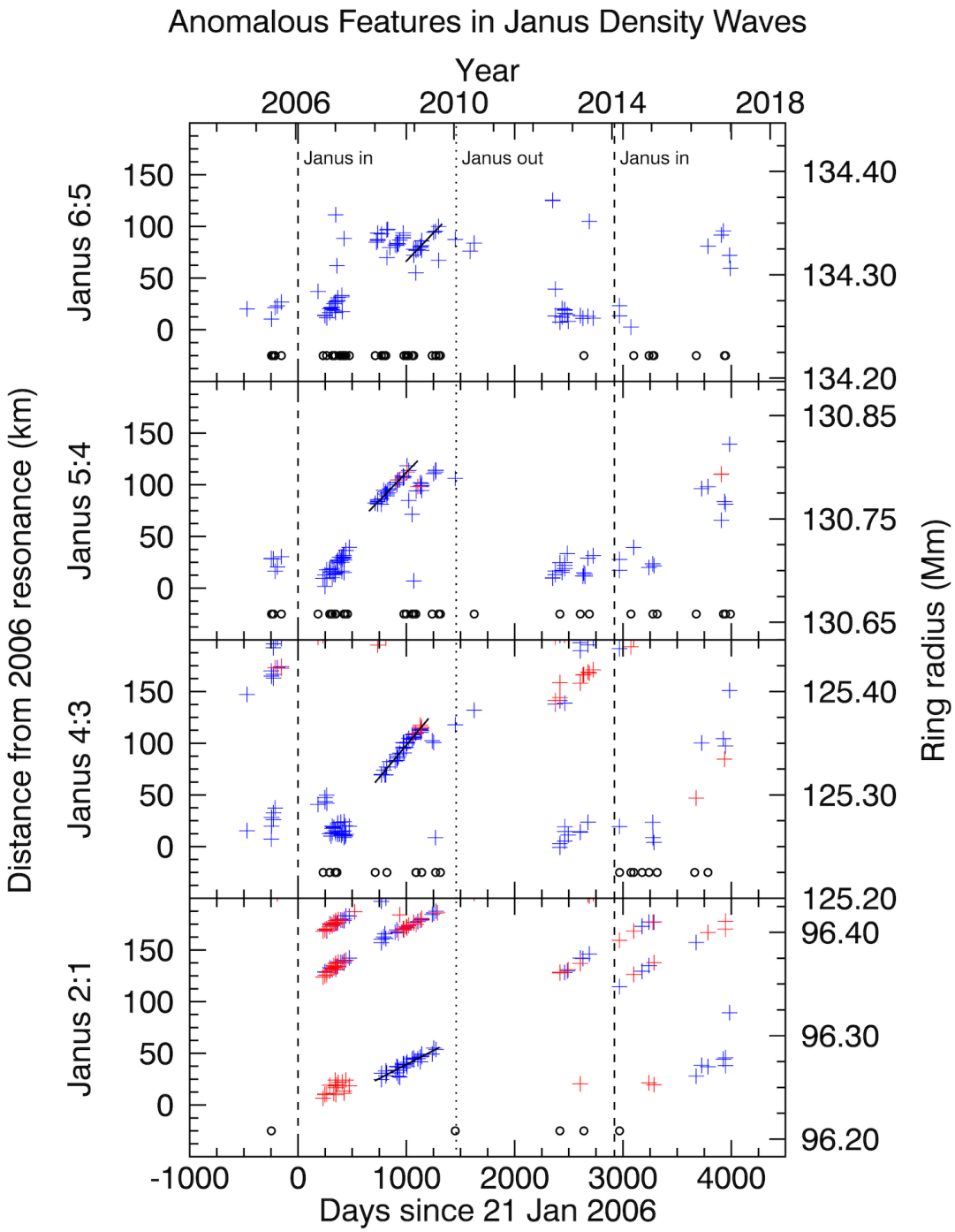

Figure 2.3: Anomalous feature detections in the four Janus resonance search regions. Each detection is indicated by a plus, with blue denoting the radial location of a single peak and red denoting the mean of two neighboring peaks (see section 2.3). The solid line identifies the points fit to derive the velocities given in table 2.5. The circles denote occultations in which no anomalous feature was detected. The 1-σ radial uncertainty of 1.17 km is smaller than the plotting symbols. Note the extended gap in observations between mid 2010 and mid 2012 due to the position of *Cassini* in Saturn's ring plane.

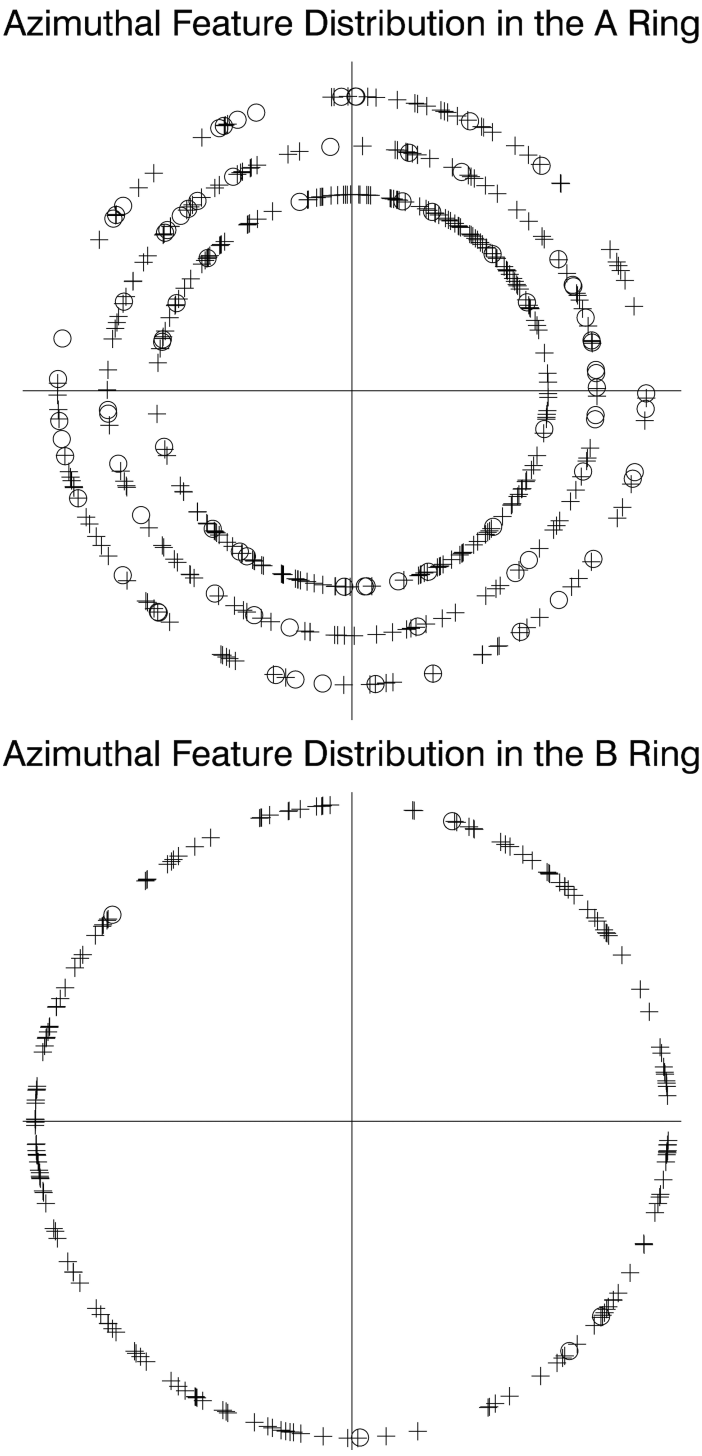

Figure 2.4: The distribution of observed longitudes in a frame co-rotating with the mean motion of the moon. Plusses denote locations in which an anomalous feature was detected. Circles denote locations where no anomalous features were observed. For occultations in which no feature was detected, the longitude at which the occultation crosses the relevant resonance location is used. The A-ring plot is not to radial scale and contains (interior to exterior) the Janus 4:3, Janus 5:4, and Janus 6:5 resonances. The B-ring plot contains the Janus 2:1 resonance..

2.5.1 Hypotheses

Discrete objects are known to exist in both the main (Tiscareno et al., 2006a, 2008) and F (Esposito et al., 2008; Meinke et al., 2012) rings, however none have been observed within the given resonance locations. For such objects to elude detection in ISS images suggests that the size of the object plus any gravitationally-created structure must be smaller than about 500 meters, the approximate best resolution of Narrow-angle Camera (NAC) images. In the Janus 4:3 region, an anomalous feature is detected in 87.6% of occultations of sufficient quality. We can estimate the quantity of objects present in this location with the formula $N = \frac{2\pi a f}{k\bar{d}}$. Setting $a = 125,250$ km at the Janus 4:3 resonance location, the observed detection frequency f to 0.876, the azimuthal elongation factor k to 8.5 (derived from Sremčević et al. (2007)) and the mean object size $\bar{d}$ to 0.5 km, we compute $N \sim 10^5$ objects.

This value seems implausibly large when one considers that these objects appear to migrate out of the resonance region on a four-year timescale. Thus, to sustain such a population would require the generation of 10^5 objects every four years. Observed anomalous features are also greater than 500 meters in radial diameter, suggesting they should be detected in ISS imagery. We will return to this subject shortly.

The isotropic nature of anomalous feature detections suggests an alternative hypothesis: that one or more azimuthally-continuous structures are propagating through the rings. Any given occultation will slice the structure at one point along its azimuth at one point in time. As the structure is propagating, occultations at different times will result in detections at different radial locations.

The results in table 2.5 indicate that the structure propagates about twice as rapidly as the local spiral density wave in the A ring and at approximately the same velocity as the density wave in the B ring. The heretofore-described qualities are consistent with a solitary wave, or soliton, which maintains its inherent structure while passing through background

disturbances and has a velocity of propagation set by the initial magnitude of the perturbation. Norman (1978) and Vukcevic (2014) have demonstrated the feasibility of launching a solitary wave within the spiral structure of some galaxies.

An azimuthally-continuous structure should be visible in all occultations that cross its radius, yet we noted in section 2.4 that regions that are farther from Saturn contain more observations in which an anomalous feature was not detected (see table 2.3 for a tabulation of this). This can be accounted for by the increasing number of resonances. Especially in the vicinity of the Janus 6:5 density wave, high-m resonances from the small, inner moons (i.e., Prometheus 18:17) become closely spaced. Each launches its own (weak) density wave or, at minimum, perturbs the local surface mass density. This results in increased "choppiness" in the background optical depth of the ring, making it more difficult to discern an anomalous feature.

2.5.2 Janus 4:3 region

We observe that not all clusters of anomalous feature detections lie in the included figures such that they imply a propagation velocity consistent with the results of table 2.5 (region 2 in figure 2.5, fitted in figure 2.3). We take the Janus 4:3 region as a case study. In particular are three additional morphologies of clusters distinct from those described above. Figure 2.5 depicts these regions, which are grouped by location on the plot, not distinct occultation morphology. The first is a "blob" of detections prior to the generation of the solitary wave (region 1). The second is a blob of detections prior to the Janus-in swaps of 2006 and 2014 (region 4). Third is a "halo" of detections around the main body of the solitary wave (region 3). We assert the generative mechanism for all these phenomena is the same: constructive interference between density waves. The time, place, and strength of these interactions determines into which phenomenon they manifest.

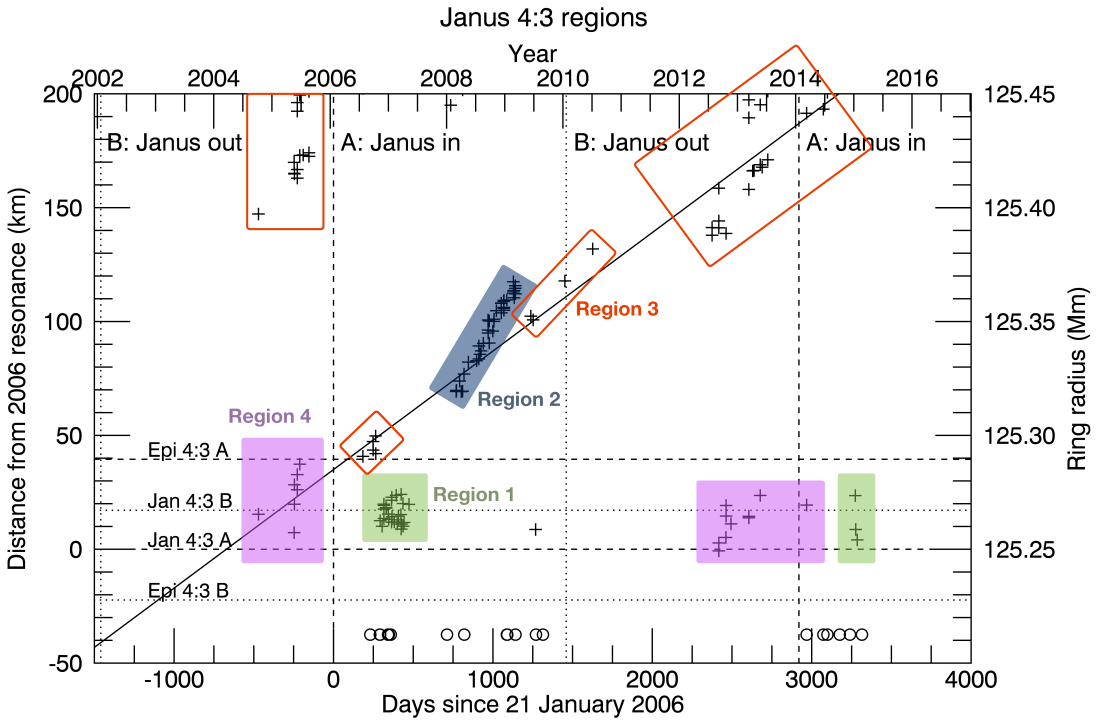

Figure 2.5: An annotated version of a panel from figure 2.3 illustrating the distinct clusters of detections observed. Regions 1 and 4 repeat to the right of the 2014 Janus-in swap. The diagonal line represents the slope with which features moving a the group velocity of the Janus 4:3 spiral density wave would propagate on the plot. See section 2.5.2 for a description of how these regions form.

2.5.2.1 Forming regions 1 and 2

When the moons swap, the resonances caused by their gravitational perturbations shift correspondingly. The ring, however, cannot respond instantaneously to this new forcing. Instead, the magnitude of the surface mass density perturbation grows with time. When the location of the new resonance falls within the wave train of an existing density wave (generated before the swap) and remains there for some time, strong nonlinear interference can take place.

As this interference builds, it generates anomalous-looking wave features that produce the blob of detections seen in region 1. When the strength of the perturbation increases past a threshold, it releases the excess negative angular momentum by generating a solitary wave (region 2).

This explains why the solitary wave is generated during the Janus-in configuration. During this time, the Janus-out-phase Epimetheus wave lies significantly interior to the now-forming Janus-in-phase Janus wave and thus takes more than a year to dissipate from the new Janus resonance location (see figure 2.5 and table 2.3 for the resonance locations). For Janus 4:3 this time scale is 1.2 years for the old Epimetheus perturbation traveling at the linear group velocity to reach the nominal new Janus resonance location and longer to pass the most perturbed region. This allows for the maximum perturbation.

2.5.2.2 Forming regions 3 and 4

During the Janus-out configuration, the Janus-in-phase Janus wave, although substantially stronger than the Janus-out-phase Epimetheus wave mentioned above, propagates out of the Janus-out-phase Janus resonance location in less than a year (0.89 yr for Janus 4:3). Thus, no solitary wave forms. Eventually, however, the newly-formed, Janus-out-phase Epimetheus wave reaches the Janus-out-phase Janus resonance and the blob of detections around day 2500 (region 4) can form from weaker nonlinear interference. For the Janus 4:3

wave, with group velocity $v_g \approx 19$ km/yr, this takes 2.1 years. The first region-4 feature after the 2010 swap occurs 2.6 years later. By 2.7 years after the 2002 Janus-out swap, a region-4 feature was also detected, but this represents the earliest available data. Although the swap occurs on 21 Jan, the moons don't immediately reach their final locations.

The final cluster, the "halo" of detections (region 3) surrounding the main solitary wave path, has actually already been described. It is the region-4 interference propagating for a number of years at a velocity comparable to the group velocity of the local spiral density wave.

2.5.2.3 Summary

In the aftermath of a Janus/Epimetheus orbital swap, the nonlinear interference between the old and new Janus and Epimetheus spiral density waves occurs at different locations and different times. Since this phenomenon is dependent solely on the arrangement of Janus and Epimetheus and the time of observation, we predict that the pattern will repeat itself following the 2014 Janus-in swap. As illustrated in figure 2.3, we have already observed repetitions of regions 1 and 4. When *Cassini* returns to an inclined orbit in 2016, further occultations should detect a new solitary wave (region 2) and new region-3 propagating interference.

2.5.3 Janus 6:5 and Janus 5:4 regions

The arguments outlined above are also consistent with the Janus 6:5 and 5:4 observations. These locations, though, do differ from Janus 4:3 in region 2. The Janus 5:4 region shows at least two parallel tracks of anomalous detentions in this area, while the Janus 6:5 region shows at least three. We consider two hypotheses for the nature of this difference.

The first notion is that after the Janus-in swap, it takes some time for the Janus-in Janus wave to propagate outwards to the Janus-in Epimetheus wave, at which point interference as described above for region 1 occurs. The timescale for this propagation is

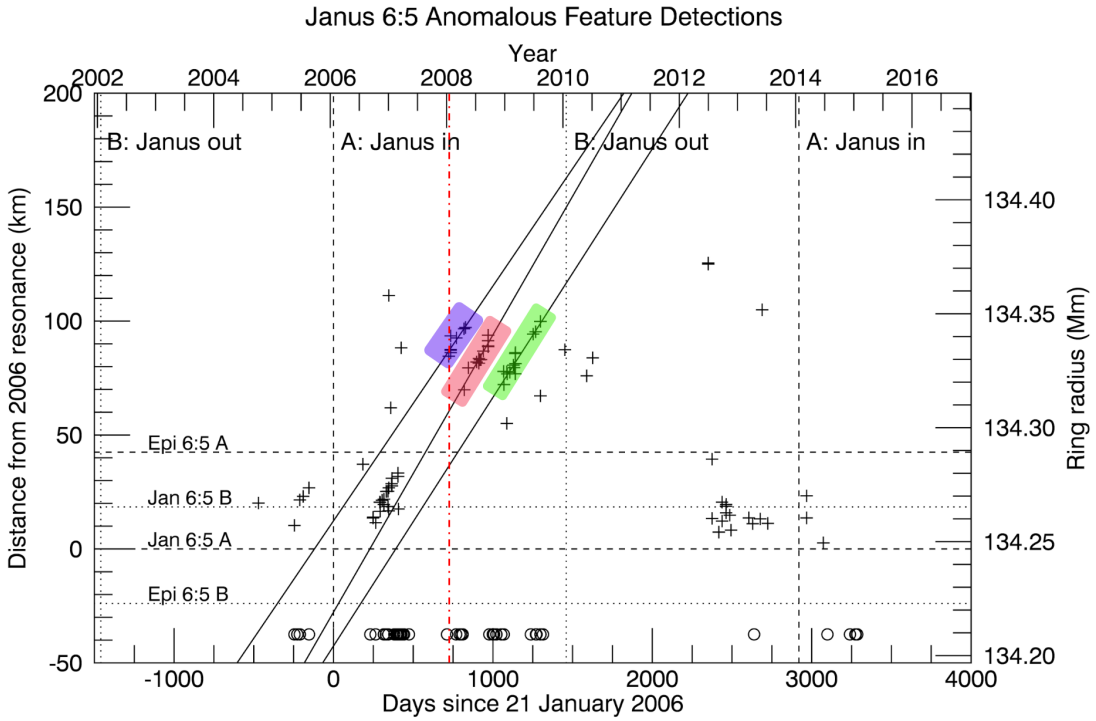

Figure 2.6: The diagonal lines represent fits to the collections of detections indicated by the colored rectangles. The solid, vertical red line indicates the earliest possible date for the Janus-in Janus wave to reach the Janus-in Epimetheus wave. Colors do not correspond to those of figure 2.5. The slopes of the lines are tabulated in table 2.6.

Resonance	Region	Velocity (km/yr)
Janus 6:5	Purple (left)	37.6±3.9
	Red (middle)	44.4±2.6
	Green (right)	39.8±1.6
Janus 5:4	Purple (left)	39.6±0.85
	Red (middle)	39.4±1.5
	Green (right)	31.9±1.5

Table 2.6: Feature velocities implied by the lines fit in figures 2.6 and 2.7. Regions correspond to those figures. Uncertainty is 1 σ with equal weighting of points. Note that the Janus 5:4 green region contains only two points.

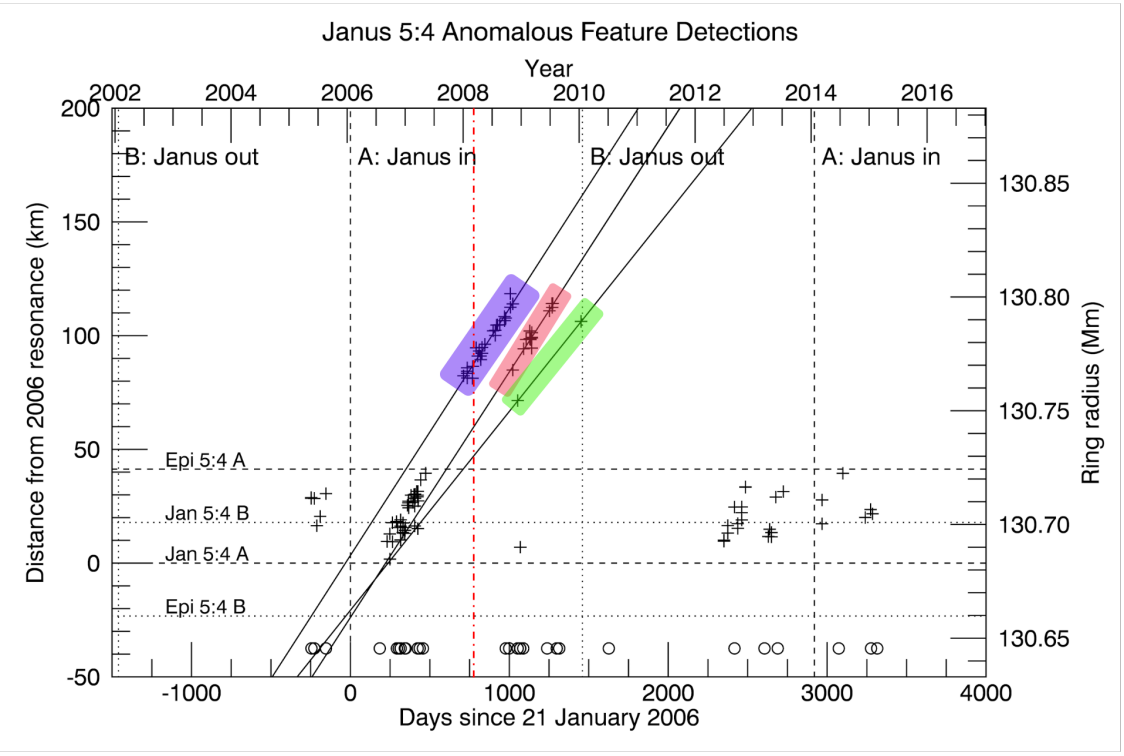

Figure 2.7: The diagonal lines represent fits to the collections of detections indicated by the colored rectangles. The solid, vertical red line indicates the earliest possible date for the Janus-in Janus wave to reach the Janus-in Epimetheus wave. Colors do not correspond to those of figure 2.5. The slopes of the lines are tabulated in table 2.6.

2.1 years for the Janus 5:4 wave and 2.0 years for the Janus 6:5 wave. Figures 2.6 and 2.7 show fits to each possible cluster of anomalous detections. This is necessary because each launched solitary wave may not have the same velocity. This hypothesis is plausible for the right-most (green) group of detections, however we must recall that the new density waves will not begin forming on exactly 21 January and thus these timescales represent a lower limit.

A second hypothesis is that a single solitary wave splits into two or more waves subsequent to being launched, a behavior of solitons that has been observed in other contexts (Hammack and Segur, 1974). This is most plausibly demonstrated by the fact that the left-most two (purple and red) fitted lines clearly bracket the initial sequence of detections in figures 2.6 and 2.7. Because these fitted lines are parallel within their uncertainties (indicating equal velocities, see table 2.6), this must have been a one-time event, not a slow diverging of two initially-launched waves.

Neither of these explanations are fully satisfying, most notably because they do not account for why a single occultation rarely observes more than one anomalous feature. Each occultation track represents a vertical line on these figures; thus, there are many instances in which, for example, a blue-feature detection is noted in an occultation but not a red or green feature.

2.5.4 Janus 2:1 region

Unlike the other resonances examined in this work, the Janus 2:1 lies in the B ring. Physical conditions in this region may be different from those in areas of the A ring and we correspondingly observe a different manifestation of the feature. Nevertheless, we believe the generative mechanism in the Janus 2:1 region is broadly the same as described above. Instead of traveling at approximately twice the group velocity of the local spiral density wave, the feature in this region propagates at a commensurate speed. Because this velocity is much slower (see table 2.5), the solitary wave should not propagate out of the examined

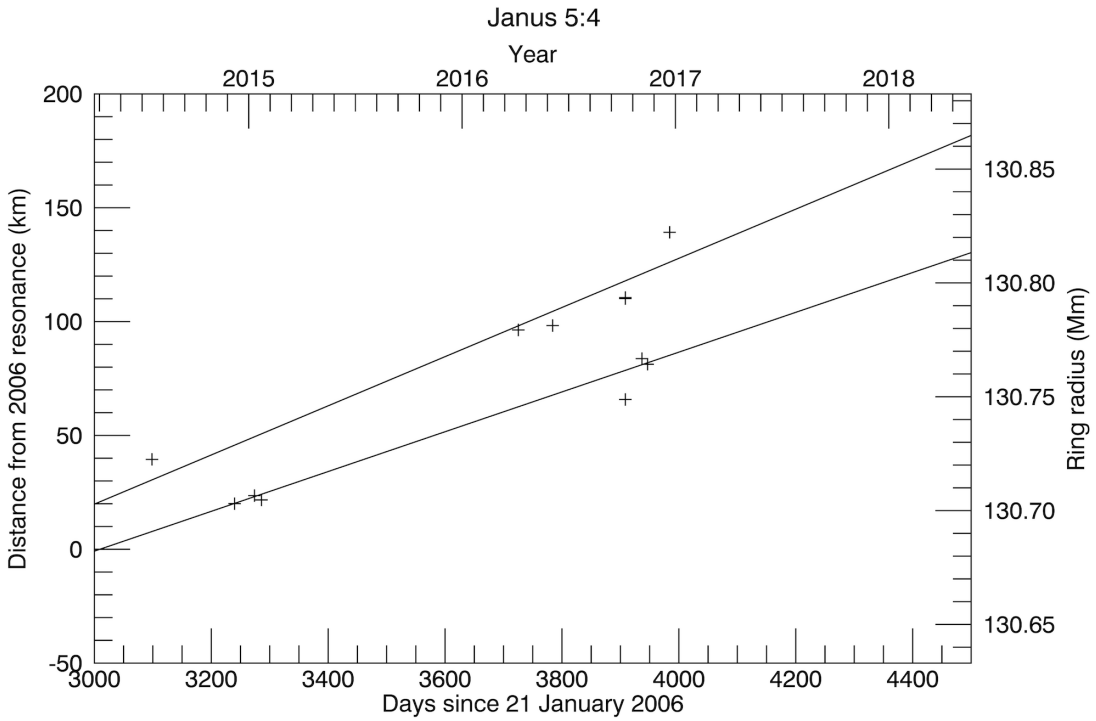

Figure 2.8: The available data for the Janus 5:4 region in the aftermath of the 2014 orbital swap. The top line has the same slope as the red (middle) line in table 2.6, while the bottom line has the velocity implied by the green (right) line in that table. Each are placed suggestively to illustrate the potential observation of another splitting solitary wave.

region within four years. Indeed, we see "copies" of the wave that are visible more than 100 km from the resonance in figure 2.3. That multiple copies persist is consistent with Horn et al. (1996), who observed a similar phenomenon for wakes generated by the moon Pan. However, the velocity necessary to achieve the observed separation in four years is not consistent with implied velocities of either the upper or lower sequences observed during the 2006-2010 period. The velocity required, 32 km/yr, is substantially larger than that implied by fits to any sequence of detections in the Janus 2:1 region. The fact that the computed feature velocity is bracketed by the density wave group velocities estimated for two different surface mass densities might lend support to the variable surface mass density hypothesis of Hedman and Nicholson (2016).

2.5.5 Reappearance after 2014 swap

When the orbital configuration seen in 2006 returned in 2014, the process of generating a solitary wave should have begun once again and our observations support this. Unfortunately, the number of observations during this epoch is substantially lower than in the post-2006 period and the quality of each observation is also typically worse than earlier in the mission. This results in relatively few opportunities to identify the feature, but it is clearly detected at all four resonance locations.

In the Janus 2:1 region, the 2006 wave can still be seen propagating as before, indicating that we can track an instance of the solitary wave for nearly ten years. The data is insufficient to identify conclusively the same split-wave behavior previously observed in the Janus 5:4 and Janus 6:5 regions, but what is available certainly hints in that direction. Figure 2.8 shows the relationship between the post-2014 data and the fits computed from the post-2006 observations for the Janus 5:4 region. Unfortunately, the new data do not fill in the critical period where the possible splitting actually occurs. High-resolution observations of that phenomenon will have to wait for a future mission.

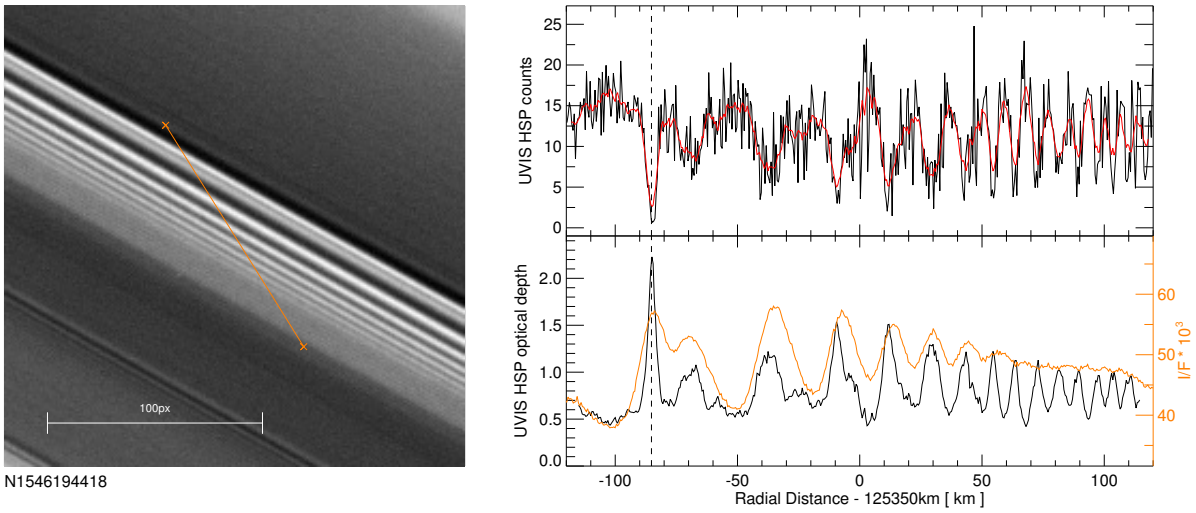

Figure 2.9: An ISS narrow-angle camera observation of the Janus 4:3 spiral density wave taken simultaneously with a UVIS HSP occultation. *Left*: The UVIS occultation track overlaid on the image. This image has a resolution of approximately 4 km/px and was taken approximately one minute prior to the occultation track passing through the anomalous feature. *Top right*: The HSP occultation sampled to 500 m (black line) and 4 km (red line). The dashed line passes through the peak of the anomalous feature. *Bottom right*: The I/F measured in a 3-px-wide profile along the UVIS track in the NAC image (orange line) and the HSP counts sampled to 4 km (black line).

2.5.6 Observations with the Imaging Science Subsystem

Continuous features like the ones described above should be easier to detect in ISS imagery than a large population of discrete objects. We undertook a successful search of archival imaging data for possible detections of either the solitary wave or the interference patterns in the spiral density wave in images captured simultaneously with occultations. Figure 2.9 illustrates a feature detection within a high-resolution targeted *Cassini* narrow-angle camera (NAC) image of the Janus 4:3 region, one of four such images found. A similar image was found for each of the Janus 2:1, Janus 5:4, and Janus 6:5 regions.

The radial locations of these features fall along the predicted path of the solitary wave, providing a confirmation of this phenomenon independent of HSP stellar occultations. Moreover, each image shows that the feature extends at least as wide as the NAC field of view, a distance of 5446 km for the image in figure 2.9. This is compelling evidence in favor of a single continuous wave rather than a collection of discrete objects.

2.6 Conclusion

It is clear that the orbital swap of Janus and Epimetheus has a substantial effect on the rings. Tiscareno et al. (2006b) have demonstrated that it accounts for the unusual morphology of second-order, linear spiral density waves and El Moutamid et al. (2016) have shown it substantially alters the shape of the outer edge of the A ring. Our investigation reveals that in Saturn's strongest density waves, the effect is even more dramatic. Nonlinear interference between the waves generated at the pre- and post-swap resonance locations results in the formation of a solitary wave. In the A ring, this wave propagates outward at about twice the group velocity of the local spiral density waves and in the B ring the propagation velocity is commensurate to the density wave group velocity.

Occultations observed by *Cassini* throughout 2016 and images captured until the end of the mission should reveal the next iteration of this cycle and provide a longer baseline

over which to understand the phenomenon. A future model describing the behavior of the solitary wave may also allow for an independent estimation of the ring surface mass density.

Finally, these observations have potential applications in understanding the physics of protoplanetary and accretion disks, where the migration of massive bodies has been theorized. Although we may generally lack the capability of detecting these moving bodies, the effects they render onto the neighboring disk of particles and gas may reveal their motion indirectly.

Chapter 3

Structures in the F ring

3.1 Introduction

The F ring of Saturn is one of the Solar System's most dynamic locations. Lying near the planet's Roche limit several thousand kilometers outside the main rings, the F ring (a = 140221.3) experiences a balance between Saturn's tidal forces and particle self-gravity. Nearby shepherd moons Prometheus and Pandora provide additional gravitational perturbations to the ring. Observations dating back to *Voyager* provide direct and indirect evidence for a population of kilometer-sized moonlets orbiting in this region.

With unparalleled spatial resolution, the Ultraviolet Imaging Spectrograph (UVIS) on *Cassini* has provided some of the most detailed-yet observations of density features within the F ring. These structures (termed "kittens") have been interpreted as direct detections of members of the local moonlet population (Esposito et al., 2008, 2012; Meinke et al., 2012). This chapter extends the search for these features to data collected since 2012 and critically reexamines their physical interpretation. It has been submitted for publication to Icarus.

3.1.1 F ring

Saturn's F ring differs substantially from the inner main rings. Albers et al. (2012) found detectable eccentricity (2.35×10^{-3}) and inclination (6.43×10^{-3}), while Scharringhausen and Nicholson (2013) measured its vertical height to be 13±7 km, orders of magnitude larger than the interior rings. The "core" is generally the most optically-thick component

($\tau \sim 0.3$) and has a variable width on the order of 10 km. One or more "strands" often accompanies the core at a distance of tens of kilometers.

3.1.2 Direct evidence for moonlets

Meinke et al. (2012) found 27 statistically-significant features in 101 stellar occultations by the F ring observed with UVIS. Seventeen of these features were determined to be consistent with semi-permanent aggregations ranging in radial width from 46 m to 2.16 km. Two of the 17 were classified as dense moonlets and one non-moonlet was simultaneously co-observed by the Visual and Infrared Mapping Spectrometer (VIMS).

Porco et al. (2005) reported the discovery of three small objects orbiting near the F ring in images captured by the *Cassini* Imaging Science Subsystem (ISS): S/2004 S3, S/2004 S4, and S/2004 S6. Subsequent observations of additional features demonstrate that some objects may persist between imaging sequences while others disappear (Spitale et al., 2006).

Showalter (2004) analyzed images from the *Voyager* spacecraft and tracked 34 "clumps" over as many as seven weeks. No feature survived the nine months between the two Saturn encounters and some showed evidence of evolution during the observation period. *Hubble* observations of the 1995 ring-plane crossing also detected a series of clumps generally consistent with F-ring orbits (Bosh and Rivkin, 1996; McGhee et al., 2001). The features in these studies have azimuthal extents of more than a degree, with one degree at the F-ring's orbit subtending approximately 2500 km. Thus, these older observations seem unlikely to represent the same phenomena denoted as clump-like in *Cassini* data, which are on the order of kilometers in size. More likely, they represent unresolved detections of the moonlet-induced features described below.

3.1.3 Indirect evidence for moonlets

An unseen population of moonlets embedded in the F ring was first theorized by Cuzzi and Burns (1988) as an explanation for the depletion of electrons in *Pioneer 11* observations.

The bulk of indirect evidence for such objects, however, comes from images made by the *Cassini* ISS. These images reveal the highly-variable structure of the F ring. Much of this variation can be attributed to regular close approaches from Prometheus, however some smaller-scale features cannot (Murray et al., 2005). Instead, these temporary structures seem better described by interactions between ring material and moonlets. This interaction could take the form of a physical collision between moonlet and the F-ring core (Attree et al., 2012) or a gravitational perturbation (Murray et al., 2008).

3.2 Data

We examined 176 stellar occultations by the F ring observed with the UVIS High Speed Photometer (HSP) between 19 May 2005 and 18 Dec 2016. In some observations, the point at which the line of sight from spacecraft to star pierces the rings moved both radially inwards and outwards. We term the inward motion the ingress, the outward motion the egress, and count these as separate occultations. In this work the ingress is denoted by 'in' and the egress by 'out' in occultation names.

HSP, a separate optical train in UVIS, is described by Esposito et al. (2004). The instrument makes photometric observations of bright O- and B-type stars through its 110-190 nm bandpass at intervals as short as 1 ms. For the observations used in this work, the cadence varied between 1 and 8 ms, remaining constant for the duration of an observation. Occultations with a longer cadence typically have lower spatial resolution, although the features described here are usually much larger than an observation's resolution.

Each sampling period Δt, HSP measures a number of photons $I\Delta t$ for the observed flux given by $I = I_0 e^{-\tau} + b$. The target star's unocculted flux I_0 is attenuated by the ring's optical depth τ and increased by the background flux b. Ignoring stellar variability, I_0 should be constant, however the HSP becomes more sensitive over the course of an observation, a phenomenon known as "ramping up" (Colwell et al., 2007). This effect is more pronounced in later observations, but because we are not attempting to make absolute photometric

measurements here, it is not a substantial concern.

For observations through *Cassini* rev 212, computations of I_0 and b were provided by N. Albers (personal communication). For subsequent occultations, we compute I_0 as the mean stellar signal in the empty regions surrounding the F ring and approximate b as 0.5 counts, the median value for all observations through rev 212. More than 90% of those observations have computed background counts of less than 2 per integration period, making this a reasonable approximation.

We convert raw HSP photon counts and observation times to positions within the rings using the method described in Albers et al. (2012)[1] . This uses NAIF SPICE kernels to account for the position and orientation of the planet and spacecraft. The main rings are assumed to lie in Saturn's equatorial plane, with longitude measured prograde from from the ascending node of the planet's equatorial plane on Earth's J2000 equator. The F ring is modeled as a precessing, inclined ellipse defined by the best-fit parameters from Albers et al. (2012).

Unless otherwise noted, "optical depth" refers to the normal optical depth

$$\tau_\perp = \tau \sin B = \ln \left[\frac{I_0}{I - b} \right] \sin B, \tag{3.1}$$

where B gives the angle between the line of sight and the ring plane. B remains approximately constant for the duration of an observation.

3.3 Methods

3.3.1 Searching for clumps

We employ an m-test to search for statistically-significant features in the data, a measure used in previous F-ring occultation studies (Esposito et al., 2008; Meinke et al., 2012). This method assumes that over spatial regions on the order of kilometers, observed photon counts are well-described by a Poisson distribution. A probability for each data point to be

[1] Geometry code provided by M. Sremčević.

observed by chance is computed assuming a Poisson distribution with mean λ equal to the average value of 5 km of surrounding data points. This probability is then multiplied by the total number of data points in an observation to compute the number of expected data points as likely or less likely to be observed than the given point. For a data point with k counts,

$$m = N \sum_{j=0}^{k} \frac{e^{-\lambda} \lambda^j}{j!}, \tag{3.2}$$

for an observation of length N and a local, 5-km mean counts of λ.

We adopt a more uniformly-conservative criterion than Meinke et al. (2012) or Esposito et al. (2008) by requiring a point to have $m < 0.1$ to be considered anomalous; this means we would expect to find such a point by chance only once in ten observations of length N. For an anomalous point to be considered part of a kitten, we also adopt the requirement of $\tau_\perp \geq 0.4$, the same as previous work. This value was chosen based on a feature observed simultaneously by UVIS and VIMS.

Larger features consist of a series of significant points that are adjacent to one another. Each observation is binned at six resolutions (25 m, 100 m, 250 m, 500 m, 1 km, and 2 km) and an m-test search is performed at each level. This preserves our ability to detect the smallest features while also enabling the detection of larger, more irregular structures which may contain a few points that aren't significant on smaller scales. To further reduce the likelihood of a false positive detection, we require a feature to be observed as significant in at least two bin sizes to be selected. Most features are observed in at least four bin sizes.

Feature radii and longitude are measured in F-ring geometry from the point of greatest observed optical depth, which may not align with the center of an object. An object's radial width dr is measured as the full width at half-max.

3.3.2 A simple accretion model

It has been postulated that clumps in the F-ring could grow through binary, collisional accretion (Canup and Esposito, 1995; Barbara and Esposito, 2002; Esposito et al., 2008, 2012). Meinke (2012) explored this possibility using the Smoluchowski coagulation-fragmentation equation with a specific focus on generating a size-frequency distribution that matched observed kittens. We implement a similar model with the purpose of examining how different ring conditions affect aggregation.

A simple model such as this represents an extremely optimistic case for how rapidly structures could assemble. In it, collisions between particles accrete or fragment solely based on their relative size. We assume tidal effects from Saturn do not alter the likelihood of agglomeration; neither do particles' relative velocity or chemical composition. If appropriately-sized structures cannot form under these circumstances, it is unlikely they would form more successfully in a more-complete model.

Suppose a given volume V contains N_0 indivisible particles of individual mass M_0. If these particles collide with one another, they can combine to form larger aggregations. If these larger aggregates collide, they can further coalesce or fragment into smaller structures. At some time $t > 0$, this system will have evolved a distribution of aggregate sizes $n(m, t)$, which we can model using the coagulation-fragmentation equation (Wattis, 2006):

$$\frac{dn(m,t)}{dt} = G_{\text{acc}} + G_{\text{frag}} - L_{\text{acc}} - L_{\text{frag}}. \tag{3.3}$$

Here, G_{acc} and G_{frag} are the gain in particles of mass m as a result of accretion and fragmentation, respectively. L_{acc} and L_{frag} are the loss of such particles as a result of the same processes.

Consider the i-th mass bin. The number of aggregates it contains increases each time smaller objects of m_j and m_k combine, such that $j + k = i$. We can write this as

$$G_{\text{acc}}(m_i, t) = \frac{1}{2} \sum_{j=1}^{i-1} K(m_{i-j}, m_j) P_{\text{acc}}(m_{i-j}, m_j) n(m_{i-j}, t) n(m_j, t), \tag{3.4}$$

where $K(m_a, m_b)$ is the likelihood of a collision occurring and $P_{\rm acc}(m_a, m_b)$ is the likelihood that such a collision results in accretion as opposed to fragmentation. We divide by two to avoid double-counting collisions.

The number of aggregates of mass m_i can also increase if a collision between two objects results in the formation of a fragment of that mass. In addition to considering the probability that a collision occurs and the probability that such a collision results in fragmentation, we must also consider what fraction of the resulting fragments fall within bin i. Thus, we have

$$G_{\rm frag}(m_i, t) = \sum_{j=1}^{j_{\rm max}} \sum_{\rm k=1}^{j} K(m_j, m_k)(1 - P_{\rm acc}(m_j, m_k))F(m_i, m_j, m_k)n(m_j, t)n(m_k, t), \quad (3.5)$$

where the additional factor $F(m_i, m_a, m_b)$ gives the fraction of the total mass $m_a + m_b$ that is fragmented into bin m_i and $j_{\rm max}$ represents the largest mass bin with $n > 0$.

Since every collision results in either accretion or fragmentation, we must remove that mass from the bin (of course, it is possible that any resulting fragmentation may replace some of that material). This gives us

$$L_{\rm acc}(m_i, t) + L_{\rm frag}(m_i, t) = n(m_i, t) \sum_{j=0}^{j_{\rm max}} K(m_i, m_j)n(m_j, t). \quad (3.6)$$

The functional forms of F, K, and $P_{\rm acc}$, as well as the values of M_0 and N_0 define the physics of our specific problem. Let us first consider K, the likelihood that a given collision occurs. Ignoring gravitational focusing (which is weak at the sizes of interest), we can estimate

$$K(m_a, m_b) = \frac{(\sigma_a + \sigma_b)v}{V} = \frac{(\pi r_a^2 + \pi r_b^2)v}{V}, \quad (3.7)$$

for cross-sectional areas σ_a and σ_b and relative velocity v. We can relate σ to m through the density ρ:

$$\rho = \frac{m_a}{V_a} = \frac{3m_a}{4\pi r_a^3} \rightarrow r_a = \left[\frac{3m_a}{4\pi\rho}\right]^{1/3}, \quad (3.8)$$

which allows us to rewrite K as

$$K(m_a, m_b) = k\left(m_a^{2/3} + m_b^{2/3}\right) = \left(\frac{\pi v}{V}\right)\left(\frac{3}{4\pi\rho}\right)^{2/3}\left(m_a^{2/3} + m_b^{2/3}\right). \quad (3.9)$$

The probability that accretion occurs $P_{\rm acc}$ is a function of the relative sizes of the colliding aggregates. Objects of similar size are more likely to fragment upon collision, while a small object will nearly always accrete onto a larger one. For $m_a \geq m_b$, we define this as

$$P_{\rm acc}(m_a, m_b) = \begin{cases} 1 - \frac{m_b}{m_a} & m_a \neq M_0 \\ 1 & m_a = m_b = M_0 \end{cases} \tag{3.10}$$

When $m_a = m_b$, the aggregates always fragment, unless both are of the fundamental size M_0, which we take to be indivisible. Accretion dominates for $m_a >> m_b$.

When fragmentation does occur, it produces a distribution of resulting objects which are power-law distributed. We adopt a power-law index of 11/6, typical of collisional fragmentation (Tanaka et al., 1996). We additionally confine the size of the largest fragment to be half the combined mass of the colliding aggregates. Thus for mass bin $m_i \leq (m_a + m_b)/2$, we write

$$F(m_i, m_a, m_b) = \frac{m_i^{-11/6}}{\sum_{j=1}^{(a+b)/2} m_j^{-11/6}} \tag{3.11}$$

as the fraction of mass fragmented into the bin.

For increased efficiency, we use logarithmic mass bins of the form $2^{i/2}$ kg and a dynamic time step. The time step is adjusted so that it varies by no more than 0.8% from the previous period, with a minimum step of one second and a maximum of 10^5 s. To demonstrate the validity of this code, we reproduce figure 1a from Silk and Takahashi (1979), who derived and plotted analytic solutions to simple kernels.

3.4 Results

3.4.1 Number and distribution of features

In 176 examined stellar occultations, we find 54 "kitten"-like features. Meinke et al. (2012) defined five categories of features: moonlet, multi-icicle, icicle, V core, W core; we define only two: moonlet and clump. We discard the W core features as detections of

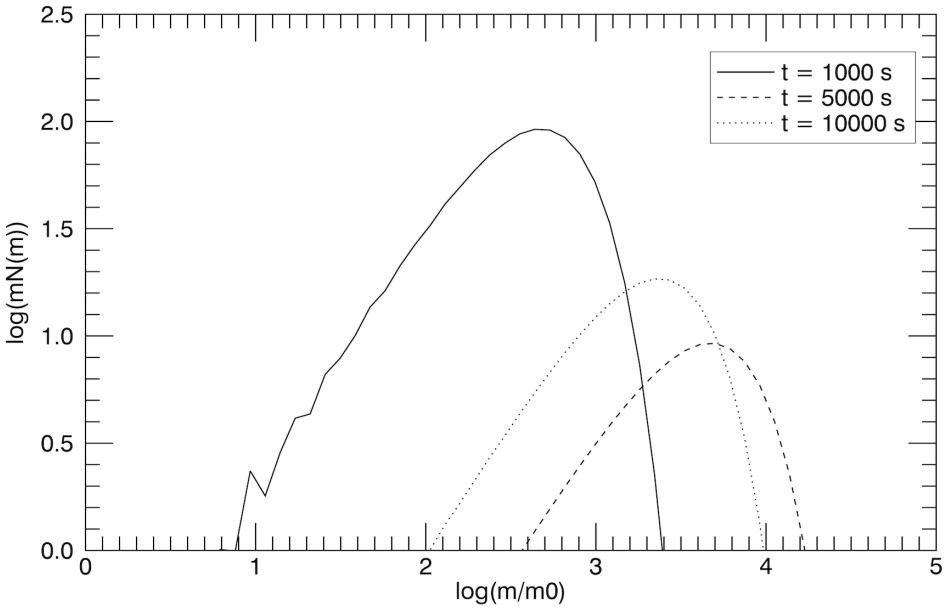

Figure 3.1: The evolution of an initial mass function $10^5\delta(m - m_0)$ for $m_0 = 1$ kg and $K = 10^{-5}$, a constant. This reproduces figure 1a from Silk and Takahashi (1979). The jitter in the $t = 1000$ case arises from the smallest logarithmic bins, which can be smaller in width than the preceding bin is in magnitude.

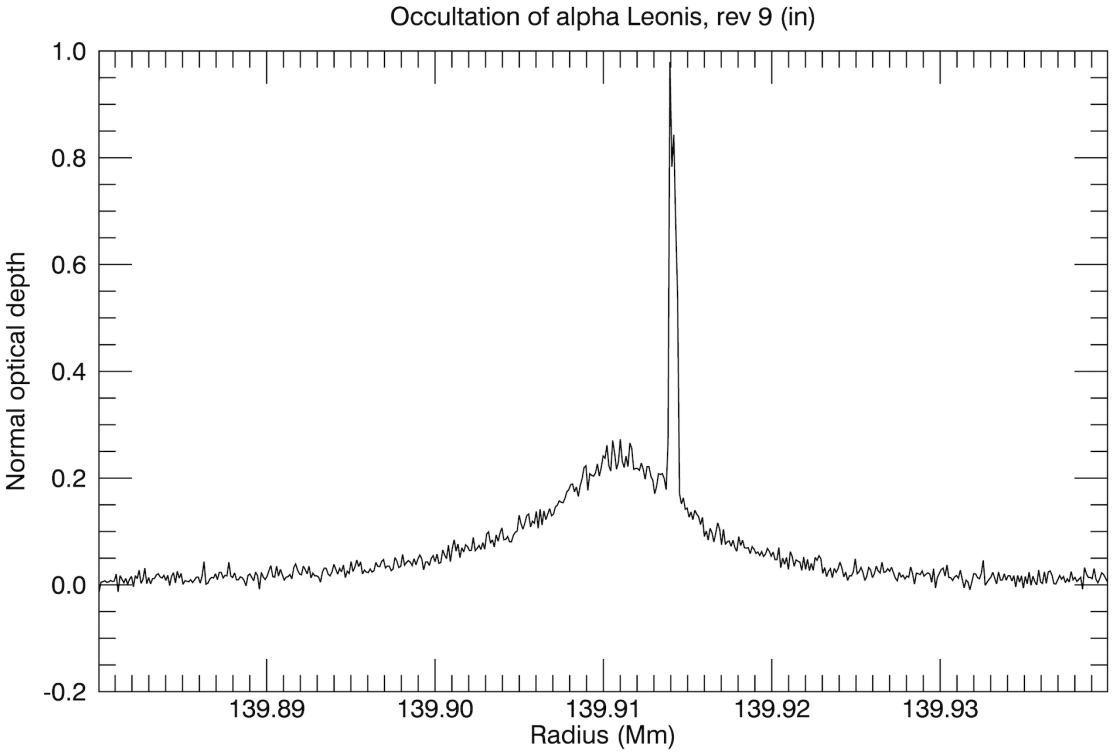

Figure 3.2: A moonlet in α Leonis, rev 9 (in). The data are binned to a radial resolution of approximately 100 m and the entire region is 60 km in width. Notice the flat sides of the occultation profile, which define a feature as a moonlet. A closer-in view is available in figure 3.3.

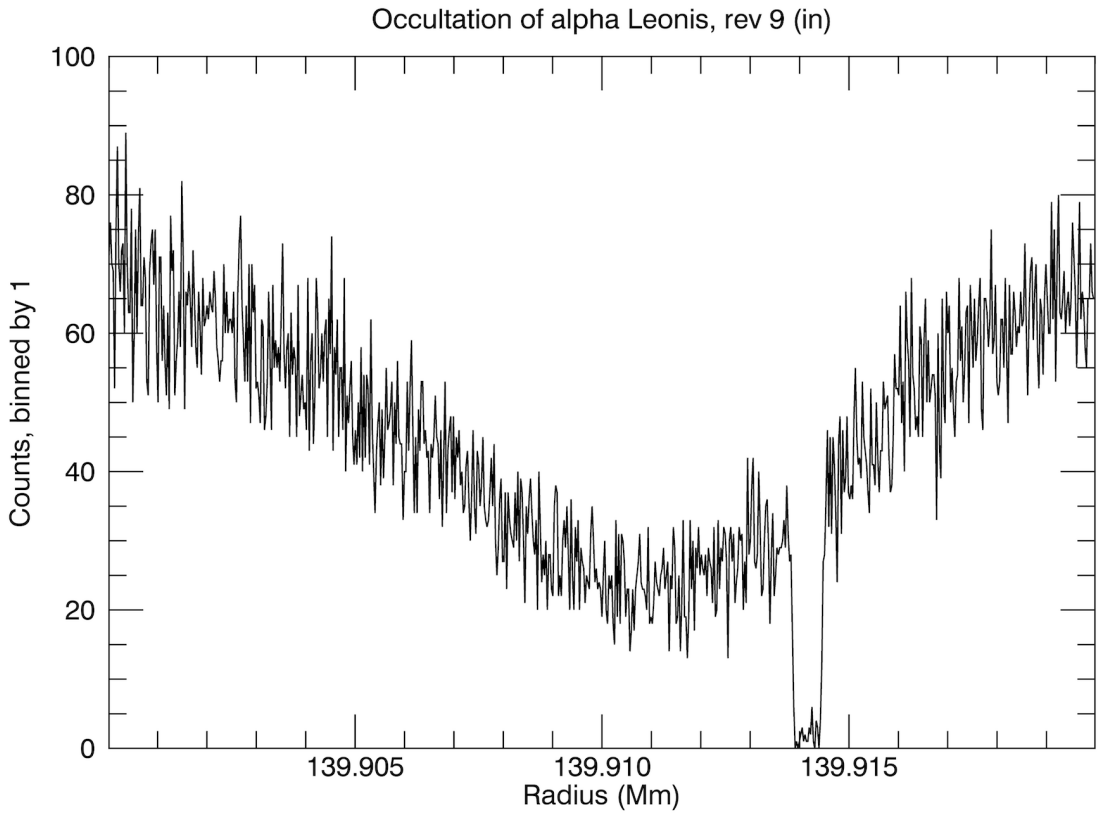

Figure 3.3: A moonlet in α Leonis, rev 9 (in). The data are unbinned with a radial resolution of 28 m and the entire region is 20 km in width. Notice the flat sides and bottom of the occultation profile, which define a feature as a moonlet.

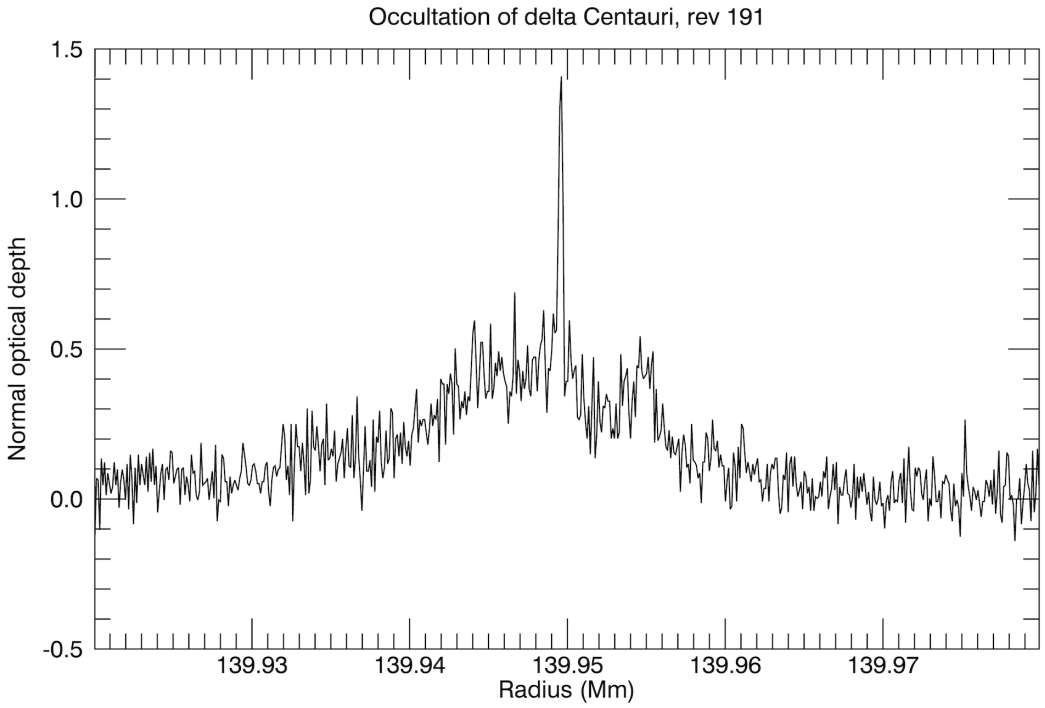

Figure 3.4: A clump in δ Centauri, rev 191. The data are binned to a radial resolution of approximately 100 m and the entire region is 60 km in width. A closer-in view is available in figure 3.5.

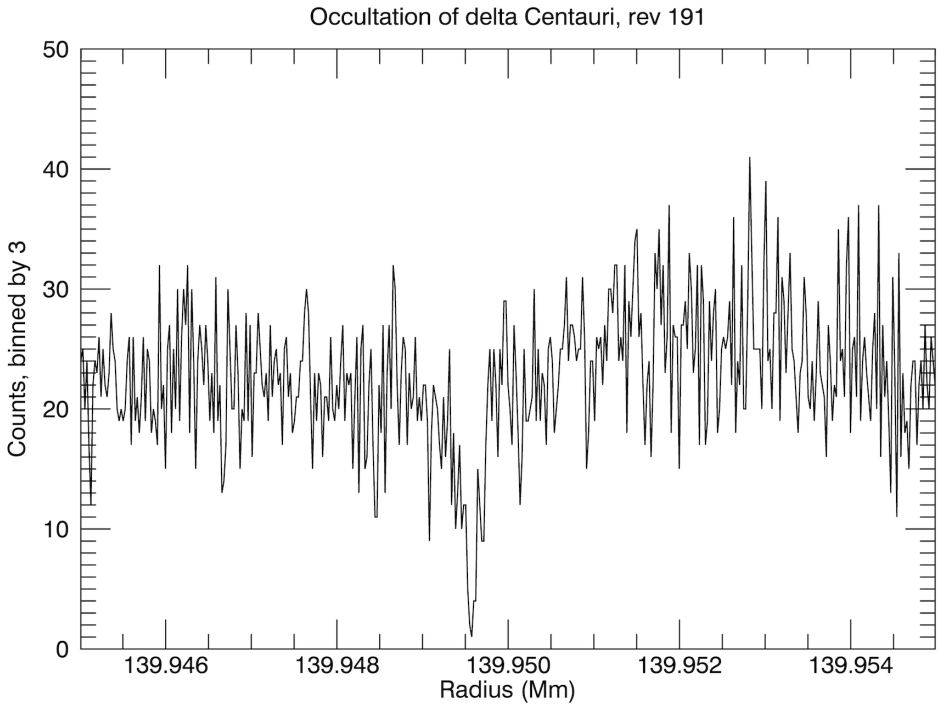

Figure 3.5: A clump in δ Centauri, rev 191. The data are binned to a radial resolution of approximately 24 m and the entire region is 9 km in width.

the F-ring core and a strand, and collapse the other non-moonlet categories into "clump," where V cores are assumed to be features that lie directly at the center of a core or strand. Moonlets are distinguished from the more-generic clump by the steep, nearly-vertical sides and flat bottom of their occultation profile. By this metric, we report 2 moonlets and 52 clumps, compared to their 2 and 17, respectively. These numbers cannot be compared as detection rates because the way in which features were classified differed between studies. Table 3.1 lists the detected features, while figures 3.2 and 3.3 show an example of a moonlet and figures 3.4 and 3.5 show an example of a clump. Figure 3.6 plots the cumulative size-frequency distribution for both the features reported in the previous work and those detected here.

The features reported here represent a conservative counting of those in the available data. A visual inspection of all occultations reveals a number of features which appear significant to the eye but are not selected by the algorithm. A common reason for this is a peak optical depth less than 0.4, but given the high variability of the F ring, this is an uneven criterion. Remaining conservative in the search allows us high confidence in the non-spurious nature of the reported objects.

Figure 3.6 shows that, for features of intermediate size, the size-frequency distribution for clumps found in this work is consistent with those from Meinke et al. (2012). Both small ($dr < 100$ m) and large ($dr > 600$ m) are depleted relative to the intermediate-sized structures. Narrower features are likely undercounted because they are similar in size to the smaller bin sizes. Suppose a clump has a true dr of 75 m. It may be detected in the 25-m binning but it could likely be split across multiple elements in the 100-m binning. Even if it falls entirely within a single 100-m bin, when averaged with other counts in that bin, it may lose its local significance. Their smaller population also means that our 176 observations are less likely to sample a statistically-significant number of them.

Conflicts with the binning aren't likely to account for a depletion of larger objects. Instead, the paucity of these features probably represents a smaller population in the rings.

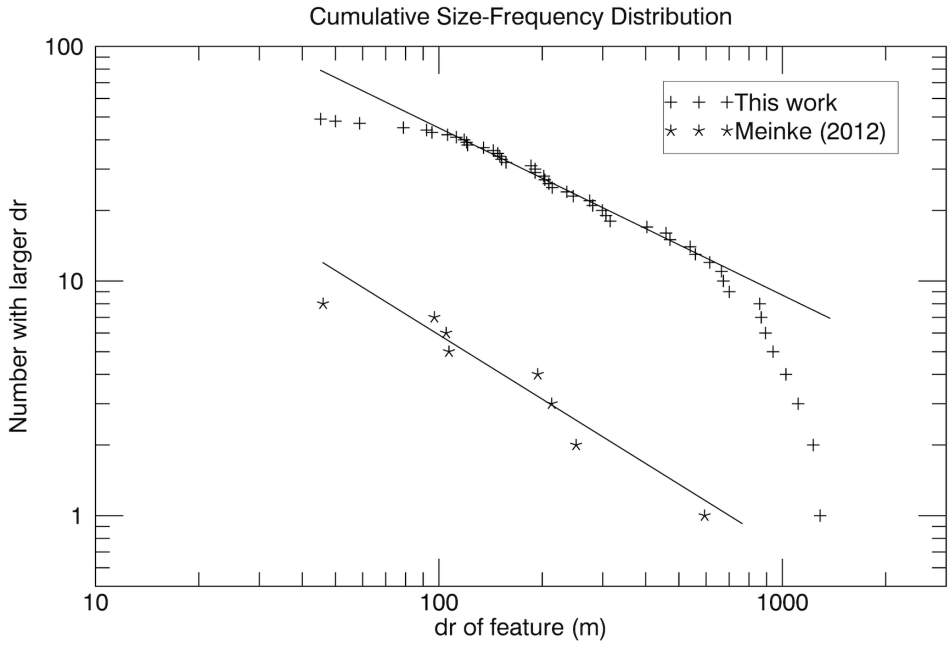

Figure 3.6: A comparison of the cumulative size-frequency distribution for features identified in this work and Meinke et al. (2012). Data points for this work are all detections classified as "clump" or "moonlet" and data points from the previous work were classified as "simple icicle" and "moonlet." Fitted lines are power laws of the form $y = ax^{-b}$, with $b = 0.71 \pm 0.02$ for the upper line and $b = 0.91 \pm 0.28$ for the lower line. Fits were performed only for features in the radial size range 100 m $< dr <$ 600 m.

These larger structures are more likely to be disrupted by Saturn's tidal forces or to engage in a destructive collision with another feature. That the two populations likely have different reasons for a reduced number of detections is supported by their different slopes relative to the fitted line.

Figure 3.7 plots the number density of clumps as a function of their relative longitude to the shepherding satellites Prometheus (interior) and Pandora (exterior). Because the distribution of total observations is not uniform relative to the positions of the moons, the values are expressed as fractions of the observations made in those relative longitude bins. In both instances, we find the greatest number of features at relative longitudes opposite each moon.

Table 3.1: Summary of detected features in the F ring. The number of features marked as included in Meinke et al. (2012) does not match their value because our method splits some structures into more than one feature and combines others. Radii are not an exact match because of differences in both the geometric model of the F ring used and the method of performing geometric computations. The column "In M12" refers to whether a feature was reported by Meinke et al. (2012).

Occultation	Radius (km)	Longitude (deg)	dr (km)	In M12
Moonlets				
α Leonis, rev 9 (in)	139914.17	350.52	0.558	Yes
α Arae, rev 90 (in)	139931.25	139.06	0.106	Yes
Clumps				

Occultation	Radius (km)	Longitude (deg)	dr (km)	In M12
126 τ, rev 8	140064.41	227.209	0.150	Yes
ζ Ophirchi, rev 26	139896.73	0.05	0.246	
α Scorpii, rev 29	139917.47	201.68	2.920	Yes
ϵ Lupi, rev 37 (out)	140014.21	91.79	0.135	
γ Arae, rev 37 (in)	140288.29	248.43	1.025	Yes
	140284.22	248.43	0.665	Yes
	140277.93	48.43	0.152	Yes
SAO 205389, rev 57	140400.49	186.87	0.673	Yes
δ Lupi, rev 57	140440.02	200.68	0.092	
α Arae, rev 63	140501.56	26.11	0.214	Yes
	140502.69	26.11	0.307	Yes
	140503.12	26.11	0.157	Yes
	140503.86	26.11	0.121	Yes
	140504.64	26.11	0.045	Yes
β Centauri, rev 64	140153.90	344.98	0.471	
β Centauri, rev 75	139945.63	173.03	0.893	Yes
	139944.74	173.03	0.079	Yes
	139944.47	173.03	0.079	Yes
β Centauri, rev 77 (in)	139904.77	172.97	0.939	
β Centauri, rev 78	140557.34	23.94	3.104	
α Arae, rev 79 (in)	140145.41	138.31	0.941	Yes
	140142.05	138.31	0.501	Yes
β Centauri, rev 81	140205.16	168.47	0.148	Yes
β Centauri, rev 89	140333.60	167.79	0.299	Yes
α Arae, rev 90 (out)	139959.63	37.36	0.119	Yes
α Arae, rev 96 (out)	140504.53	50.65	1.230	Yes

Occultation	Radius (km)	Longitude (deg)	dr (km)	In M12
δ Centauri, rev 98	140000.60	193.97	0.236	
α Arae, rev 98 (in)	140321.23	134.52	0.203	Yes
α Arae, rev 98 (out)	140526.25	57.38	1.374	Yes
ϵ Cassiopeiae, rev 104 (out)	140181.42	137.34	0.315	Yes
	140189.08	137.34	0.701	
β Centauri, rev 105 (out)	140229.90	345.01	0.615	
σ Sagittarii, rev 114	140319.23	186.86	1.289	
α Virginis, rev 134	140557.73	136.70	0.868	Yes
κ Canis Majoris, rev 168 (out)	140249.24	201.15	0.539	
ζ Canis Majoris, rev 169 (in)	139924.29	147.61	0.120	
ζ Puppis, rev 171 (in)	140505.2	132.07	1.112	
	140500.29	132.07	0.191	
ζ Puppis, rev 171 (out)	139987.18	238.20	3.268	
	139999.44	238.20	3.701	
γ Pegasi, rev 172 (out)	140502.00	151.15	0.050	
	140525.75	151.13	0.280	
ϵ Canis Majoris, rev 173 (in)	139921.22	74.41	0.185	
	139914.89	74.41	0.209	
ϵ Canis Majoris, rev 174 (in)	139957.87	74.36	0.112	
α Lyrae, rev 175	140481.56	273.38	0.275	
θ Carinae, rev 186	140000.66	118.096	0.459	
	139996.11	118.10	0.404	
δ Centauri, rev 191	139949.60	270.60	0.202	
α Virginis, rev 210	140389.90	114.00	0.095	
β Canis Majoris, rev 211	139916.64	99.60	0.860	
α Virginis, rev 232	140303.86	339.34	0.144	

Occultation	Radius (km)	Longitude (deg)	dr (km)	In M12
α Lupi, rev 248	140370.18	336.99	0.059	
α Pavonis, rev 254	140028.83	249.58	0.191	

3.4.2 Mass of features

We can estimate the mass of a given clump by making assumptions about its shape and density. A dominant factor in the shape of an aggregate is azimuthal lengthening due to differential rotation. This has been observed both numerically through N-body simulations of self-gravity wakes (e.g., Salo et al. (2004)) and directly in the A ring in the form of propellors (Tiscareno et al., 2006a, 2008). Sremčević et al. (2007) directly measured the azimuthal elongation of propellor features to be approximately 8.5 times their radial width, a value we will adopt here. Treating a clump as a triaxial ellipsoid with radial and vertical size dr and azimuthal size $8.5dr$, we find a mass of

$$m_{dr} = \frac{8.5\pi}{6}\rho dr^3, \tag{3.12}$$

for for a bulk density ρ. Meinke et al. (2012) adopt a value of 235 kg/m^3 for ρ, corresponding to half the density of Prometheus, while Barbara and Esposito (2002) adopt a value of 1000 kg/m^3.

Of course, more azimuthally-elongated structures are also more likely to be "cut" by an arbitrary occultation path across the F ring. We can estimate the total population of objects in the ring of a given radial size as

$$N_{dr} = \frac{n_{\rm obs}}{n_{\rm occ}}\frac{2\pi a}{8.5dr}, \tag{3.13}$$

where $n_{\rm obs}$ is the number of features detected with radial width dr, $n_{\rm occ} = 176$, and a is the semi-major axis of the F ring. By placing detected objects into a series of dr bins, we can

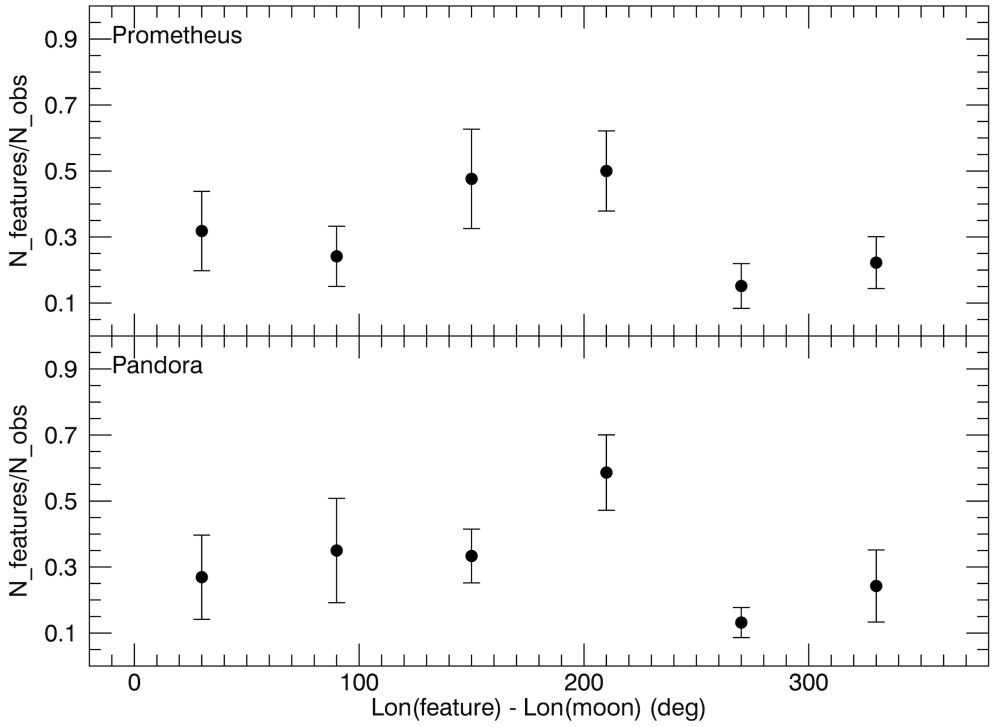

Figure 3.7: The longitude relationship between detected features and the F-ring shepherd moons Prometheus (top) and Pandora (bottom). Each point represents a bin 60° in width centered on the point. In both instances, we find the greatest concentration of kittens (relative to the total number of observations in those configurations) near longitudes opposite that of each moon. The bulk detection rate is 0.31.

estimate the total mass of aggregates in the F ring by summing:

$$M = \sum_{dr_{\min}}^{dr_{\max}} N_{dr} m_{dr} \tag{3.14}$$

Correcting for an order-of-magnitude error in their calculation, Meinke et al. (2012) estimate the total mass of F-ring kittens as 6.1×10^{15} kg. The features detected in this study imply a value of approximately 10^{16} kg. The total mass of all of Saturn's rings is believed to be within an order of magnitude of the mass of Mimas ($M_{\rm M} \approx 3.8 \times 10^{19}$ kg), so for one component of one tenuous ring to account for $\sim 10^{-3}$ of that mass seems implausibly high.

To evaluate the plausibility of these values, we need to independently estimate the mass of both the F ring and the aggregates within it. The primary means for estimating density within the rings is by measuring the changing wavelength of spiral density waves, however no such waves exist in the F ring. Here we will attempt to use the known surface-mass density of the A ring to derive a value for the F ring by comparing the ring's equivalent depths. Equivalent depth is the optical-depth analog to the property of equivalent width often computed for spectral lines. It is given by

$$\epsilon = \int \tau(r) dr \tag{3.15}$$

and acts as a proxy for the total amount of material in a given (linear) region. Here we make the assumption that two regions with the same equivalent depth should have the same surface-mass density and that σ changes linearly with ϵ. Such a relationship between σ and ϵ only holds if each compared region has the same particle-size distribution, as changing particle size can change the optical depth created by a fixed amount of mass. Since the dusty F ring likely has a much larger proportion of small particles than the A ring, the values derived here probably overestimate masses in the F ring (French and Nicholson, 2000; Bosh et al., 2002).

To estimate the mass of the F ring, we examined 12 occultations which displayed an unperturbed core. Each observation was binned to a radial resolution of 100 m and the

equivalent depth of the core was integrated across a region defined by its full width at half-max. For occultations in which more than one strand was visible, the most optically-thick was measured. In each observation, the equivalent depth of the A-ring region from 125,500 - 125,600 km was also computed. This comparison region was selected because it is unperturbed by any density waves and free of large-scale optical depth variation. Tiscareno et al. (2007) give the surface-mass density of this region as 375.1 kg/m^2. We can then estimate the surface-mass density of the F-ring core by

$$\sigma_{\text{core}} = \left(\frac{\epsilon_{\text{core}}}{\epsilon_{\text{A ring}}}\right)\left(\frac{\Delta r_{\text{A ring}}}{\Delta r_{\text{core}}}\right)\sigma_{\text{A ring}}. \tag{3.16}$$

If we assume the F-ring core has a vertical height commensurate with its radial width, we can convert to the volume-mass density $\rho_{\text{core}} = \sigma_{\text{core}}/\Delta r_{\text{core}}$. Table 3.2 shows the results of this analysis, which indicates an F-ring core density of 0.0092±0.0063 kg/m^3. The high variation of this value is representative of the extremely-variable nature of the ring. The core width Δr of 13.6±5.7 km is indeed consistent with the vertical height of 13±7 km found by Scharringhausen and Nicholson (2013), indicating a nearly-circular cross-section.

If we consider the F ring core to be a circular ring of cross-sectional diameter 13 km and radius 140221 km, it would have a volume of about 10^{17} m^3. Filling such a volume to a uniform density of 0.0092 kg/m^3 would require a ring mass of 9.4×10^{14} kg. This is more than an order of magnitude less then our computed aggregate mass.

A similar approach can be used to estimate the density, and thus the mass, of a single clump. Most features have a larger ϵ per km than the core in which they are embedded (an exception is relatively-tenuous features that lie on the edge of the core and are thus still prominent). If we assume the increase in optical depth (and thus surface-mass density) occurs from material confined in the clump region, we can estimate directly the density of the feature. We make this estimate by computing ϵ in the core region excluding the feature and then computing the equivalent depth for the added structure separately. Figure 3.8 illustrates how these regions were defined and table 3.3 gives the values for each occultation

Occultation	ϵ_{core} (km)	Δr_{core} (km)	$\epsilon_{\text{A ring}}$ (km)	σ_{core} (kg/m^2)	ρ_{core} (kg/m^3)
126 Tauri, rev 10	16.6	15.3	552.9	73.9	0.0048
σ Sagittarii, rev 11	30.6	18.7	595.9	103.1	0.0055
λ Scorpii, rev 29	15.4	8.6	570.8	116.8	0.0135
α Arae, rev 33	17.0	7.5	643.1	131.9	0.0176
κ Centauri, rev 36	19.3	8.3	631.5	138.3	0.0167
δ Persei, rev 39	19.1	16.8	662.8	64.1	0.0038
α Arae, rev 65	23.1	15.6	476.1	74.4	0.0048
α Arae, rev 85 (in)	24.8	9.1	724.2	140.3	0.0153
β Centauri, rev 92	28.8	26.1	766.4	53.9	0.0021
β Centauri, rev 102	22.0	15.0	717.1	76.4	0.0051
ζ Centauri, rev 112	16.1	15.2	724.8	54.5	00.36
θ Carinae, rev 190	17.3	7.1	728.8	125.0	0.0176
Mean	20.8	13.6	672.0	96.1	0.0092
Standard deviation	5.1	5.7	72.6	33.3	0.0063

Table 3.2: Observations used to estimate the density of the F-ring core. $\Delta r_{\text{A ring}}$ was within 200 m of 100 km for every observation.

Occultation	$(\epsilon/dr)_{\rm core}$	$(\epsilon/dr)_{\rm clump}$	Clump/core	$\rho_{\rm clump}$ (kg/m^3)
126 τ, rev 8	3.3	6.3	1.9	0.09
b Centauri, rev 57	5.4	10.8	2.0	0.10
β Centauri, rev 77 (in)	3.3	4.9	1.5	0.02
β Centauri, rev 89	2.9	6.5	2.3	0.08
δ Centauri, rev 98	2.7	4.1	1.5	0.04
α Arae, rev 98 (in)	1.6	3.9	2.5	0.11
σ Sagittarii, rev 114	2.9	2.7	0.9	-
ϵ Canis Majoris, rev 174 (in)	3.9	4.9	1.2	0.02
Mean	3.3	5.5	1.7	0.10
Standard Deviation	1.1	2.5	0.5	0.04

Table 3.3: Observations used to estimate the density structures in the F ring. Data were binned to approximately 100 m for all occultations.

in which the core and feature were easily separable.

The resulting average value of 0.10 ± 0.04 kg/m^3 is more than three orders of magnitude less than that used by Meinke et al. (2012) and four orders less than that assumed in Barbara and Esposito (2002). Using this new value, the total F-ring aggregate mass implied by our detected features is about 4×10^{12} kg or bout 0.5% our estimate F-ring mass. Such a aggregate mass is similar to that of Anthe, a small icy satellite with a diameter on the order of 1 km.

We can use our simple accretion-fragmentation model to evaluate how the F ring would behave in both the dense-aggregate and diffuse-aggregate situations. For collision velocities averaging 1 m/s (Attree et al., 2012) and an F-ring volume of 10^{17} m^3, we can write (see equation 3.9) the coefficients of the collision kernel as $k_{\rm dense} = 3.17 \times 10^{-19}$ and $k_{\rm diffuse} = 5.61 \times 10^{-17}$. In the dense case, we take the mass of the ring to be ten times that of the clumps embedded within, $M_{\rm dense} = 10^{17}$ kg. For the diffuse scenario, we use the F-ring mass estimated from equivalent depth, $M_{\rm diffuse} = 9.4 \times 10^{14}$ kg. To prevent clumps from growing unbounded, we limit the largest clump to twice the largest observed feature. Accretions which reach this limit are disrupted into smaller objects, as if by Saturn's tidal forces.

Figure 3.9 shows the size distribution for clumps formed in these two cases. It shows

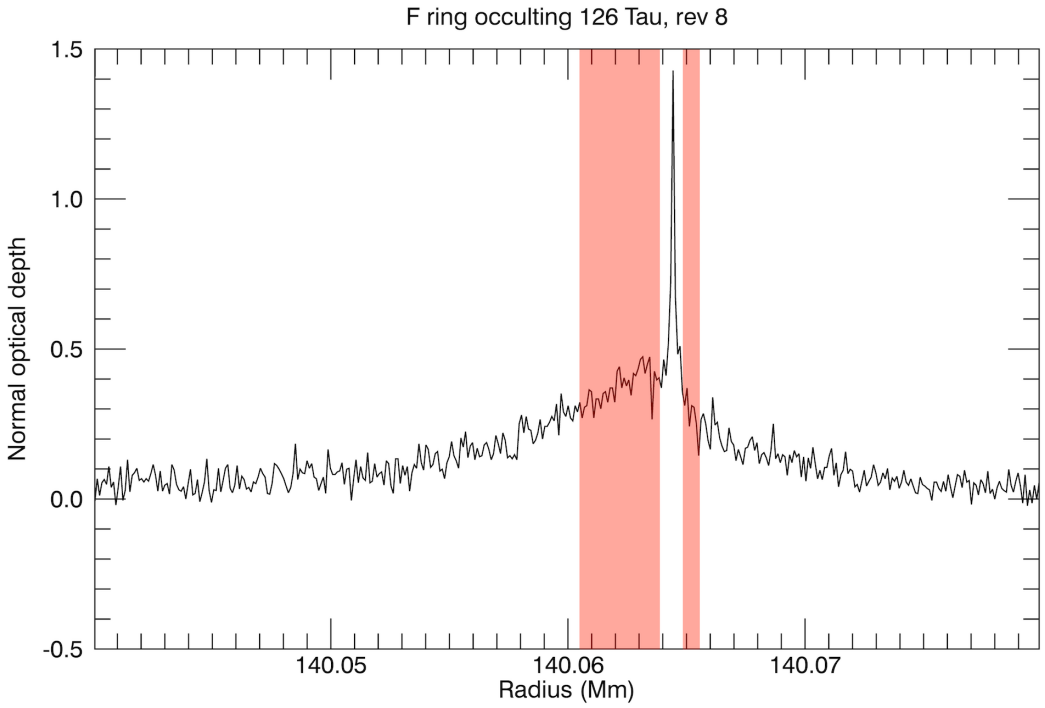

Figure 3.8: Schematic showing how the density of a features is measured. The shaded regions represent the F-ring core, while the region in between represents the kitten. Each area has its equivalent depth computed, with the two core regions being combined into one.

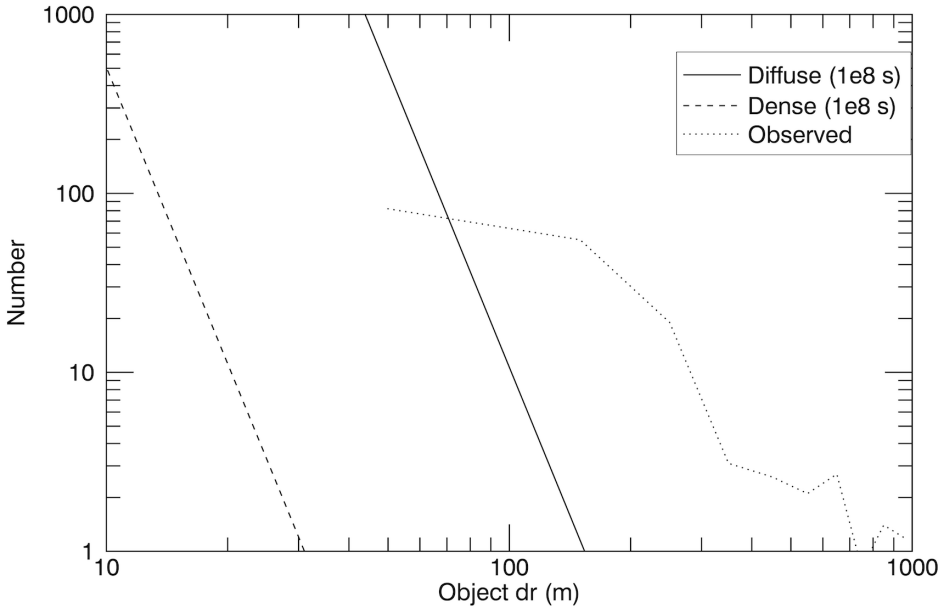

Figure 3.9: Clump size distributions resulting from the diffuse- and dense-object regimes compared to the observed features. Each simulation was initialized with no clumps and run for 1×10^8 s to achieve steady state.

that the diffuse ring produces a number of clumps that is more similar to the number observed. However, in neither situation does simple binary accretion reproduce what we actually observe. The diffuse simulation does produce a similar number of $dr = 70$ m features, but, as discussed above, the occultations are probably undercounting the true number of small objects due to insufficient resolution.

3.5 Discussion

Our results imply a population of structures within the F ring consistent with those reported by Meinke et al. (2012). However, we argue that these F-ring features are substantially more diffuse than previously estimated. A mass of clumps on the order of 10^{16} kg is simply too large to be plausible when considered in the larger picture of Saturn's rings. This is especially true given that the F ring as a whole must consist of substantially more mass than just the clumps.

In fact, it is worth considering whether a term like "clump" is even appropriate for the majority of these structures. A feature approximately twice as optically-thick as the surrounding ring material seems more an over-density that any coherent, independent object. A plausible alternative explanation for these features is that they represent "skirts" of material loosely attracted by the denser and more-coherent moonlets. Such density enhancements, while obvious in our high-resolution stellar occultations, may be undetectable by even high resolution imaging.

This concealment is demonstrated by analyses of ISS F-ring images. Beurle et al. (2010) present three 28° degree mosaics in which they identify 28 structures indicating the presence of moonlets. Assuming each structure to correspond to a unique moonlet, this indicates a population of 120 bodies in the entire ring. Colwell et al. (2009) present a high-resolution image and identifying six moonlet-driven structures in 0.2° of ring longitude. This corresponds to a population of 1718 moonlets. If we assume our two moonlets are spherical which a mean dr of 332 m, we estimate 4800 such bodies in the entire ring. Imaging searches

may have an especially difficult time identifying features that lie near the densest (and thus brightest) parts of the core.

If we identify our non-moonlet detections as accumulations of material around these objects, we find that material would accumulate as much as 13 times larger than the solid object itself (4316 m). However, a 332-m moonlet with a density of 235 kg/m^3 has a Hill radius of only 569 m, so these accumulations cannot be permanent. It seems more likely that these diffuse structures have multiple origins. Some may slough off of moonlets, while others form through independent aggregation. Still others may represent simple fluctuations of the F-ring's density viewed from convenient angles.

Our result that kittens are observed most often in configurations where the point of observation and Prometheus are on opposite sides of the planet is consistent with the results of Esposito et al. (2012) and inconsistent with the results of Hedman et al. (2011). However, it should be noted that the latter used different techniques to analyze data collected from a different instrument, so we may not in fact be observing the same population of physical objects. Prometheus and the F ring have a synodic period of 67.6 days, so these results indicate that the features we are probing are most evident about a month after the moon's encounter with the ring.

The relationship with Prometheus and (a lesser one with) Pandora support the notion of tenuous structures, which can regularly form and disperse on the order of a month. It also seems to rule out these features as mainly detections of the so-called "streamer-channels" imposed gravitationally on the ring by Prometheus' close approach. Streamer-channels are observed to persist in the rings for many synodic periods (Murray et al., 2005). However, the creation of kittens likely occurs in parallel with these larger, more-obvious structures.

3.6 Conclusions

With nearly twice the data as previous studies, we confirm the presence of a population of density features in the F ring. These features range in radial size from tens of meters to

more than a kilometer and their distribution is consistent with a power law for structures of intermediate size. The less-tenuous "moonlet" class of objects appears to be rarer than previously imagined; despite a substantial increase in F-ring occultations, we detect no additional moonlets.

We correct previous (e.g., Barbara and Esposito (2002); Esposito et al. (2008); Meinke et al. (2012)) characterizations of the remaining features. Optical depth comparisons with the better-understood A ring indicate that these structures have densities orders of magnitude lower than previously considered. These less-massive aggregates are also more consistent with reasonable values for the mass of the tenuous F ring. The mechanisms which construct them remain poorly-understood, but it seems implausible that they form solely through binary accretion processes.

Chapter 4

Direct Detection of Gaps in the Main Rings

4.1 Introduction

Evidence that Saturn's rings are structurally inhomogeneous on small scales predates the *Cassini* mission. Ground-based observations revealed that the main rings were brighter at their ansae (the locations of greatest observed radial extent) than at the sub-observer point (Ferrin, 1975; Price and Baker, 1975; Lumme et al., 1977; French et al., 2007). Detailed analyses of *Voyager* images by Dones et al. (1993) demonstrated that such a brightness asymmetry is not an effect of Earth-based observation. Since the arrival of *Cassini*, observations by the Composite Infrared Spectrometer (Ferrari et al., 2009), Ultraviolet Imaging Spectrograph (Colwell et al., 2006, 2007), and Visual and Infrared Mapping Spectrometer (Hedman et al., 2007c) have provided confirmation across a broad range of wavelengths.

Colombo et al. (1976) and Franklin and Colombo (1978) showed that such an asymmetry could be produced by series of aligned particle wakes. Theory and simulations indicate that such structures coalesce through self-gravitation and are sheared by differential Keplerian rotation (Salo, 1995; Salo et al., 2004). Simplified "granola bar" models of these wakes have been shown to reproduce the varying brightness observed in occultations by UVIS and VIMS, but this remains indirect evidence for the presence of self-gravity wakes in Saturn's A ring (Colwell et al., 2006; Hedman et al., 2007c). This chapter presents the direct detection of these wakes, namely the gaps that represent the features' minima. It has been submitted for publication in Icarus.

4.2 Data

This study uses stellar occultations observed by the High Speed Photometer (HSP) of the *Cassini* Ultraviolet Imaging Spectrograph (UVIS), described in detail by Esposito et al. (2004). A discrete optical train within the spectrograph, HSP measures flux from a target star on a rapid cadence, 500 or 1000 Hz for the observations used in this work.

4.2.1 Optical depth and geometric solution

The target star's flux I_0 is attenuated by any material between the star and the instrument. We assume that all such attenuation is the result of material in Saturn's rings. For a region of the rings with line-of-sight optical depth τ, the flux reaching HSP is $I = I_0 e^{-\tau} + b$, where b is the background of ancillary light entering the aperture of the photometer. The instrument measures $I\Delta t$ for each sampling period Δt. Although, in an ideal situation, I_0 would remain constant for the duration of the observation (ignoring stellar variability), HSP actually becomes more sensitive as an observation progresses (Colwell et al., 2007). To account for this "ramping up," we use a variable I_0 measured in unocculted regions and interpolated elsewhere. The background b is conversely measured at locations of complete attenuation.

We can rearrange the above formula and account for the spacecraft's angle of elevation with respect to the rings B to derive an expression for the normal optical depth $\tau_\perp$:

$$\tau_\perp = \tau \sin B = \ln\left[\frac{I_0}{I-b}\right] \sin B. \tag{4.1}$$

All references to the optical depth in this paper refer to $\tau_\perp$.

We use the method of Albers et al. (2012) to convert an array of observation times to coordinates in the ring plane through knowledge of the position and orientation of the planet and spacecraft derived from NAIF SPICE[1] . Longitude in this system is measured

[1] Geometry code provided by M. Sremčević.

prograde from the ascending node of Saturn's equatorial plane on Earth's J2000 equator. We can estimate the uncertainty in the absolute radial coordinate by comparing the computed location of the inner Encke Gap edge with the location tabulated in French et al. (1993). For the observations used in this study, the 1-σ radial uncertainty is 0.32 km. Gap sizes, however, are a relative measurement and not subject to the absolute radial uncertainty.

4.2.2 Resolution

For a study of such small structures, we must carefully examine the resolution of our observations. The simplest measure of this is the geometric resolution r_{G}, which is the change between where the line of sight from HSP to the occulted star pierces the ring in one integration period to where it does so in the next. This varies by less than a meter in the occultations used in this study and the largest value for each observation is listed in table 4.1.

Of course, stars aren't truly point sources, so they have a projected diameter on the ring. With a small-angle approximation, we can estimate the projected star diameter r_{S}:

$$r_{\mathrm{S}} = 2\frac{d_{\mathrm{ring}} r_{\mathrm{star}}}{d_{\mathrm{ring}} + d_{\mathrm{star}}}, \tag{4.2}$$

where d_{ring} and d_{star} are the distance from *Cassini* to the ring and star, respectively, and r_{star} is the radius of the star.

We estimate the diffraction limit of our observations as the size of the Fresnel zone, $r_{\mathrm{F}} = \sqrt{\lambda D/2}$, where λ is the wavelength of the occulted light and D is the distance to the occulting material. The values listed in table 4.1 are computed with $\lambda = 190$ nm, the longest wavelength observed by HSP.

Unless otherwise noted, references to the resolution in this paper are to the geometric resolution. In no observation is the geometric resolution substantially different from the diffraction limit.

Occultation	r_G (m)	r_S (m)	r_F (m)
β Lupi R57	9.8	0.95[a]	8.4
ζ Centauri R60	9.3	1.04[b]	9.4
ζ Centauri R62	9.1	0.81[b]	8.3
ϵ Centauri R65	10.0	1.1[c]	9.2
β Crucis R98	6.1	1.8[d]	8.8
α Virginis R134	10.1	0.63[e]	5.2
α Virginis R173_out	8.4	1.8[e]	8.8

Stellar radii: [a]Underhill et al. (1979), [b]Fitzpatrick and Massa (2005), [c]Hohle et al. (2010), [d]Cohen et al. (2008), [e]Harrington et al. (2009)

Table 4.1: Several measures of the radial resolution of the occultations used in this work. See section 4.2.2 for an explanation of each measure. All projected stellar radii r_S are computed using distances from Hipparchus (van Leeuwen, 2007).

4.2.3 Data selection

Occultations are labeled by the star occulted and the *Cassini* revolution during which the observation occurred. In some observations, the track of the occultation through the ring plane moves both inwards and outwards. We treat the ingress and egress as separate occultations and they are labeled with an 'in' or 'out' after the *Cassini* rev. By this standard, HSP has observed more than 200 stellar occultations since the arrival of *Cassini* at Saturn. Because this work examines the rings on their smallest scale, however, we select only observations that match certain requirements.

We restrict our dataset to those observations that meet the following criteria in the A ring:

(1) Radial resolution ≤ 10 m

(2) $I_0 \Delta t > 100$ counts

(3) Complete coverage of A ring

(4) Not occulting a "visual" double star[2]

Table 4.2 lists the occultations that meet these criteria and are included in this study. The selected observations span a period of time from 26 January 2008 to 19 October 2012.

4.2.4 Self-gravity wake geometry

We adopt a coordinate system defined by increasing ring-plane radius from Saturn and the direction of orbital motion. All angles are measured in a positive direction from the positive radial axis, as depicted in figure 4.1. Due to the motion of *Cassini*, in each successive integration period the point at which the occultation pierces the rings falls on a different location. We call the track angle $\phi_{\rm track}$ the instantaneous angle at which this point is moving. We call the viewing angle $\phi_{\rm view}$ the instantaneous angle made between the

[2] β Centauri, β Crucis, and α Virginis are spectroscopic binaries, but this has no bearing on an occultation.

Occultation	$I_0\Delta t$	B (deg)	$\phi_{\rm track}$ (deg)	$\phi_{\rm view}$ (deg)	Gaps
β Lupi R57	151.6	49.6	154.3	228.5	52537
ζ Centauri R60	210.0	53.6	170.6	230.1	53061
ζ Centauri R62	213.8	53.6	9.0	67.9	70584
ϵ Centauri R65	262.0	59.6	172.6	228.0	49786
β Crucis R98	273.9	65.2	155.8	198.4	123911
α Virginis R134	150.8	17.3	151.8	291.0	50428
α Virginis R173_out	123.2	17.3	302.3	95.4	49510

Table 4.2: An overview of the relevant parameters for the occultations used in this work. All values are averaged across the A ring. The track and viewing angles typically vary less than 1° across the ring.

positive radial direction and the vector from the spacecraft to the occulted star. The pitch angle $\phi_{\rm wake}$ is the angle at which the self-gravity wake structures are canted. Our pitch angle is defined differently than in other works:

$$\phi_{\rm wake} = 180^\circ - \phi_{\rm Colwell,\ Hedman} = 90^\circ + \phi_{\rm Salo}. \tag{4.3}$$

See section 3 of Hedman et al. (2007c) and figure 6 of Salo et al. (2004) for their definitions.

Although we make our measurements in dr, through knowledge of the pitch and track angles, these can be converted to the true gap width S. Since $\phi_{\rm wake} > 90^\circ$,

$$S = dr \left| \frac{\sin(\phi_{\rm wake} - \phi_{\rm track})}{\cos \phi_{\rm track}} \right|. \tag{4.4}$$

Note that S has a pole where an occultation changes radial direction ($\phi_{\rm track} = 90^\circ, 270^\circ$).

4.3 Methods

We employ a variation of the m-test algorithm developed for the Uranian rings by Colwell et al. (1990) and used subsequently to investigate clumping in Saturn's F ring (Esposito et al., 2008; Meinke et al., 2012). This technique searches for consecutive series of highly statistically-unlikely data points within a given observation. Our modified version, described below, searches for tenuous regions rather than dense ones and applies more stringent constraints.

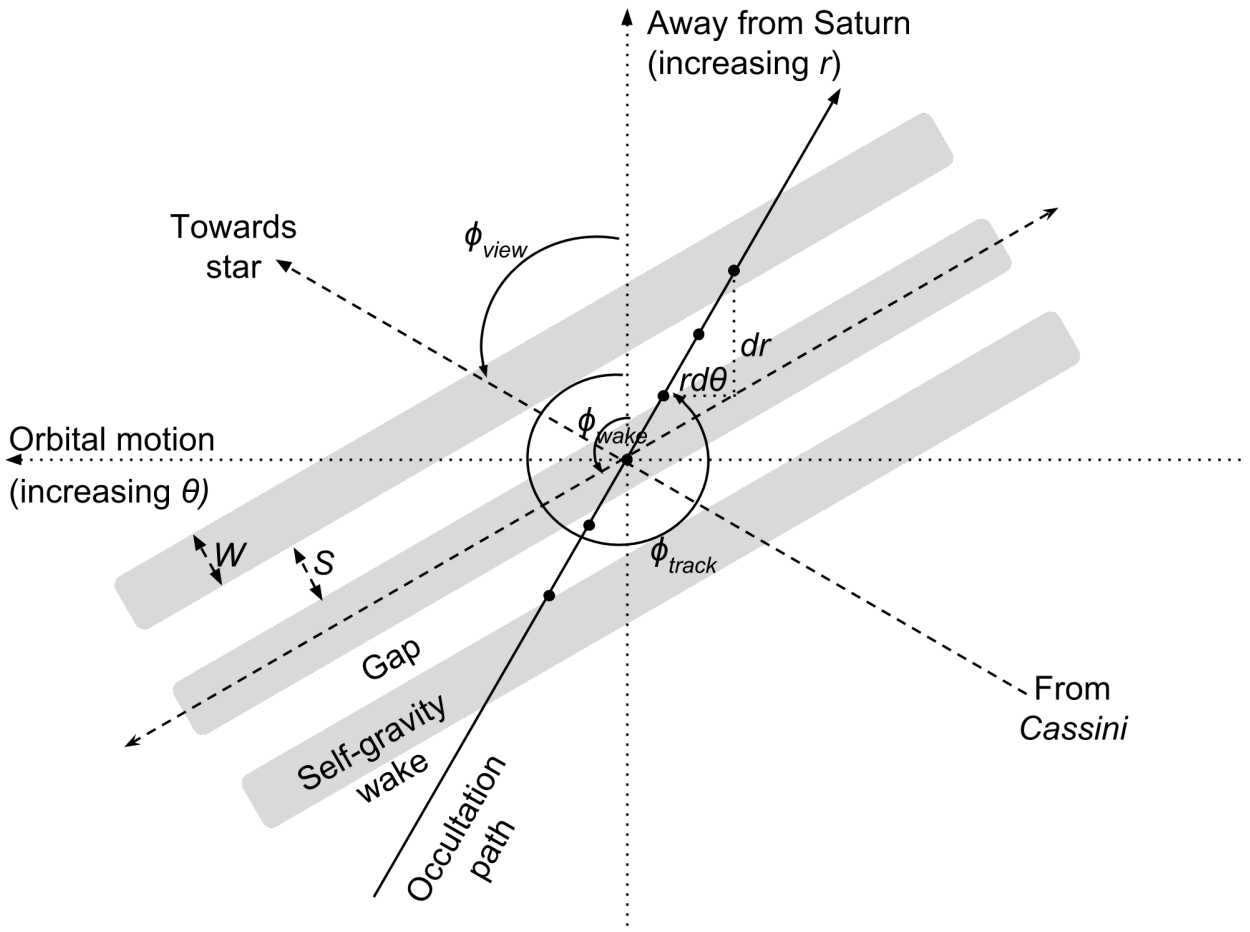

Figure 4.1: A schematic of the coordinate system used in this work. Each small dot represents the center location of one integration period. The granola bar model assumes the length of each wake is infinite.

4.3.1 Computing m

For an observed signal well-described by the Poisson distribution, the probability of observing k counts from a source averaging λ counts per integration period is:

$$P(k, \lambda) = \frac{e^{-\lambda}\lambda^k}{k!}. \tag{4.5}$$

When searching for tenuous features (where k is larger than the surrounding background), we can compute the likelihood of an integration period resulting in k *or more* counts by summing:

$$P(\geq k, \lambda) = 1 - \sum_{j=0}^{k} \frac{e^{-\lambda}\lambda^j}{j!}. \tag{4.6}$$

The probability m that such an event occurs in this observation, then, is the cumulative probability multiplied by the number of data points in the observation N:

$$m = N \times P(\geq k, \lambda). \tag{4.7}$$

Because the selected occultations are purposefully among the brightest available, all trigger the square-root data compression mode of UVIS (Colwell et al., 2010). This is lossy compression, so the resulting data vector cannot contain all possible integer values represented by the Poisson distribution; instead, our data samples this curve at intervals. We compute the mean λ in a 1-km region surrounding each data point. Thus, the mean can respond to local changes in the background optical depth. We account for the compression as done in Meinke et al. (2012) by adopting a threshold m of 0.1, meaning we reject any point likely to occur once by random in ten or fewer occultations.

We also introduce a new constraint by requiring a feature to consist of at least two consecutive m-test-significant points. This increases the minimum detectable feature size in exchange for increased confidence that an observed detection is real. The practical effect of this is that, for each observation, the smallest gap we can detect is twice the geometric resolution r_{G} listed in table 4.1.

4.3.2 Filtering by optical depth

By their nature, gaps must have a lower optical depth than the ring material in which they are embedded. To quantify this, we filter our m-test-significant features to select only those in which the optical depth of the gap $\tau_{\rm gap}$ is substantially lower than that of the surrounding ring $\tau_{\rm back}$. By fitting the granola bar model to a set of UVIS occultations, Colwell et al. (2006) found the mean optical depth of the gaps to be 0.12 across much of the A ring. VIMS occultations analyzed by Hedman et al. (2007c) yield a similar result. This is approximately a quarter of the typical A-ring optical depth of 0.5, so we adopt a threshold $\tau_{\rm gap}/\tau_{\rm back} = 0.25$. The specific implementation of the "optical depth ratio" is:

$$\tau_{\rm gap}/\tau_{\rm back} = \frac{\text{Median } \tau_\perp \text{ of feature}}{\text{Median } \tau_\perp \text{ of surrounding 1-km region}}. \tag{4.8}$$

Thus, the optical depth ratio is computed over the same region as the Poisson mean and can conform to local changes in the optical depth, such as density waves (which have wavelengths greater than 1 km).

4.3.3 Gap parameters

For each gap that is identified by the algorithm, its radial width dr is estimated as the radial displacement from the outermost significant point to the innermost one. Its track angle $\phi_{\rm track}$, viewing angle $\phi_{\rm view}$, radial location, and observation time are all taken as the median value for the feature.

4.4 Results

The algorithm described in section 4.3 was run over the range [122340, 136780] km for each observation listed in table 4.2. This table lists the number of gaps detected for each observation; they total to 449,817 features. This section describes the nature of the gaps themselves, their radial distribution in the A ring, and comparisons to prior work. Figures

4.5 through **??** plot quantities radially across the A ring. Refer to figure 4.2 for a plot of how the optical depth varies across the same region.

4.4.1 Gap morphology

4.4.1.1 Gap shape

Figure 4.3 depicts the typical appearance of detected gaps in the A ring. The leftmost pair of detections illustrates a potential shortcoming of the search algorithm, as its very fine resolution can sometimes split into two a feature a human might label as a single phenomenon. Conversely, the requirement of two or more consecutive significant points can sometimes eliminate the smallest structures, like the dip observable around 0.05 on the abscissa. Anecdotally, the latter case occurs more frequently than the former and we are confident that our search is undercounting the true population of gaps in these observations.

The region also shows the typical morphology of A-ring self-gravity wakes, in which we observe alternating regions of compression and rarefaction. Wider gaps, like the one that could be inferred from the concatenation of the leftmost two detections are often adjacent to wider wakes, like the ones visible immediately before or after the given gap. Narrower gaps, like those on the right, are adjacent to narrower wakes. The wavelength of 50-60 m implied by the rightmost three gaps and wakes is consistent with the Toomre wavelength for this region.

Meinke et al. (2012) demonstrated that the shape of an occulted aggregate can indicate its level of cohesion: straight sides and a flat bottom indicate a solid object, while a jagged appearance indicates a looser structure. Since the gaps detected in this study are generally only a couple of data points wide, there is insufficient resolution to draw a firm conclusion.

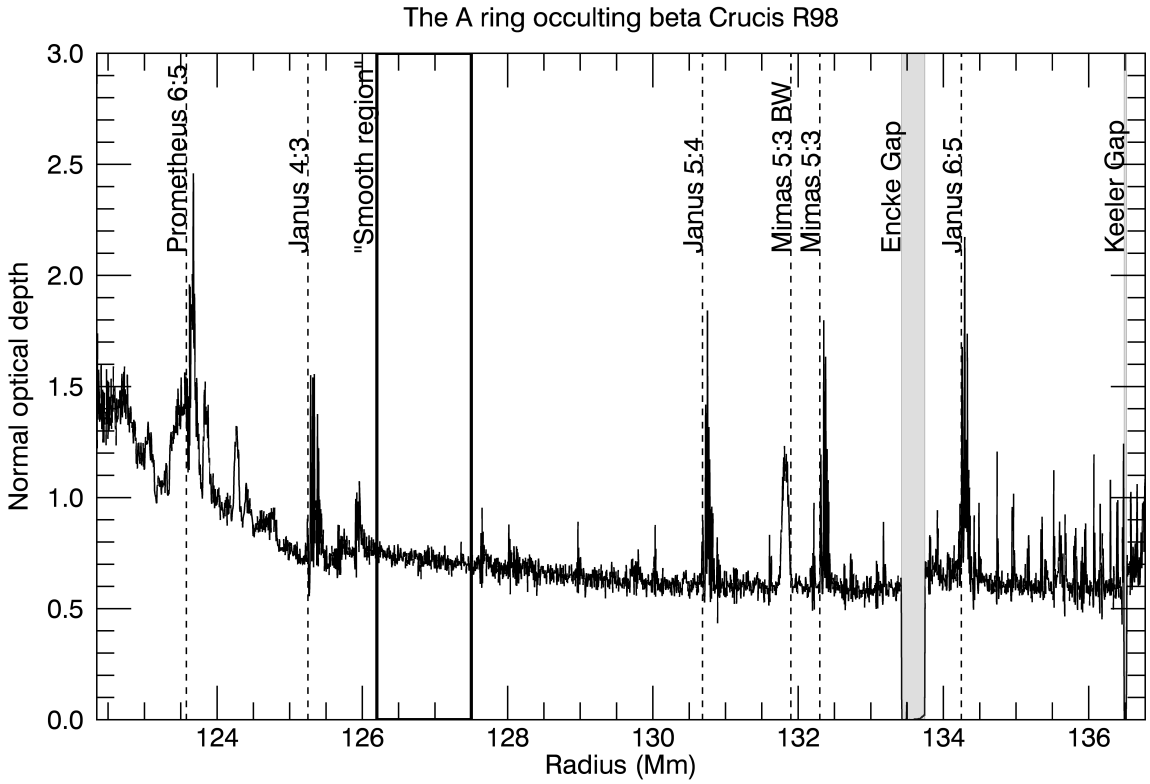

Figure 4.2: The normal optical depth of the A ring, binned at 5 km. The strong resonances discussed in this work are indicated with dashed lines. All are inner Lindblad resonances except for the Mimas 5:3 bending wave, denoted by BW. The Encke and Keeler gaps are shaded gray. The "smooth region" is used in section 4.4.1.2.

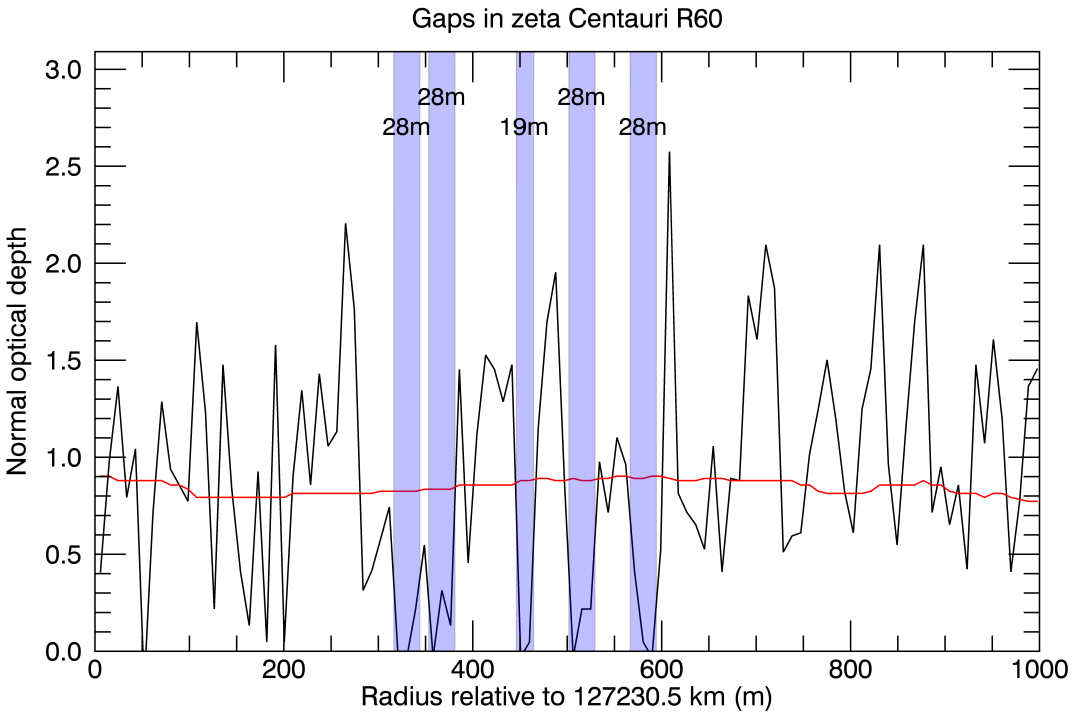

Figure 4.3: Five gaps (marked by the shaded rectangles) in the unbinned ζ Centauri R60 occultation. The horizontal red line gives the median-smoothed optical depth of the region and each identified gap is labeled with its dr.

4.4.1.2 Size distribution

Figure 4.3 demonstrates that gaps occur in different sizes. In figure 4.4 we plot the distribution of gap sizes, measured by their radial width dr. The dr of a gap is very dependent on orientation; two identical gaps could produce two different measurements of dr in two occultations of different ϕ_{track} and ϕ_{view}. To first order, however, these geometric corrections are consistent across a single occultation and thus should not affect the size distribution.

We can group the occultations into two broad categories by their gap size distributions. β Lupi R57, ζ Centauri R60, and ϵ Centauri R65 all have very similar and relatively steep distributions. ζ Centauri R62, α Virginis R134, and α Virginis R134_out all have similar and relatively shallow distributions. β Crucis R98 falls somewhat intermediately. For figures 4.5 through **??**, we adopt β Centauri R60 and β Centauri R62 as representative of the steep and shallow groups, respectively. Since both observations are of the same star, many other observing parameters are constant between the two.

We can fit the distributions in figure 4.4 with a power law of the form $y = 10^{bx+c}$, from which the power-law index b describes how steep or shallow the distribution is. Computing b in 50-km intervals across the ring allows us to examine how the distribution of gap dr changes with location. Figure 4.5 shows this for both the steep (top panel) and shallow (bottom panel) groups. In both cases we see shallower dr distributions at the location of strong density waves within the A ring, indicating that density waves are relatively rich in larger gaps. These additional large gaps are not simply the narrow, period-shortened outer end of the density wave train; even at their narrowest, the peaks and troughs of the wave train are still several times larger than the largest detected gaps. This is consistent with models that suggest that density waves may trigger increased aggregation of ring particles (Esposito et al., 2012). Our seven occultations, however, are insufficient in number to search for a possible phase lag in the strong A-ring density waves, which have $m \geq 4$.

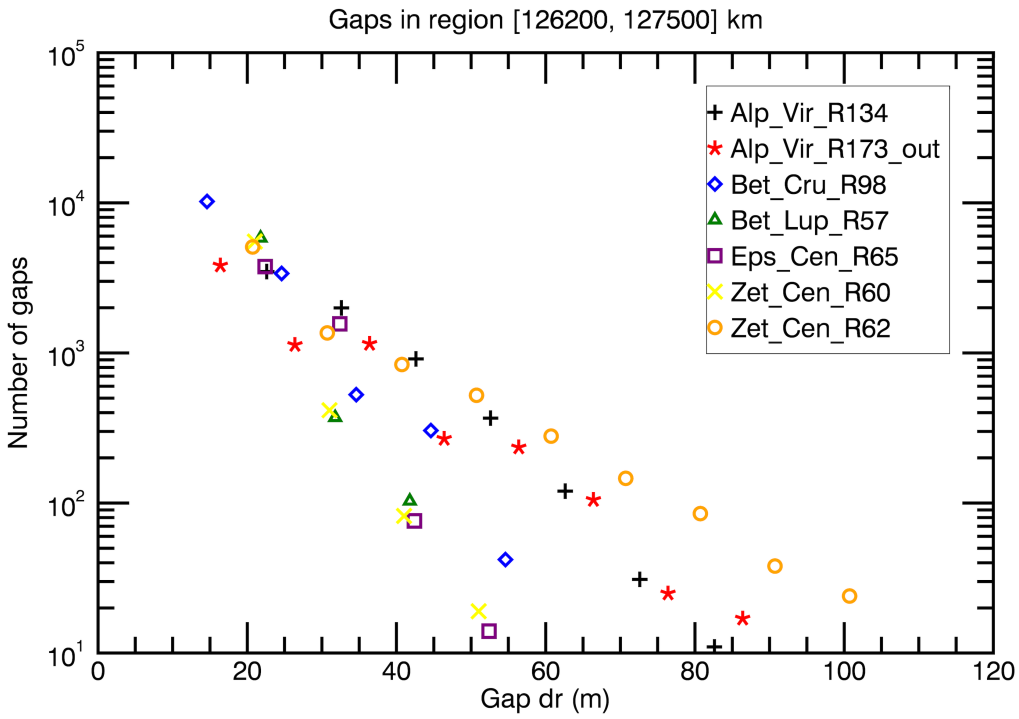

Figure 4.4: The distribution of gap sizes observed in a region of the rings containing no strong spiral density waves (see the "smooth region" of figure 4.2).

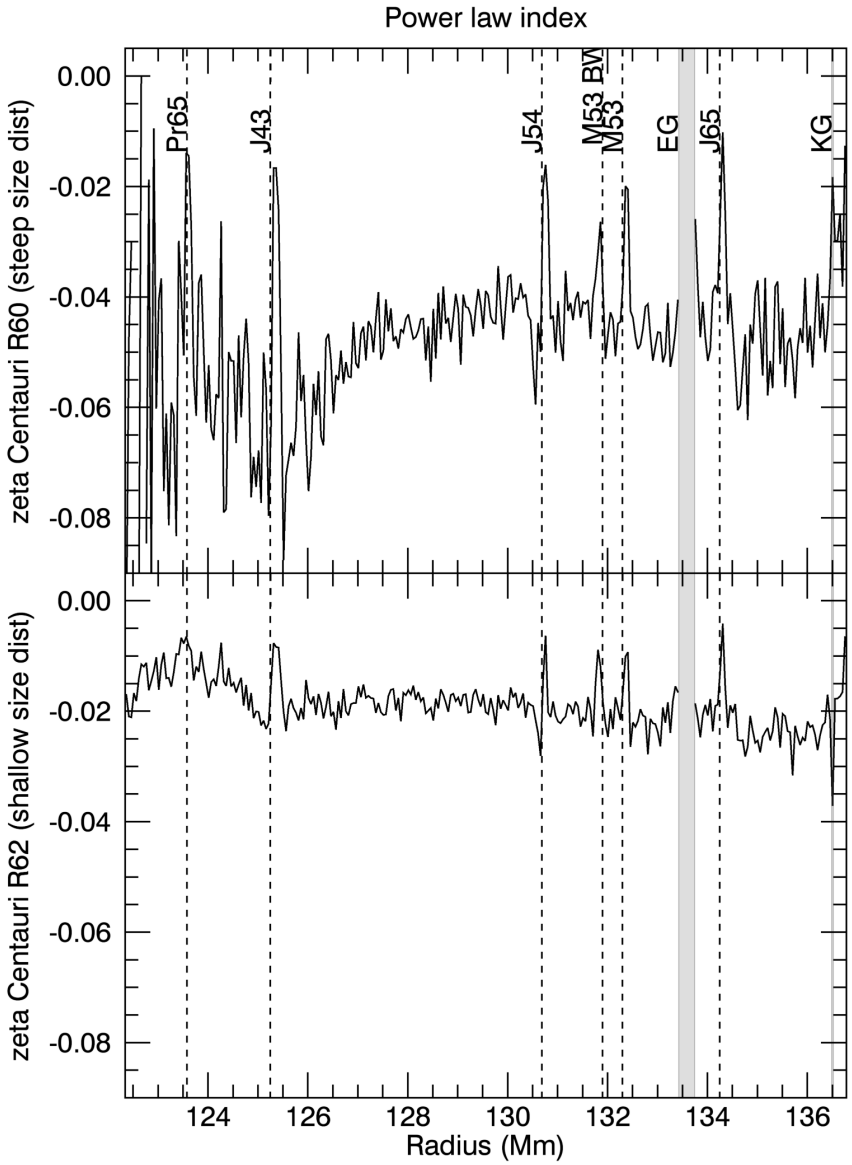

Figure 4.5: The variation of the power-law index b with radial location in the A ring. The top panel shows a member of the steep dr distribution group and the bottom panel a member of the shallow group.

4.4.2 Radial distribution

We can also plot a version of figure 4.5 that simply shows how the number of gaps detected varies radially. Figure 4.6 depicts these distributions for the ζ Centauri R60 and ζ Centauri R62 occultations. From this, we can make a surprising observation: although the number of gaps is generally depleted at the locations of strong density waves, this depletion is substantially less for occultations in the steep group. Most strikingly, this translates into a relative excess of detected gaps at the Janus 4:3 resonance location. Furthermore, although the number of gaps is depleted at the location of the Mimas 5:3 bending wave, the magnitude of this depletion is not affected by our choice of group.

Although it may appear as if gaps are impossibly forming in the Keeler gap, in reality this feature does not line up cleanly with our 50-km plotting bins. No gaps are detected in any observation in the Encke or Keeler gaps, as expected.

4.4.3 Comparisons to prior work

Previous studies have provided substantial indirect evidence for the presence of self-gravity wakes in the A ring. The typical approach is to observe the rings at several different viewing angles and quantify a change in brightness (reflected light for images, transmitted for occultations). The larger and more aligned the wakes, the larger the observed brightness asymmetry. If our detected gaps are indeed the minima between self-gravity wakes, they should vary in sync with changes in this asymmetry.

4.4.3.1 *Voyager* images

During their flybys of Saturn, the *Voyager* spacecraft took many images of the rings at different viewing angles. Dones et al. (1993) examined a pair of these images with nearly orthogonal viewing angles and extracted a brightness profile from each. The ratio of these profiles gives the magnitude of the brightness asymmetry, which is extracted from their

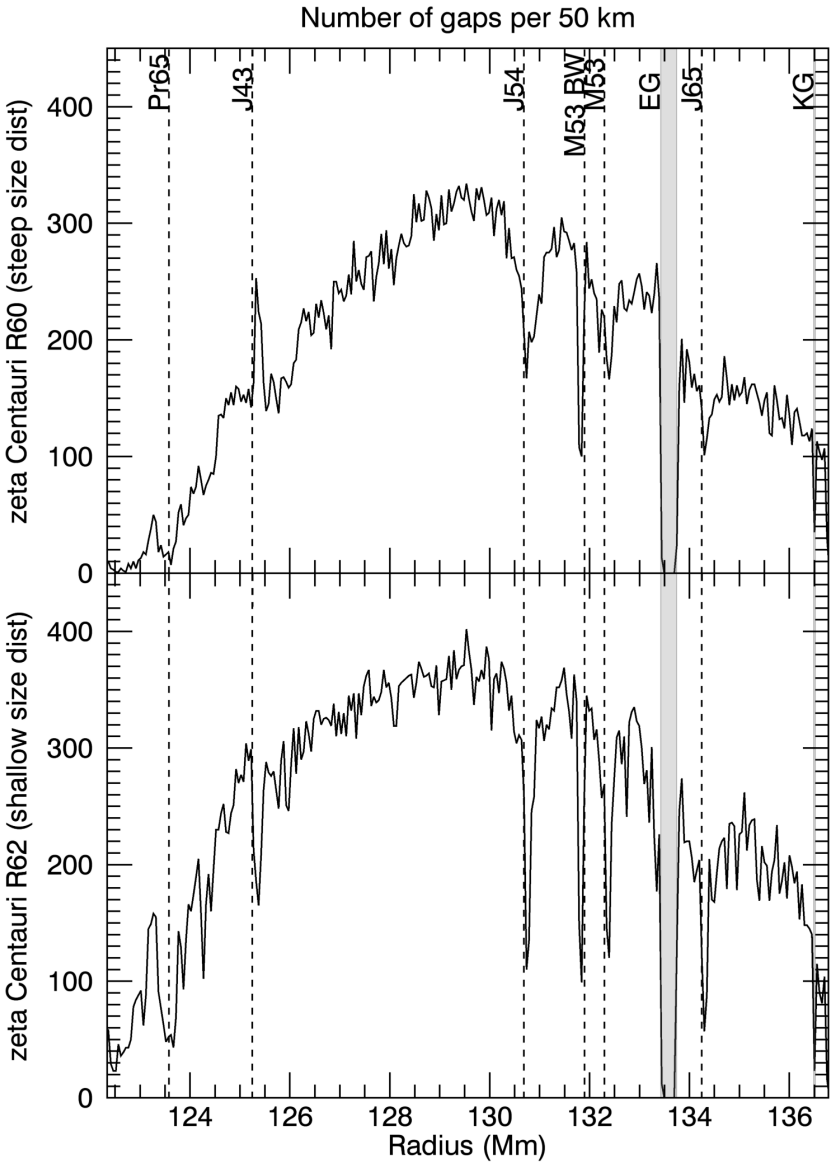

Figure 4.6: The variation of the number of detected gaps with radial location in the A ring. The top panel shows a member of the steep *dr* distribution group and the bottom panel a member of the shallow group.

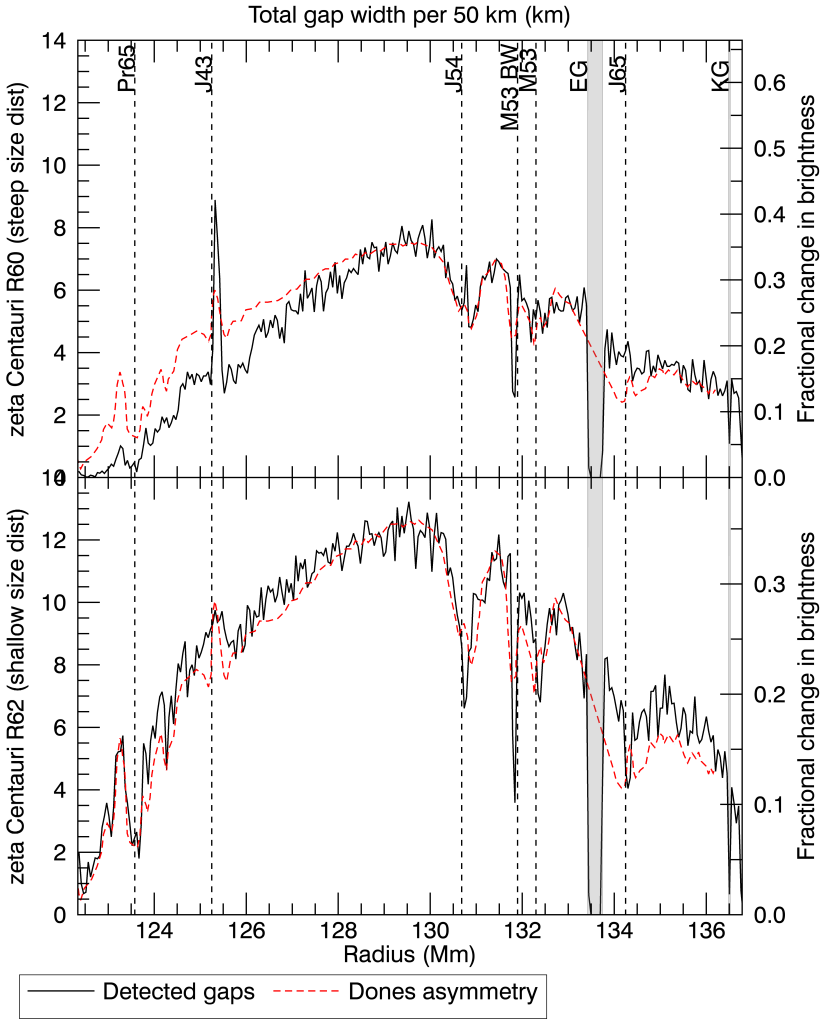

Figure 4.7: A comparison between the portion of the ring we observe to be gaps $\sum_i dr_i$ and the brightness asymmetry observed by Dones et al. (1993). The Dones asymmetry (red line) is plotted against the right axis.

figure 21 and plotted in red (dashed) in figure 4.7. It is evident that radial variation in the brightness asymmetry is matched by radial variation in the amount of gap area we detect. Clearly, *Voyager* did not observe the scenario with excess detected gaps around the Janus 4:3 resonance, as the ζ Centauri R60 occultation matches more poorly than does the ζ Centauri R62 one. Regardless, the agreement between our observations and the *Voyager* asymmetry is clear.

4.4.3.2 UVIS stellar occultations

Colwell et al. (2006) examined a series of stellar occultations observed by UVIS at different viewing angles and found variation in observed ring transparency. These brightness variations can be modeled by the simple granola bar model of self-gravity wakes, which approximates the optical depth of the wake maxima as infinity and their length as infinite (Colwell et al., 2007). Using equation 4 from Colwell et al. (2007) and best-fit wake parameters from Jerousek et al. (2016), we can compute the transparency implied by the granola bar model. These results, which are unique to each observation, are plotted in blue (dot-dashed) in figure 4.8.

The modeled transparencies have a generally-flatter distribution than the fraction of the ring we observe to consist of gaps. This model is also unable to account for the large discrepancy we observe around the Janus 4:3 resonance in some observations. Nevertheless, where the granola bar model predicts large drops in transparency, we detect a smaller portion of the ring is composed of gaps.

Beyond approximately 133,000 km, we do not reproduce the results of the transparency model. Colwell et al. (2006), however, also find difficulty in fitting this model to their data and note that a smaller fraction of the ring outside the Encke gap is composed of self gravity wakes, an observation entirely consistent with our own. Another possible factor is that the smallest particles, uniform over much of the A ring, appear to become smaller starting around 133,000 km (Jerousek et al., 2016). These smaller particles, possibly liberated from

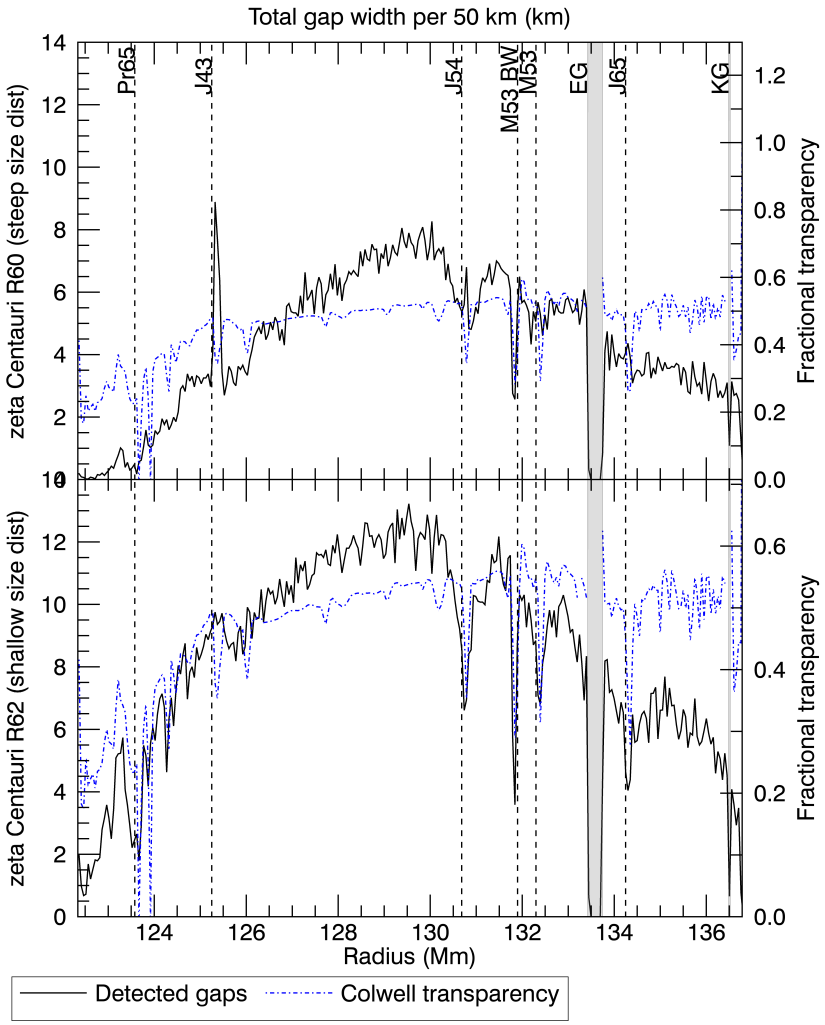

Figure 4.8: A comparison between the portion of the ring we observe to be gaps $\sum_i dr_i$and the transparency model of Colwell et al. (2006). The Colwell transparency (blue line) is plotted against the right axis.

the regolith of larger objects, could fill in the gaps, reducing their transparency and thus how easy they are to detect.

4.4.4 Gaps in the B ring

We performed a search with the same parameters on the B ring to limited effect. At most locations, the B ring is substantially more optically-thick than anywhere in the A ring and much of the central B ring is essentially opaque. Thus, our ability to detect gaps was severely limited. Nevertheless, some basic conclusions can be drawn. In the regions where the optical depth is similar to the A ring (beyond about 117,000 km), we observe gaps at a similar rate as in the A ring. The number of observable gaps is also still modified by the presence of spiral density waves; in general, more gaps are visible when a wave is present. Finally, we continue to see two modes in the appearance of the radial distribution of gaps. Figure 4.9 gives an example of how gaps are distributed throughout the B ring. For this observation, we detect 11,308 gaps in the B ring, as compared to 70,584 in the A ring, despite the fact that the B-ring search region (26,200 km) was nearly twice as large as the A-ring region (14,440 km).

4.5 Discussion

4.5.1 The origin of the gaps

If self-gravity wakes are indeed the explanation for the observed brightness asymmetry in the A ring, then our results are a clear direct detection of their minima. In occultations in which we don't see excess gaps around the Janus 4:3 resonance, we reproduce well both the *Voyager* brightness asymmetry and the occultation transparency asymmetry.

In figure 4.3, we have identified the regions between the gaps as where the UVIS line-of-sight to the star passes through a self-gravity wake. Measuring from the rightmost edge of the fourth gap to the rightmost edge of the fifth gap gives an estimated radial projection of

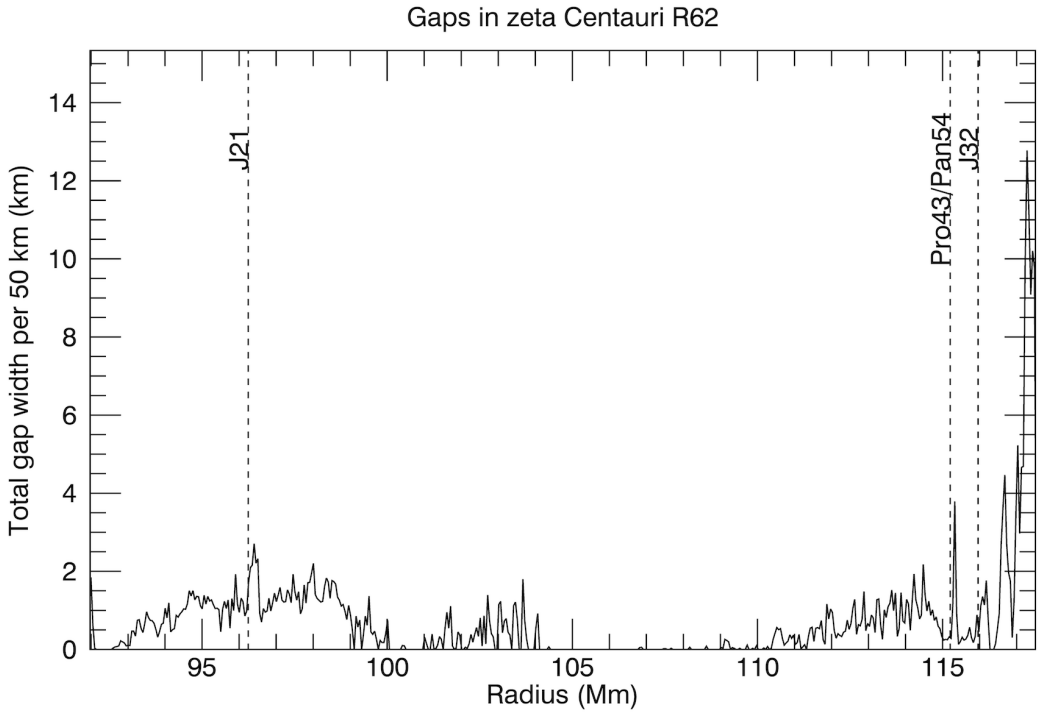

Figure 4.9: Radial distribution of gap width in the B ring. The central part of the B ring is essentially opaque in even the brightest stellar occultations.

the wavelength of 65 m. Salo et al. (2004) found that in simulations self-gravity wakes formed with wavelengths commensurate with the Toomre critical wavelength (Toomre, 1964):

$$\lambda_{\rm cr} = \frac{4\pi^2 G\sigma}{\kappa^2}, \tag{4.9}$$

where σ is the local surface mass density, κ is the local epicyclic frequency, and G is the gravitational constant. At the location of figure 4.3 and assuming a surface mass density of 40 g/cm^2, this gives a wavelength of 57 m. By rearranging equation 4.4 and setting $dr = 65$ m and $S = 57$ m, we find $\phi_{\rm wake} = 110.7°$, consistent with previous results (Colwell et al., 2006; Hedman et al., 2007c; Ferrari et al., 2009; Jerousek et al., 2016).

Our observations are not entirely consistent with simple models of self-gravity wakes, however. In the granola bar model, observations with a track angle generally perpendicular to the wakes would see more gaps per unit of radial distance than observations with tracks generally parallel to the wakes (see figure 4.10). We do not find substantial variation in the number of detected gaps with different observing geometries. Only in one observation, β Crucis R98, did we find markedly more gaps (see table 4.2).

One explanation for this outlier is that this occultation had the best resolution of our data set. Since our observed gap dr were power-law distributed and dominated by small gaps, a better resolution would detect smaller and thus more numerous gaps. The most likely explanation for the lack of viewing geometry dependence on our gap detections is a breakdown of the $L = \infty$ approximation in the granola bar model. Simulations show that although self-gravity wakes are generally aligned, they bend and twist before trailing off (Salo et al., 2004). A random cut through such a region could detect the "end-to-end" spacing as well as the minima of the wave and clip some kinks more than once. This scenario is depicted in the right panel of figure 4.10.

As demonstrated by all prior work, on the large scale the viewing angle is the dominant indicator of whether the gaps between the self-gravity wakes are being observed. On this very small scale, however, a myriad of factors determine the likelihood that an individual gap

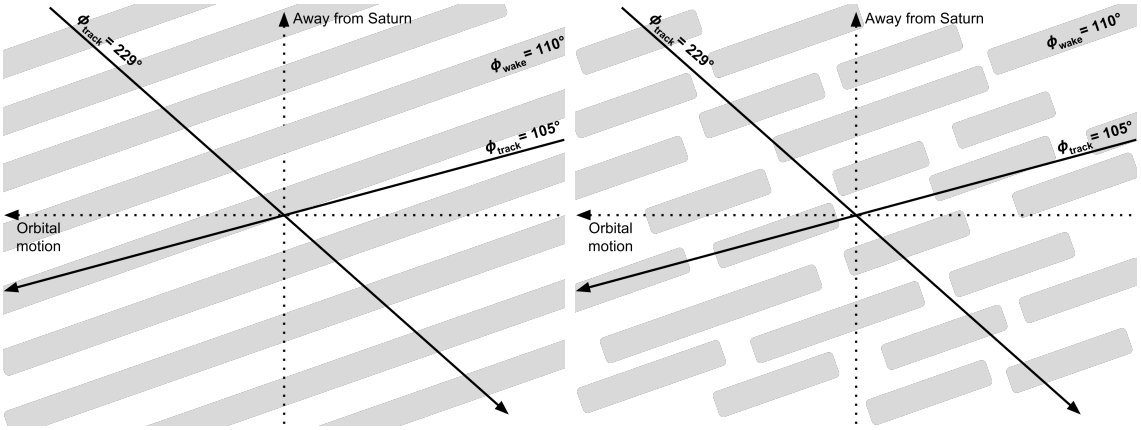

Figure 4.10: Two scenarios for the structure of self-gravity wakes.The left panel depicts the traditional granola bar model, with wakes of infinite length. The right panel depicts a "broken" granola bar model, in which the wakes do not have infinite length. The solid lines represent two possible occultation tracks through the region. In the left scenario, these paths yield dramatically different numbers of detected gaps. In the right, the number of detected gaps is less variable.

will be detected. These include $\phi_{\rm track}$, $\phi_{\rm view}$, B, the signal-to-noise ratio (governed by $I_0\Delta t$), and the resolution. Our data is insufficient to disentangle their individual contributions.

4.5.2 The Janus 4:3 region

The most intriguing result is the strange behavior in the vicinity of the Janus 4:3 resonance. In some observations we detect more gaps than in the surrounding ring and in others we detect fewer (see figure **??**). The occultations that show an excess of gaps also have a steeper gap size distribution than those that do not. Although this phenomenon is most pronounced at the Janus 4:3 resonance, it is also visible at the other strong Lindblad resonances and affects the size distribution across the A ring.

That the Janus 4:3 region would appear different than other resonance regions in not an altogether new observation. French et al. (2007) examined the A-ring brightness asymmetry in *Hubble* imagery and noted that the longitude of minimum brightness shifted from the background in the opposite direction of the Janus 5:4 region.

If the self-gravity wakes are canted at a different angle or angles within the density waves, they would be more readily detectable with a viewing geometry that differs from the viewing geometry that best detects gaps elsewhere in the ring. Hedman et al. (2007c) find that the pitch angle of the wakes changes more dramatically inside of the strong A ring resonances than it does across the rest of the ring at large. Such an observation is consistent with our results here.

4.6 Conclusions

Our search for the minima between the self-gravity wakes has resulted in nearly half a million detected gaps over seven occultations. The size and location of these gaps are consistent with previous indirect observations of the wake structure. We observe an inverse relationship between the number of detected gaps and their size; density waves generally contain fewer but larger gaps than the surrounding ring. These features span the entire A

ring, indicating that self-gravity wake formation is not unique to one region of the A ring.

Although future *Cassini* occultations are unlikely to allow for substantive improvement in our ability to directly detect small-scale gaps in the A ring, the findings here should provide a valuable constraint on modeling efforts.

Now that an m-test based search for small gaps has proven successful in the A ring, we intend to expand it to the rings closer to Saturn. Although self-gravity wakes are less likely in the Cassini Division and C ring, our method should allow for a more robust search for small holes in these regions, which may be indicative of unresolvable embedded objects.

Chapter 5

Conclusions

5.1 Summary of results

5.1.1 A solitary wave at Janus resonances

Saturn's moons Janus and Epimetheus are unique as co-orbital satellites. Every 4.0 years, their resonance brings them within a few degrees of one another, at which point they exchange angular momentum and move radially to swap positions. On 21 Jan 2006, this occurred for the first time during *Cassini's* time at Saturn, with Janus moving closer to Saturn and Epimetheus moving farther away.

When these satellites migrate, their resonances move with them and begin to raise spiral density waves at the new locations. During the Janus-in configuration, the newly-forming wave overlaps for a substantial period of time with the old Epimetheus wave. Because Janus spiral density waves are strongly non-linear, the combination of these waves do not result in a combined wave that is a superposition of the two. Instead, this substantial disruption of the ring forms a solitary wave, which propagates away from Saturn. At Janus resonances in the A ring (Janus 4:3, Janus 5:4, Janus 6:5), the solitary wave propagates at approximately twice the group velocity of the local spiral density wave. At the Janus 2:1 resonance in the B ring, solitary wave propagation speed is commensurate with the group velocity of the local spiral density wave.

When the moons swap such that Epimetheus is closer to Saturn, the same overlapping situation doesn't occur. Thus, we do not see the formation of an additional solitary wave.

Instead, changes propagate outward at the group velocity of the local spiral density wave, which I track at all four resonance locations. In 2014, Janus moved inwards once more and evidence for a solitary wave reappeared.

The presence of a solitary wave could provide evidence for unseen, embedded, massive objects in structures like protoplanetary disks. Popular hypotheses for Solar System formation, like the Nice model, specifically suggest that radial planetary migration is not only possible but likely.

5.1.2 Aggregates in the F ring

Saturn's F ring is among the most dynamic locations in the Solar System. Substantial evidence exists for a population of small objects embedded within this tenuous ring, including from previous investigations using the Ultraviolet Imaging Spectrograph (UVIS). I carried out a reanalysis of previous UVIS stellar occultations and expanded the dataset to include all observations performed through the end of 2016.

A more-carefully-implemented statistical search revealed previously-unseen structures in data used by other studies. These features have radial sizes ranging from tens of meters to kilometers and frequently display optical depths substantially greater than the background ring core. I demonstrate that the population of features found in this expanded dataset are consistent with conclusions about their size-frequency distribution drawn in previous work. Namely, for structures of intermediate size, the distribution is well-described by a power-law with more features of smaller sizes.

However, I dispute previous assumptions about the solidity of these aggregates. I compare integrated optical depths across the F ring core and objects with those of the better-characterized A ring to conclude that these detected features are substantially less dense than previously assumed. Instead of densities on the order 100 kg/m^3, I estimate a mean value of 0.1 kg/m^3. The F ring, on average, is ten times more diffuse than that. These values imply aggregate (4×10^{12} kg) and total F-ring (9.4×10^{14} kg) masses that are much

more consistent with estimates of the overall mass of Saturn's rings. Simple aggregation-fragmentation simulations suggest that a more-diffuse F ring is better able to form the observed population of structures. Binary accretion, however, seems insufficient to account for what I observe.

5.1.3 Small-scale gaps in the rings

Observations dating back to the pre-spaceflight era provide evidence for systematic small-scale structures in the main rings. Numerous *Cassini* observations have provided indirect evidence for the presence of these so-called "self-gravity wakes," quasi-periodic structures with a wavelength of several tens of meters. I conducted the first comprehensive search for these structures in the A and B rings, a task for which the highest-resolution UVIS occultations are ideally suited. In seven of the best observations, I detected nearly half a million gaps which mark the minima of the wakes. Many fewer gaps were visible in the B ring, which is substantially optically-thicker.

The number of observed gaps increases radially outwards over the inner half of the A ring and then decreases more slowly over the outer half. The area covered by these gaps corresponds nearly exactly with the magnitude of the A ring's brightness asymmetry as observed by *Voyager*, indicating that the presence of these gaps is likely to account for variation in the brightness of the rings. One exception to this correlation occurs in the vicinity of the Janus 4:3 resonance, where some observations show an increase in the number of gaps. In general, however, density waves seem to suppress the formation or detection of self-gravity wakes.

Gaps are observed with a lower frequency in the narrow peaks of spiral density waves and are more common in the broad troughs. The general variation of gaps with observing geometry is less consistent with simple models of self-gravity wakes than that observed in lower-resolution surveys. One possible explanation for this is a self-gravity wake structure that is substantially more irregular than the model. Such a structure is broadly supported

by N-body simulations.

5.2 Dynamic rings

From afar, the rings appear both uniform and constant. Such a view was largely supported by observations made by the two *Voyager* spacecraft, each of which performed a stellar and radio occultation of the rings. With relatively poor spatial and temporal resolution, these occultations appeared consistent with steady-state models of the rings. The *Voyager* cameras, however, provided some evidence that the rings were constantly in flux. Observations of so-called "spokes" revealed that the appearance of the main rings could change on a timescale as short as hours. Brightness features in the F ring appeared to be in relative motion on the scales of hours, days, and months.

As seen by *Cassini*, the rings are incredibly dynamic. Daphnis perturbs the edges of the Keeler gap and ripples travel through the C ring. A population of small "propellor" objects migrate through the A ring and the D ring has changed its shape. The dynamism of the F ring hinted at by *Voyager* has been revealed as a complex braided structure full of "fans" and "jets," all of it modified by close encounters with Prometheus.

The results I present here further expand this intricate picture. The Janus-Epimetheus solitary wave demonstrates how critical timing can be in governing ring phenomenon. The difference between the Janus-in configuration and the Janus-out configuration can be distilled down to a few additional months of overlap between an old and new density wave. That difference is enough to create a major propagating feature in the former instance and minor perturbations in the latter.

The time-sensitivity of observations also manifests itself in my study of self-gravity wakes. Prior bulk analyses of the A ring's brightness asymmetry have yielded consistent, repeatable results. The same is only partially true for my detection of individual gaps. The implication seems clear: averaged over large spatial scales, the abundance of self-gravity wakes is relatively common. But, at any given location, the small-scale state of the ring can

be substantially changed at different points in time.

F-ring structures that are more diffuse than previously expected also indicate ephemerality. An object with a density on the order of 100 kg/m^3 is likely semi-permanent, but one three orders of magnitude more diffuse is far less constrained. The dynamic nature of the F ring could form and disperse such tenuous structures over short timescales.

5.3 Applications

The direct parallels for this work elsewhere in the Solar System are not extensive. Saturn's main rings are substantially more massive than those known to orbit other bodies. Their icy nature also differentiates them from what we know about the Jovian, Uranian, and Neptunian ring systems. Saturn's diffuse rings, of which the F ring is the densest and most well-studied, may prove more valuable for comparison.

The F ring can also shed light on the accretion processes that shaped our early Solar System. Many of the regular satellites of Saturn have densities on the order of that of ice, indicating that they may have accreted, at least in part, out of nearly-pure ring material (e.g., Porco et al. (2007)). These moons depleted the mass available for new object formation in the present-day rings, but the processes by which they formed are still operating today. On a larger scale, accretion processes led to the formation of the planets themselves. While Saturn's rings, lacking both gas and influence from a strong magnetic field, may be a limited comparison to a protoplanetary disk, they still offer an opportunity to observe actual accretion in an astrophysical disk.

Perhaps the most promising application of my results lies in the detection of a solitary wave resulting from the radial motion of a massive body. The discovery of hot Jupiters and the adoption of planet-formation hypotheses like the Nice model have suggested that radial migration of massive planets is not uncommon. Spiral density waves have already been detected in multiple protoplanetary systems (Muto et al., 2012; Pérez et al., 2016). Where there are density waves, there is the possibility of a solitary wave similar in form to the ones

I have described here. Small radial motions, undetectable by our current technology, could yield an observable phenomenon that would allow the identification of migrating bodies.

5.4 Looking to the future

The work detailed here is only the beginning for understanding the small-scale structure of the rings. The solitary wave in particular highlights a number of needs and opportunities for further work. Although the theoretical basis for solitary waves has already been explored for (unforced) galactic density waves (Vukcevic, 2014), no such theory exists for the forced, planetary rings case. Once a theoretical framework for the waves are developed, their velocity and size may be able to provide an independent estimate for the surface-mass density of the regions through which they propagate. This would be of great value because currently analyses of spiral density waves represent the only means of making such estimates.

In the interim, it may be possible to detect changes in the local surface-mass density by charting changes in the solitary wave's speed. One possible way to accomplish that would be to compare the residuals from a best-fit velocity at different times along the wave's path. Biases may indicate short-term changes in propagation velocity.

The F ring needs an expansion of simulations capable of modeling the accretion and destruction of tenuous structures. My work has demonstrated that previous conceptions as to the solidity of these "objects" were misleading. Things that are relatively dense can be modeled effectively with our current generation of N-body simulations, but tenuous objects require a larger range of particle sizes to be considered.

Expanding the study of individual gaps between the maxima of self-gravity wakes probably requires one thing we are unlikely to get: substantially more data. In more than 170 available occultations, only 7 met the criteria I outlined in chapter 4 for inclusion in the study. Carefully-designed "tracking occultations" provided the best data with which to search for gaps and these observations can only occur in certain situations. With the conclusion of *Cassini* in September 2017, it may be decades before comparable datasets are

acquired. No data collected from ground- or space-based telescopes will be sufficient.

When another mission does arrive at Saturn, a different kind of observing program would provide the means necessary for expanding the study of small-scale structure. *Cassini* data has provided an extraordinary overview of ring phenomena across many scales, locations, and timespans far beyond what *Voyager* and *Pioneer 11* could, but, in light of a new understanding of the dynamism of the rings, there are clear deficiencies for more detailed work.

The varied nature of UVIS occultations means that there are few instances of repeat observation of the same element of ring material. Many images taken by *Cassini* cameras serve this purpose, but at a resolution far too poor for the study of self-gravity wakes or tenuous F-ring structures. A series of repeat observations spanning just hours or days, while technically-challenging, would provide tremendous information about how the ring evolves on short timescales. Keplerian shear means that locations a kilometer apart would experience substantial relative motion on the order of days. How does this change the structure of a self-gravity wake? Detailed observations could help us find out.

Bibliography

N. Albers, M. Sremčević, J. E. Colwell, and L. W. Esposito. Saturn's F ring as seen by Cassini UVIS: Kinematics and statistics. Icarus, 217:367–388, January 2012. doi: 10.1016/j.icarus.2011.11.016.

N. O. Attree, C. D. Murray, N. J. Cooper, and G. A. Williams. Detection of Low-velocity Collisions in Saturn's F Ring. ApJ, 755:L27, August 2012. doi: 10.1088/2041-8205/755/2/L27.

K. Baillié, J. E. Colwell, J. J. Lissauer, L. W. Esposito, and M. Sremčević. Waves in Cassini UVIS stellar occultations. 2. The C ring. Icarus, 216:292–308, November 2011. doi: 10.1016/j.icarus.2011.05.019.

J. M. Barbara and L. W. Esposito. Moonlet Collisions and the Effects of Tidally Modified Accretion in Saturn's F Ring. Icarus, 160:161–171, November 2002. doi: 10.1006/icar.2002.6962.

W. A. Baum, T. Kreidl, J. A. Westphal, G. E. Danielson, P. K. Seidelmann, D. Pascu, and D. G. Currie. Saturn's E ring. Icarus, 47:84–96, July 1981. doi: 10.1016/0019-1035(81)90093-2.

T. M. Becker, J. E. Colwell, L. W. Esposito, and A. D. Bratcher. Characterizing the particle size distribution of Saturn's A ring with Cassini UVIS occultation data. Icarus, 279:20–35, November 2016. doi: 10.1016/j.icarus.2015.11.001.

K. Beurle, C. D. Murray, G. A. Williams, M. W. Evans, N. J. Cooper, and C. B. Agnor. Direct Evidence for Gravitational Instability and Moonlet Formation in Saturn's Rings. ApJ, 718:L176–L180, August 2010. doi: 10.1088/2041-8205/718/2/L176.

A. S. Bosh and A. S. Rivkin. Observations of Saturn's Inner Satellites During the May 1995 Ring-Plane Crossing. Science, 272:518–521, April 1996. doi: 10.1126/science.272.5261.518.

A. S. Bosh, C. B. Olkin, R. G. French, and P. D. Nicholson. Saturn's F Ring: Kinematics and Particle Sizes from Stellar Occultation Studies. Icarus, 157:57–75, May 2002. doi: 10.1006/icar.2002.6791.

F. Braga-Ribas, B. Sicardy, J. L. Ortiz, C. Snodgrass, F. Roques, R. Vieira-Martins, J. I. B. Camargo, M. Assafin, R. Duffard, E. Jehin, J. Pollock, R. Leiva, M. Emilio, D. I. Machado, C. Colazo, E. Lellouch, J. Skottfelt, M. Gillon, N. Ligier, L. Maquet, G. Benedetti-Rossi, A. R. Gomes, P. Kervella, H. Monteiro, R. Sfair, M. El Moutamid, G. Tancredi, J. Spagnotto, A. Maury, N. Morales, R. Gil-Hutton, S. Roland, A. Ceretta, S.-H. Gu, X.-B. Wang, K. Harpsøe, M. Rabus, J. Manfroid, C. Opitom, L. Vanzi, L. Mehret, L. Lorenzini, E. M. Schneiter, R. Melia, J. Lecacheux, F. Colas, F. Vachier, T. Widemann, L. Almenares, R. G. Sandness, F. Char, V. Perez, P. Lemos, N. Martinez, U. G. Jørgensen, M. Dominik, F. Roig, D. E. Reichart, A. P. Lacluyze, J. B. Haislip, K. M. Ivarsen, J. P. Moore, N. R. Frank, and D. G. Lambas. A ring system detected around the Centaur (10199) Chariklo. Nature, 508:72–75, April 2014. doi: 10.1038/nature13155.

J. A. Burns, M. R. Showalter, D. P. Hamilton, P. D. Nicholson, I. de Pater, M. E. Ockert-Bell, and P. C. Thomas. The Formation of Jupiter's Faint Rings. Science, 284:1146, May 1999. doi: 10.1126/science.284.5417.1146.

R. M. Canup. Origin of Saturn's rings and inner moons by mass removal from a lost Titan-sized satellite. Nature, 468:943–946, December 2010. doi: 10.1038/nature09661.

R. M. Canup and L. W. Esposito. Accretion in the Roche zone: Coexistence of rings and ring moons. Icarus, 113:331–352, February 1995. doi: 10.1006/icar.1995.1026.

R. O. Chancia and M. M. Hedman. Are There Moonlets Near the Uranian α and β Rings? AJ, 152:211, December 2016. doi: 10.3847/0004-6256/152/6/211.

S. Charnoz, A. Morbidelli, L. Dones, and J. Salmon. Did Saturn's rings form during the Late Heavy Bombardment? Icarus, 199:413–428, February 2009. doi: 10.1016/j.icarus.2008.10.019.

D. H. Cohen, M. A. Kuhn, M. Gagné, E. L. N. Jensen, and N. A. Miller. Chandra spectroscopy of the hot star βCrucis and the discovery of a pre-main-sequence companion. MNRAS, 386:1855–1871, June 2008. doi: 10.1111/j.1365-2966.2008.13176.x.

G. Colombo, P. Goldreich, and A. W. Harris. Spiral structure as an explanation for the asymmetric brightness of Saturn's A ring. Nature, 264:344, November 1976. doi: 10.1038/264344a0.

J. E. Colwell and L. W. Esposito. Origins of the rings of Uranus and Neptune. I - Statistics of satellite disruptions. J. Geophys. Res., 97:10, June 1992. doi: 10.1029/92JE00788.

J. E. Colwell, L. J. Horn, A. L. Lane, L. W. Esposito, P. A. Yanamandra-Fisher, S. H. Pilorz, K. E. Simmons, M. D. Morrison, C. W. Hord, R. M. Nelson, B. D. Wallis, R. A. West, and B. J. Buratti. Voyager photopolarimeter observations of Uranian ring occultations. Icarus, 83:102–125, January 1990. doi: 10.1016/0019-1035(90)90009-X.

J. E. Colwell, L. W. Esposito, and M. Sremčević. Self-gravity wakes in Saturn's A ring measured by stellar occultations from Cassini. Geophys. Res. Lett., 33:L07201, April 2006. doi: 10.1029/2005GL025163.

J. E. Colwell, L. W. Esposito, M. Sremčević, G. R. Stewart, and W. E. McClintock. Self-gravity wakes and radial structure of Saturn's B ring. Icarus, 190:127–144, September 2007. doi: 10.1016/j.icarus.2007.03.018.

J. E. Colwell, P. D. Nicholson, M. S. Tiscareno, C. D. Murray, R. G. French, and E. A. Marouf. The Structure of Saturn's Rings. 2009. doi: 10.1007/978-1-4020-9217-6_13.

J. E. Colwell, L. W. Esposito, R. G. Jerousek, M. Sremčević, D. Pettis, and E. T. Bradley. Cassini UVIS Stellar Occultation Observations of Saturn's Rings. AJ, 140:1569–1578, December 2010. doi: 10.1088/0004-6256/140/6/1569.

J. N. Cuzzi and J. A. Burns. Charged particle depletion surrounding Saturn's F ring - Evidence for a moonlet belt? Icarus, 74:284–324, May 1988. doi: 10.1016/0019-1035(88)90043-7.

I. de Pater, S. G. Gibbard, E. Chiang, H. B. Hammel, B. Macintosh, F. Marchis, S. C. Martin, H. G. Roe, and M. Showalter. The dynamic neptunian ring arcs: evidence for a gradual disappearance of Liberté and resonant jump of courage. Icarus, 174:263–272, March 2005. doi: 10.1016/j.icarus.2004.10.020.

S. F. Dermott and C. D. Murray. The dynamics of tadpole and horseshoe orbits II. The coorbital satellites of saturn. Icarus, 48:12–22, October 1981. doi: 10.1016/0019-1035(81)90148-2.

L. Dones. A recent cometary origin for Saturn's rings? Icarus, 92:194–203, August 1991. doi: 10.1016/0019-1035(91)90045-U.

L. Dones, J. N. Cuzzi, and M. R. Showalter. Voyager Photometry of Saturn's A Ring. Icarus, 105:184–215, September 1993. doi: 10.1006/icar.1993.1118.

M. K. Dougherty, L. W. Esposito, and S. M. Krimigis. Saturn from Cassini-Huygens. 2009. doi: 10.1007/978-1-4020-9217-6.

L. R. Doyle, L. Dones, and J. N. Cuzzi. Radiative transfer modeling of Saturn's outer B ring. Icarus, 80:104–135, July 1989. doi: 10.1016/0019-1035(89)90163-2.

C. Dumas, R. J. Terrile, B. A. Smith, G. Schneider, and E. E. Becklin. Stability of Neptune's ring arcs in question. Nature, 400:733–735, August 1999. doi: 10.1038/23414.

M. El Moutamid, P. D. Nicholson, R. G. French, M. S. Tiscareno, C. D. Murray, M. W. Evans, C. McGhee French, M. M. Hedman, and J. A. Burns. How Janus' Orbital Swap Affects the Edge of Saturn's A Ring? Icarus, in press, 2016.

L. W. Esposito. Planetary Rings. July 2006.

L. W. Esposito, M. Ocallaghan, and R. A. West. The structure of Saturn's rings - Implications from the Voyager stellar occultation. Icarus, 56:439–452, December 1983. doi: 10.1016/0019-1035(83)90165-3.

L. W. Esposito, C. A. Barth, J. E. Colwell, G. M. Lawrence, W. E. McClintock, A. I. F. Stewart, H. U. Keller, A. Korth, H. Lauche, M. C. Festou, A. L. Lane, C. J. Hansen, J. N. Maki, R. A. West, H. Jahn, R. Reulke, K. Warlich, D. E. Shemansky, and Y. L. Yung. The Cassini Ultraviolet Imaging Spectrograph Investigation. Space Sci. Rev., 115: 299–361, December 2004. doi: 10.1007/s11214-004-1455-8.

L. W. Esposito, B. K. Meinke, J. E. Colwell, P. D. Nicholson, and M. M. Hedman. Moonlets and clumps in Saturn's F ring. Icarus, 194:278–289, March 2008. doi: 10.1016/j.icarus.2007.10.001.

L. W. Esposito, N. Albers, B. K. Meinke, M. Sremčević, P. Madhusudhanan, J. E. Colwell, and R. G. Jerousek. A predator-prey model for moon-triggered clumping in Saturn's rings. Icarus, 217:103–114, January 2012. doi: 10.1016/j.icarus.2011.09.029.

C. Ferrari, S. Brooks, S. Edgington, C. Leyrat, S. Pilorz, and L. Spilker. Structure of self-gravity wakes in Saturn's A ring as measured by Cassini CIRS. Icarus, 199:145–153, January 2009. doi: 10.1016/j.icarus.2008.09.001.

I. Ferrin. On the structure of Saturn's rings and the 'real' rotational period for the planet. Ap&SS, 33:453–457, April 1975. doi: 10.1007/BF00640110.

G. Filacchione, F. Capaccioni, M. Ciarniello, R. N. Clark, J. N. Cuzzi, P. D. Nicholson, D. P. Cruikshank, M. M. Hedman, B. J. Buratti, J. I. Lunine, L. A. Soderblom, F. Tosi, P. Cerroni, R. H. Brown, T. B. McCord, R. Jaumann, K. Stephan, K. H. Baines, and E. Flamini. Saturn's icy satellites and rings investigated by Cassini-VIMS: III - Radial compositional variability. Icarus, 220:1064–1096, August 2012. doi: 10.1016/j.icarus.2012.06.040.

E. L. Fitzpatrick and D. Massa. Determining the Physical Properties of the B Stars. II. Calibration of Synthetic Photometry. AJ, 129:1642–1662, March 2005. doi: 10.1086/427855.

F. A. Franklin and G. Colombo. On the azimuthal brightness variations of Saturn's rings. Icarus, 33:279–287, February 1978. doi: 10.1016/0019-1035(78)90147-1.

R. G. French and P. D. Nicholson. Saturn's Rings II. Particle Sizes Inferred from Stellar Occultation Data. Icarus, 145:502–523, June 2000. doi: 10.1006/icar.2000.6357.

R. G. French, P. D. Nicholson, M. L. Cooke, J. L. Elliot, K. Matthews, O. Perkovic, E. Tollestrup, P. Harvey, N. J. Chanover, M. A. Clark, E. W. Dunham, W. Forrest, J. Harrington, J. Pipher, A. Brahic, I. Grenier, F. Roques, and M. Arndt. Geometry of the Saturn system from the 3 July 1989 occultation of 28 SGR and Voyager observations. Icarus, 103:163–214, June 1993. doi: 10.1006/icar.1993.1066.

R. G. French, H. Salo, C. A. McGhee, and L. Dones. HST observations of azimuthal asymmetry in Saturn's rings. Icarus, 189:493–522, August 2007. doi: 10.1016/j.icarus.2007.02.019.

P. Goldreich and S. Tremaine. The dynamics of planetary rings. ARA&A, 20:249–283, 1982. doi: 10.1146/annurev.aa.20.090182.001341.

P. Goldreich, S. Tremaine, and N. Borderies. Towards a theory for Neptune's arc rings. AJ, 92:490–494, August 1986. doi: 10.1086/114178.

P. K. Haff, G. L. Siscoe, and A. Eviatar. Ring and plasma - The enigmae of Enceladus. Icarus, 56:426–438, December 1983. doi: 10.1016/0019-1035(83)90164-1.

J. L. Hammack and H. Segur. The Korteweg-de Vries equation and water waves. Part 2. Comparison with experiments. Journal of Fluid Mechanics, 65:289–314, 1974. doi: 10.1017/S002211207400139X.

C. J. Hansen, L. Esposito, A. I. F. Stewart, J. Colwell, A. Hendrix, W. Pryor, D. Shemansky, and R. West. Enceladus' Water Vapor Plume. Science, 311:1422–1425, March 2006. doi: 10.1126/science.1121254.

D. Harrington, G. Koenigsberger, E. Moreno, and J. Kuhn. Line-profile Variability from Tidal Flows in Alpha Virginis (Spica). ApJ, 704:813–830, October 2009. doi: 10.1088/0004-637X/704/1/813.

M. M. Hedman. Why Are Dense Planetary Rings Only Found between 8 AU and 20 AU? ApJ, 801:L33, March 2015. doi: 10.1088/2041-8205/801/2/L33.

M. M. Hedman and P. D. Nicholson. Kronoseismology: Using Density Waves in Saturn's C Ring to Probe the Planet's Interior. AJ, 146:12, July 2013. doi: 10.1088/0004-6256/146/1/12.

M. M. Hedman and P. D. Nicholson. More Kronoseismology with Saturn's rings. MNRAS, 444:1369–1388, October 2014. doi: 10.1093/mnras/stu1503.

M. M. Hedman and P. D. Nicholson. The B-ring's surface mass density from hidden density waves: Less than meets the eye? Icarus, in press, 2016.

M. M. Hedman, J. A. Burns, M. R. Showalter, C. C. Porco, P. D. Nicholson, A. S. Bosh, M. S. Tiscareno, R. H. Brown, B. J. Buratti, K. H. Baines, and R. Clark. Saturn's dynamic D ring. Icarus, 188:89–107, May 2007a. doi: 10.1016/j.icarus.2006.11.017.

M. M. Hedman, J. A. Burns, M. S. Tiscareno, C. C. Porco, G. H. Jones, E. Roussos, N. Krupp, C. Paranicas, and S. Kempf. The Source of Saturn's G Ring. Science, 317:653–, August 2007b. doi: 10.1126/science.1143964.

M. M. Hedman, P. D. Nicholson, H. Salo, B. D. Wallis, B. J. Buratti, K. H. Baines, R. H. Brown, and R. N. Clark. Self-Gravity Wake Structures in Saturn's A Ring Revealed by Cassini VIMS. AJ, 133:2624–2629, June 2007c. doi: 10.1086/516828.

M. M. Hedman, P. D. Nicholson, M. R. Showalter, R. H. Brown, B. J. Buratti, R. N. Clark, K. Baines, and C. Sotin. The Christiansen Effect in Saturn's narrow dusty rings and the spectral identification of clumps in the F ring. Icarus, 215:695–711, October 2011. doi: 10.1016/j.icarus.2011.02.025.

M. M. Hohle, R. Neuhäuser, and B. F. Schutz. Masses and luminosities of O- and B-type stars and red supergiants. Astronomische Nachrichten, 331:349, April 2010. doi: 10.1002/asna.200911355.

L. J. Horn, J. Hui, A. L. Lane, and J. E. Colwell. Observations of Neptunian rings by Voyager Photopolarimeter Experiment. Geophys. Res. Lett., 17:1745–1748, September 1990. doi: 10.1029/GL017i010p01745.

L. J. Horn, M. R. Showalter, and C. T. Russell. Detection and Behavior of Pan Wakes in Saturn's A Ring. Icarus, 124:663–676, December 1996. doi: 10.1006/icar.1996.0240.

R. A. Jacobson, P. G. Antreasian, J. J. Bordi, K. E. Criddle, R. Ionasescu, J. B. Jones, R. A. Mackenzie, M. C. Meek, D. Parcher, F. J. Pelletier, W. M. Owen, Jr., D. C. Roth, I. M. Roundhill, and J. R. Stauch. The Gravity Field of the Saturnian System from Satellite Observations and Spacecraft Tracking Data. AJ, 132:2520–2526, December 2006. doi: 10.1086/508812.

R. A. Jacobson, J. Spitale, C. C. Porco, K. Beurle, N. J. Cooper, M. W. Evans, and C. D. Murray. Revised Orbits of Saturn's Small Inner Satellites. AJ, 135:261–263, January 2008. doi: 10.1088/0004-6256/135/1/261.

R. G. Jerousek, J. E. Colwell, L. W. Esposito, P. D. Nicholson, and M. M. Hedman. Small particles and self-gravity wakes in saturn's rings from uvis and vims stellar occultations. Icarus, 279:36 – 50, November 2016. ISSN 0019-1035. doi: 10.1016/j.icarus.2016.04.039. Planetary Rings.

M. A. Kenworthy, S. Lacour, A. Kraus, A. H. M. J. Triaud, E. E. Mamajek, E. L. Scott, D. Ségransan, M. Ireland, F.-J. Hambsch, D. E. Reichart, J. B. Haislip, A. P. LaCluyze, J. P. Moore, and N. R. Frank. Mass and period limits on the ringed companion transiting the young star J1407. MNRAS, 446:411–427, January 2015. doi: 10.1093/mnras/stu2067.

C. C. Lin and F. H. Shu. On the Spiral Structure of Disk Galaxies. ApJ, 140:646, August 1964. doi: 10.1086/147955.

J. J. Lissauer. Bending waves and the structure of Saturn's rings. Icarus, 62:433–447, June 1985. doi: 10.1016/0019-1035(85)90186-1.

J. J. Lissauer and J. N. Cuzzi. Resonances in Saturn's rings. AJ, 87:1051–1058, July 1982. doi: 10.1086/113189.

K. Lumme, L. W. Esposito, W. M. Irvine, and W. A. Baum. Azimuthal brightness variations of Saturn's rings. II - Observations at an intermediate tilt angle. ApJ, 216:L123–L126, September 1977. doi: 10.1086/182525.

E. E. Mamajek, A. C. Quillen, M. J. Pecaut, F. Moolekamp, E. L. Scott, M. A. Kenworthy, A. Collier Cameron, and N. R. Parley. Planetary Construction Zones in Occultation: Discovery of an Extrasolar Ring System Transiting a Young Sun-like Star and Future Prospects for Detecting Eclipses by Circumsecondary and Circumplanetary Disks. AJ, 143:72, March 2012. doi: 10.1088/0004-6256/143/3/72.

C. A. McGhee, P. D. Nicholson, R. G. French, and K. J. Hall. HST Observations of Saturnian Satellites during the 1995 Ring Plane Crossings. Icarus, 152:282–315, August 2001. doi: 10.1006/icar.2001.6635.

B. K. Meinke. Observations and Models of Accretion in Saturn's F ring. PhD thesis, University of Colorado, 2012.

B. K. Meinke, L. W. Esposito, N. Albers, and M. Sremčević. Classification of F ring features observed in Cassini UVIS occultations. Icarus, 218:545–554, March 2012. doi: 10.1016/j.icarus.2011.12.020.

C. D. Murray and S. F. Dermott. Solar system dynamics. 1999.

C. D. Murray, C. Chavez, K. Beurle, N. Cooper, M. W. Evans, J. A. Burns, and C. C. Porco. How Prometheus creates structure in Saturn's F ring. Nature, 437:1326–1329, October 2005. doi: 10.1038/nature04212.

C. D. Murray, K. Beurle, N. J. Cooper, M. W. Evans, G. A. Williams, and S. Charnoz. The determination of the structure of Saturn's F ring by nearby moonlets. Nature, 453:739–744, June 2008. doi: 10.1038/nature06999.

T. Muto, C. A. Grady, J. Hashimoto, M. Fukagawa, J. B. Hornbeck, M. Sitko, R. Russell, C. Werren, M. Curé, T. Currie, N. Ohashi, Y. Okamoto, M. Momose, M. Honda, S. Inutsuka, T. Takeuchi, R. Dong, L. Abe, W. Brandner, T. Brandt, J. Carson, S. Egner, M. Feldt, T. Fukue, M. Goto, O. Guyon, Y. Hayano, M. Hayashi, S. Hayashi, T. Henning, K. W. Hodapp, M. Ishii, M. Iye, M. Janson, R. Kandori, G. R. Knapp, T. Kudo, N. Kusakabe, M. Kuzuhara, T. Matsuo, S. Mayama, M. W. McElwain, S. Miyama, J.-I. Morino, A. Moro-Martin, T. Nishimura, T.-S. Pyo, E. Serabyn, H. Suto, R. Suzuki, M. Takami, N. Takato, H. Terada, C. Thalmann, D. Tomono, E. L. Turner, M. Watanabe, J. P. Wisniewski, T. Yamada, H. Takami, T. Usuda, and M. Tamura. Discovery of Small-scale Spiral Structures in the Disk of SAO 206462 (HD 135344B): Implications for the Physical State of the Disk from Spiral Density Wave Theory. ApJ, 748:L22, April 2012. doi: 10.1088/2041-8205/748/2/L22.

F. Namouni and C. Porco. The confinement of Neptune's ring arcs by the moon Galatea. Nature, 417:45–47, May 2002. doi: 10.1038/417045a.

P. D. Nicholson, D. P. Hamilton, K. Matthews, and C. F. Yoder. New observations of Saturn's coorbital satellites. Icarus, 100:464–484, December 1992. doi: 10.1016/0019-1035(92)90111-J.

P. D. Nicholson, M. M. Hedman, R. N. Clark, M. R. Showalter, D. P. Cruikshank, J. N. Cuzzi, G. Filacchione, F. Capaccioni, P. Cerroni, G. B. Hansen, B. Sicardy, P. Drossart, R. H. Brown, B. J. Buratti, K. H. Baines, and A. Coradini. A close look at Saturn's rings with Cassini VIMS. Icarus, 193:182–212, January 2008. doi: 10.1016/j.icarus.2007.08.036.

C. A. Norman. A non-linear theory of spiral density waves. MNRAS, 182:457–472, February 1978.

M. E. Ockert-Bell, J. A. Burns, I. J. Daubar, P. C. Thomas, J. Veverka, M. J. S. Belton, and K. P. Klaasen. The Structure of Jupiter's Ring System as Revealed by the Galileo Imaging Experiment. Icarus, 138:188–213, April 1999. doi: 10.1006/icar.1998.6072.

L. M. Pérez, J. M. Carpenter, S. M. Andrews, L. Ricci, A. Isella, H. Linz, A. I. Sargent, D. J. Wilner, T. Henning, A. T. Deller, C. J. Chandler, C. P. Dullemond, J. Lazio, K. M. Menten, S. A. Corder, S. Storm, L. Testi, M. Tazzari, W. Kwon, N. Calvet, J. S. Greaves, R. J. Harris, and L. G. Mundy. Spiral density waves in a young protoplanetary disk. Science, 353:1519–1521, September 2016. doi: 10.1126/science.aaf8296.

C. C. Porco. An explanation for Neptune's ring arcs. Science, 253:995–1001, August 1991. doi: 10.1126/science.253.5023.995.

C. C. Porco, E. Baker, J. Barbara, K. Beurle, A. Brahic, J. A. Burns, S. Charnoz, N. Cooper, D. D. Dawson, A. D. Del Genio, T. Denk, L. Dones, U. Dyudina, M. W. Evans, B. Giese, K. Grazier, P. Helfenstein, A. P. Ingersoll, R. A. Jacobson, T. V. Johnson, A. McEwen, C. D. Murray, G. Neukum, W. M. Owen, J. Perry, T. Roatsch, J. Spitale, S. Squyres, P. Thomas, M. Tiscareno, E. Turtle, A. R. Vasavada, J. Veverka, R. Wagner, and R. West. Cassini Imaging Science: Initial Results on Saturn's Rings and Small Satellites. Science, 307:1226–1236, February 2005. doi: 10.1126/science.1108056.

C. C. Porco, P. Helfenstein, P. C. Thomas, A. P. Ingersoll, J. Wisdom, R. West, G. Neukum, T. Denk, R. Wagner, T. Roatsch, S. Kieffer, E. Turtle, A. McEwen, T. V. Johnson, J. Rathbun, J. Veverka, D. Wilson, J. Perry, J. Spitale, A. Brahic, J. A. Burns, A. D. Del Genio, L. Dones, C. D. Murray, and S. Squyres. Cassini Observes the Active South Pole of Enceladus. Science, 311:1393–1401, March 2006. doi: 10.1126/science.1123013.

C. C. Porco, P. C. Thomas, J. W. Weiss, and D. C. Richardson. Saturn's small inner satellites: Clues to their origins. Science, 318:1602, December 2007. doi: 10.1126/science.1143977.

M. J. Price and A. Baker. Illumination of Saturn's ring by the ball. I - Preliminary results. Icarus, 25:136–145, May 1975. doi: 10.1016/0019-1035(75)90193-1.

E. Reffet, M. Verdier, and C. Ferrari. Thickness of Saturn's B ring as derived from seasonal temperature variations measured by Cassini CIRS. Icarus, 254:276–286, July 2015. doi: 10.1016/j.icarus.2015.04.006.

Morgan E. Rehnberg, Larry W. Esposito, Zarah L. Brown, Nicole Albers, Miodrag Sremčević, and Glen R. Stewart. A traveling feature in saturn's rings. Icarus, 279:100 – 108, November

2016. ISSN 0019-1035. doi: http://dx.doi.org/10.1016/j.icarus.2016.06.012. URL http://www.sciencedirect.com/science/article/pii/S0019103516302901. Planetary Rings.

S. J. Robbins, G. R. Stewart, M. C. Lewis, J. E. Colwell, and M. Sremčević. Estimating the masses of Saturn's A and B rings from high-optical depth N-body simulations and stellar occultations. Icarus, 206:431–445, April 2010. doi: 10.1016/j.icarus.2009.09.012.

J. Salmon, S. Charnoz, A. Crida, and A. Brahic. Long-term and large-scale viscous evolution of dense planetary rings. Icarus, 209:771–785, October 2010. doi: 10.1016/j.icarus.2010.05.030.

H. Salo. Simulations of dense planetary rings. III. Self-gravitating identical particles. Icarus, 117:287–312, October 1995. doi: 10.1006/icar.1995.1157.

H. Salo, R. Karjalainen, and R. G. French. Photometric modeling of Saturn's rings. II. Azimuthal asymmetry in reflected and transmitted light. Icarus, 170:70–90, July 2004. doi: 10.1016/j.icarus.2004.03.012.

B. R. Scharringhausen and P. D. Nicholson. The vertical structure of the F ring of Saturn from ring-plane crossings. Icarus, 226:1275–1293, November 2013. doi: 10.1016/j.icarus.2013.08.010.

P. K. Seidelmann, B. A. Archinal, M. F. A'Hearn, A. Conrad, G. J. Consolmagno, D. Hestroffer, J. L. Hilton, G. A. Krasinsky, G. Neumann, J. Oberst, P. Stooke, E. F. Tedesco, D. J. Tholen, P. C. Thomas, and I. P. Williams. Report of the IAU/IAG Working Group on cartographic coordinates and rotational elements: 2006. Celestial Mechanics and Dynamical Astronomy, 98:155–180, July 2007. doi: 10.1007/s10569-007-9072-y.

M. R. Showalter. Disentangling Saturn's F Ring. I. Clump orbits and lifetimes. Icarus, 171:356–371, October 2004. doi: 10.1016/j.icarus.2004.05.006.

F. H. Shu. Waves in planetary rings. In R. Greenberg and A. Brahic, editors, IAU Colloq. 75: Planetary Rings, pages 513–561, 1984.

F. H. Shu. Six Decades of Spiral Density Wave Theory. ARA&A, 54:667–724, September 2016. doi: 10.1146/annurev-astro-081915-023426.

F. H. Shu, J. N. Cuzzi, and J. J. Lissauer. Bending waves in Saturn's rings. Icarus, 53:185–206, February 1983. doi: 10.1016/0019-1035(83)90141-0.

B. Sicardy, F. Roddier, C. Roddier, E. Perozzi, J. E. Graves, O. Guyon, and M. J. Northcott. Images of Neptune's ring arcs obtained by a ground-based telescope. Nature, 400:731–733, August 1999. doi: 10.1038/23410.

J. Silk and T. Takahashi. A statistical model for the initial stellar mass function. ApJ, 229:242–256, April 1979. doi: 10.1086/156949.

B. A. Smith, L. A. Soderblom, R. Beebe, D. Bliss, R. H. Brown, S. A. Collins, J. M. Boyce, G. A. Briggs, A. Brahic, J. N. Cuzzi, and D. Morrison. Voyager 2 in the Uranian system - Imaging science results. Science, 233:43–64, July 1986. doi: 10.1126/science.233.4759.43.

B. A. Smith, L. A. Soderblom, D. Banfield, C. Barnet, A. T. Basilevksy, R. F. Beebe, K. Bollinger, J. M. Boyce, A. Brahic, G. A. Briggs, R. H. Brown, C. Chyba, S. A. Collins, T. Colvin, A. F. Cook, D. Crisp, S. K. Croft, D. Cruikshank, J. N. Cuzzi, G. E. Danielson, M. E. Davies, E. de Jong, L. Dones, D. Godfrey, J. Goguen, I. Grenier, V. R. Haemmerle, H. Hammel, C. J. Hansen, C. P. Helfenstein, C. Howell, G. E. Hunt, A. P. Ingersoll, T. V. Johnson, J. Kargel, R. Kirk, D. I. Kuehn, S. Limaye, H. Masursky, A. McEwen, D. Morrison, T. Owen, W. Owen, J. B. Pollack, C. C. Porco, K. Rages, P. Rogers, D. Rudy, C. Sagan, J. Schwartz, E. M. Shoemaker, M. Showalter, B. Sicardy, D. Simonelli, J. Spencer, L. A. Sromovsky, C. Stoker, R. G. Strom, V. E. Suomi, S. P. Synott, R. J. Terrile, P. Thomas, W. R. Thompson, A. Verbiscer, and J. Veverka. Voyager 2 at Neptune: Imaging Science Results. Science, 246:1422–1449, December 1989. doi: 10.1126/science.246.4936.1422.

J. N. Spitale and C. C. Porco. Association of the jets of Enceladus with the warmest regions on its south-polar fractures. Nature, 449:695–697, October 2007. doi: 10.1038/nature06217.

J. N. Spitale, R. A. Jacobson, C. C. Porco, and W. M. Owen, Jr. The Orbits of Saturn's Small Satellites Derived from Combined Historic and Cassini Imaging Observations. AJ, 132:692–710, August 2006. doi: 10.1086/505206.

M. Sremčević, J. Schmidt, H. Salo, M. Seiß, F. Spahn, and N. Albers. A belt of moonlets in Saturn's A ring. Nature, 449:1019–1021, October 2007. doi: 10.1038/nature06224.

H. Tanaka, S. Inaba, and K. Nakazawa. Steady-State Size Distribution for the Self-Similar Collision Cascade. Icarus, 123:450–455, October 1996. doi: 10.1006/icar.1996.0170.

P. C. Thomas. Sizes, shapes, and derived properties of the saturnian satellites after the Cassini nominal mission. Icarus, 208:395–401, July 2010. doi: 10.1016/j.icarus.2010.01.025.

P. C. Thomas, R. Tajeddine, M. S. Tiscareno, J. A. Burns, J. Joseph, T. J. Loredo, P. Helfenstein, and C. Porco. Enceladus's measured physical libration requires a global subsurface ocean. Icarus, 264:37–47, January 2016. doi: 10.1016/j.icarus.2015.08.037.

H. B. Throop, C. C. Porco, R. A. West, J. A. Burns, M. R. Showalter, and P. D. Nicholson. The jovian rings: new results derived from Cassini, Galileo, Voyager, and Earth-based observations. Icarus, 172:59–77, November 2004. doi: 10.1016/j.icarus.2003.12.020.

M. S. Tiscareno, J. A. Burns, M. M. Hedman, C. C. Porco, J. W. Weiss, L. Dones, D. C. Richardson, and C. D. Murray. 100-metre-diameter moonlets in Saturn's A ring from observations of 'propeller' structures. Nature, 440:648–650, March 2006a. doi: 10.1038/nature04581.

M. S. Tiscareno, P. D. Nicholson, J. A. Burns, M. M. Hedman, and C. C. Porco. Unravelling Temporal Variability in Saturn's Spiral Density Waves: Results and Predictions. ApJ, 651:L65–L68, November 2006b. doi: 10.1086/509120.

M. S. Tiscareno, J. A. Burns, P. D. Nicholson, M. M. Hedman, and C. C. Porco. Cassini imaging of Saturn's rings. II. A wavelet technique for analysis of density waves and other radial structure in the rings. Icarus, 189:14–34, July 2007. doi: 10.1016/j.icarus.2006.12.025.

M. S. Tiscareno, J. A. Burns, M. M. Hedman, and C. C. Porco. The Population of Propellers in Saturn's A Ring. AJ, 135:1083–1091, March 2008. doi: 10.1088/0004-6256/135/3/1083.

A. Toomre. On the gravitational stability of a disk of stars. ApJ, 139:1217–1238, May 1964. doi: 10.1086/147861.

A. Toomre. Group Velocity of Spiral Waves in Galactic Disks. ApJ, 158:899, December 1969. doi: 10.1086/150250.

A. B. Underhill, L. Divan, M.-L. Prevot-Burnichon, and V. Doazan. Effective temperatures, angular diameters, distances and linear radii for 160 O and B stars. MNRAS, 189:601–605, November 1979. doi: 10.1093/mnras/189.3.601.

F. van Leeuwen. Validation of the new Hipparcos reduction. A&A, 474:653–664, November 2007. doi: 10.1051/0004-6361:20078357.

A. J. Verbiscer, M. F. Skrutskie, and D. P. Hamilton. Saturn's largest ring. Nature, 461: 1098–1100, October 2009. doi: 10.1038/nature08515.

M. Vukcevic. Non-linear density wave solutions for different models of galaxies. MNRAS, 441:565–570, June 2014. doi: 10.1093/mnras/stu592.

J.A.D. Wattis. An introduction to mathematical models of coagulationäìfragmentation processes: A discrete deterministic mean-field approach. Physica D: Nonlinear Phenomena, 222(1Äì2):1 – 20, 2006. doi: http://dx.doi.org/10.1016/j.physd.2006.07.024.